THESIS FOR THE DEGREE OF DOCTOR OF PHILOSOPHY

Control and Optimization of Fuel Cell Based Powertrains for Automotive Applications

QIAN XUN

Department of Electrical Engineering
Division of Electric Power Engineering
CHALMERS UNIVERSITY OF TECHNOLOGY
Gothenburg, Sweden 2022

Control and Optimization of Fuel Cell Based Powertrains for Automotive Applications
QIAN XUN
ISBN 978-91-7905-639-1

Doktorsavhandlingar vid Chalmers Tekniska Högskola
Ny serie nr. 5105
ISSN 0346-718X

Division of Electric Power Engineering
Department of Electrical Engineering
Chalmers University of Technology
SE–412 96 Göteborg
Sweden
Telephone +46 (0)31-772 1000

Chalmers Bibliotek, Reproservice
Gothenburg, Sweden 2022

To my family and friends

Control and Optimization of Fuel Cell Based Powertrains for Automotive Applications
QIAN XUN
Department of Electrical Engineering
Chalmers University of Technology

Abstract

Fuel cell powered electric vehicles, with fast-refueling time, high energy density, and zero CO_2 emissions, are becoming a promising solution for future fossil-free transportation. However, the relatively slow dynamic response and the inability of recovering the regenerative energy make vehicles solely powered by fuel cells not an immediately attractive solution. Instead, hybrid vehicles powered by fuel cells combined with energy buffers such as batteries and supercapacitors could be of more interest. Due to the unique characteristics of each energy buffer, the vehicle performance may vary with the hybrid energy storage system configuration. This thesis performs a comprehensive study on various energy storage configurations for applications in fuel cell hybrid electric vehicles.

This thesis first examines the fuel cell/supercapacitor passive hybrid configuration where the fuel cell and supercapacitor share the same DC-link voltage. The power distribution between them is inherently determined by their internal resistances. Therefore, the DC-link voltage varies and depends on the vehicle power demand. In this work, a fuel cell/supercapacitor passive hybrid powertrain is first modeled and evaluated. Simulation results show that the energy efficiency is 53%–71% during propulsion and 84%–94% during braking, respectively. Moreover, a 3 kW lab-scale fuel cell/supercapacitor passive hybrid system is designed and investigated. Experimental results show that the fuel cell takes time to respond to a load change, while the supercapacitor provides the transient power, which makes it possible to downsize the fuel cell.

Since the passive configuration loses the active controllability, this thesis further considers a fully-active fuel cell/supercapacitor system to improve the controllability of the power distribution. This configuration requires a boost converter for the fuel cell and a buck-boost converter for the supercapacitor. In this work, an adaptive power split method is used to smooth the fuel cell current and prevent the supercapacitor from exceeding its lower and upper charge limits. The cut-off frequency of the low-pass filter is adaptively controlled by the spectrum area ratio.

Experimental results show that the supercapacitor state-of-charge is effectively controlled within the desired range. Moreover, a load disturbance compensator is proposed and demonstrated to improve the control performance such that the DC-link voltage fluctuation caused by the load current variation is significantly reduced.

This thesis also investigates the cost-effectiveness of different energy buffers hybridized with fuel cells in various trucking applications. First, a chance-constraint co-design optimization problem is formulated. Convex modeling steps are presented to show that the problem can be decomposed and solved using convex programming. Results show that the power rating of the electric machine can be dramatically reduced when the delivered power is satisfied in a probabilistic sense. Moreover, the hybridization of fuel cells with lithium-ion batteries results in the lowest cost while the vehicle using lithium-ion capacitors as the energy buffer can carry the heaviest payload. This work also develops a robust co-design optimization framework considering the uncertainties in parameters (e.g., vehicle movement) and design decision variables (e.g., scaling factors of fuel cells and batteries). Results show that these uncertainties might propagate to uncertainties in state variables (e.g., battery energy) and optimization variables (e.g., battery power), leading to a larger battery capacity and therefore a higher total cost in robust optimal solutions.

In summary, this thesis performs a comprehensive study on control and optimization of fuel cell based powertrains for automotive applications. This will provide a guidance on component selection and sizing, as well as powertrain system configuration and optimization for design of fuel cell powered electric vehicles.

Index Terms: Fuel cell, Electric vehicles, Batteries, Supercapacitors, DC-link voltage, Power distribution, Cut-off frequency, Load disturbance compensator, Chance-constraint co-design optimization, Convex programming, Robust co-design optimization.

Acknowledgements

I sincerely appreciate the financial support from the Swedish Electromobility Center, the Swedish Energy Agency, and the Chalmers Area of Advance Transport.

I would like to thank my supervisor Prof. Yujing Liu for his guidance and support throughout my Ph.D. study. His invaluable insights, suggestions, and comments helped me grow professionally and personally. I also thank my examiner Prof. Ola Carlson for his guidance in study planning, my co-supervisor Dr. Stefan Lundberg for his help with the experiment platform, Prof. Torbjörn Thiringer for his help with EIS testing of fuel cells and supercapacitors, and my colleagues Magnus Ellsén, Jian Zhao, and Felix Mannerhagen for their help with LabView programming and supercapacitor packaging.

I am very grateful to my co-authors Emma Grunditz and Xiaoliang Huang and the colleagues from the Automatic Control group at Chalmers, especially Prof. Nikolce Murgoviski for his help with algorithm development and academic writing as well as Anand Ganesan for helpful discussions.

I had a great time with the colleagues in the Division of Electric Power Engineering at Chalmers, especially with my office mates: Daniel Pehrman, Niladri Roy Chowdhury, and Maryam Mohiti Ardakani.

I sincerely thank my master's students, Denis Hafi-zovic, Georgios Mamolis, Kunyang Huang, and Yuning Li for their help with the experiments.

I really enjoyed my stay with Prof. Ramon Costa-Castelló at the Polytechnic University of Catalonia, Spain. Special thanks go to Vicente Roda, Unnikrishnan Raveendran Nair, Miquel Martí, and German Fuentes for their help with the experiments.

Finally, I thank my family for their love and my friends for their support.

Qian Xun
Gothenburg, Sweden
April, 2022

List of Acronyms

FC	Fuel cell
SC	Supercapacitor
ICE	Internal combustion engine
GHG	Greenhouse gas
EV	Electric vehicle
PEM	Polymer electrolyte membrane
FCHEV	Fuel cell hybrid electric vehicle
FCHET	Fuel cell hybrid electric truck
SoC	State of charge
PMSM	Permanent magnet synchronous machine
PWM	Pulse width modulation
ESR	Equivalent series resistor
LPF	Low-pass filter
OCV	Open circuit voltage
LiC	Lithium-ion capacitor
LiB	Lithium-ion battery
FEM	Finite element method
SoD	State of degradation

CDF	Cumulative distribution function
WLTC	Worldwide harmonized Light duty driving Test Cycle
FTP72	Federal Test Procedure
ArtUrban	Artemis Urban
NEDC	New European Driving Cycle
ArtRural	Artemis Rural
EUDC	Extra Urban Driving Cycle
HWFET	Highway Fuel Economy Test Cycle
ArtMW130	Artemis Motorway 130
CSC	City Suburban Cycle
MBC	Manhattan Bus Cycle

Contents

Part I

Overview

Chapter 1

Introduction

This chapter introduces the background, motivations, and research questions that are being addressed in this thesis. It describes the thesis outline and the main contributions, followed by a list of the publications.

1.1 Technical Background

The development of internal combustion engine (ICE) vehicles is one of the greatest achievements of the modern technology. Unfortunately, the highly developed automotive industry is also a major factor worsening our environment: global warming and greenhouse gas (GHG) emissions [1]. Moreover, the world's crude oil reserves are projected to run out within the next forty years [2]. To address above issues [3], the exploration of alternative and sustainable energy resources is essential.

Transportation electrification is one of the alternatives to reduce GHG emissions and fossil fuel consumption. In fact, electric vehicles (EVs) have started replacing ICE vehicles. Among others, EVs powered by batteries and fuel cells (FCs) are of great interest [4]. In particular, FC powered EVs might be a promising solution thanks to their high energy density and fast refueling time. Various types of FC technologies have been developed: alkaline, phosphoric acid, molten carbonate, solid oxide, polymer electrolyte membrane (PEM), and direct methanol [5–7]. The PEM-based FC (i.e., PEMFC) technology has been demonstrated to be commercially feasible for transportation and automotive applications, especially for passenger cars, buses, logistic vehicles, and trucks [8]. EVs powered by PEMFCs

are efficient, environmentally friendly, and emission-free as they only emit water and heat, if green hydrogen[1] is used as the fuel [9, 10].

So far, the relatively slow dynamic response and the inability of recovering the regenerative energy make vehicles solely powered by FCs a less attractive solution. Instead, vehicles powered by FCs combined with energy buffers such as batteries and supercapacitors (SCs) could be of more interest. In fact, there have been several fuel cell hybrid electric vehicles (FCHEVs) in the market: Honda FCX [11, 12], Honda FCX Clarity, Honda Clarity Fuel Cell [13], Toyota FCHV-adv, Toyota Mirai [14, 15], and Hyundai NEXO [16] for passenger cars; Alpha [17], XCIENT Fuel Cell [18], and GenH2 for trucks; Coradia iLint, Tangshan, Foshan, and Mireo plus H for railway applications; Golden Gate Zero, CFT Flagship, and Hyseas III for maritime applications.

During the past decades, FCHEVs have made significant progress in terms of environmental adaptability, driving range, and performance. FCHEVs have achieved -40 ℃ cold start. Heat dissipation at high temperatures is no longer an issue. The driving range has been extended due to the development of the hydrogen tank. In today's passenger car, the hydrogen tank volume has increased to 60 L and the pressure has increased to 700 bar. The mass ratio of hydrogen to tank has increased to 5.7%. With improvements in power densities of the FC, power converter, and electric machine, the size and weight of FCHEVs have been reduced. However, there are still some challenges to be addressed. For instance, the durability of FCHEVs has not met the U.S. Department of Energy (DoE) target due to the relatively short lifetime of the FC stack. The hydrogen refueling infrastructure needs to be expanded. In fact, only 553 stations have been established by the end of 2020 although more stations are expected to be established in the future [8, 19]. Moreover, the FCHEV cost is still relatively high (e.g., 60000 USD for a Mirai) and the FC takes up to around 40% of it. Therefore, in addition to building up more hydrogen refueling stations, efficiency improvement, lifetime enhancement, and cost reduction of the FC stack are some of the perennial goals and main challenges to be met concurrently, as shown in Fig. 1.1 [8].

1.2 Motivations

To reduce the FCHEV cost, one can reduce the FC system cost [20]. As can be seen in Fig. 1.2, the cost of the FC system in light-duty applications has reduced 67%

[1] Green hydrogen is defined as hydrogen produced by splitting water into hydrogen and oxygen using renewable electricity.

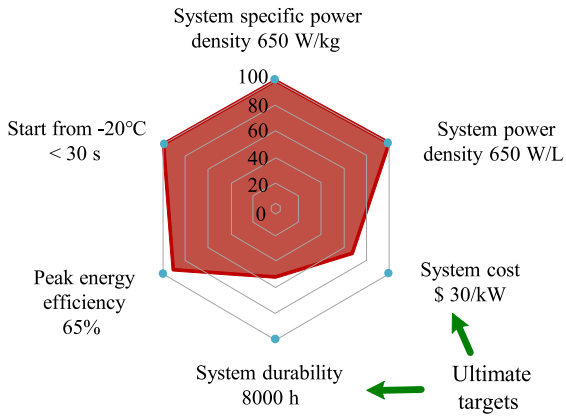

Fig. 1.1: Status in 2015 (filled area) of fuel cell development with respect to the U.S. DoE targets (blue points). Numbers from 0 to 100 indicate the percentage of the targeted property.

since 2006. The cost is targeted to be further decreased to 40 $/kW in 2025 with an ultimate target of 30 $/kW according to U.S. DoE. On the other hand, in most commercial FCHEVs, a full-power rating FC stack is utilized with a small-capacity battery. Therefore, another way to reduce the cost of FCHEVs is to investigate hybridization topologies and properly downsize the power rating of the FC stack, leading to a lower cost of the auxiliary system and the FC system.

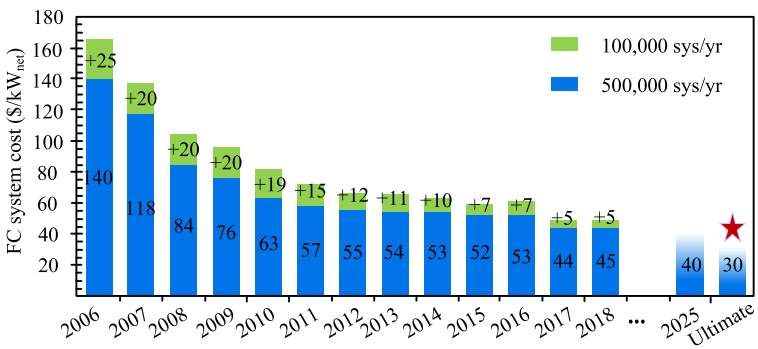

Fig. 1.2: Light-duty fuel cell cost improvement. Data from the Annual Merit Review and Peer Evaluation Meeting in 2019.

Hybridization topologies of FC with other energy storage technologies (i.e., batteries or/and SCs) are classified into passive, semi-active, and fully-active configurations [21, 22]. Several valuable contributions have been made for FC/SC passive

hybrid system, including component sizing [23–27], initial voltage connection [26], experimental verification [26, 27], powertrain system modeling as well as the driving cycles evaluation. However, due to that the FC is directly connected to the DC-link, the DC-link voltage varies with the FC power that is determined by the passive configuration and the load power demand according to the different driving cycles. Also, a varied DC-link voltage might result in different energy efficiency in both component and the whole powertrain system.

To maintain a relatively constant DC-link voltage, DC/DC converters can be utilized to form a semi-active [28–31] or fully-active hybrid system [32–34]. In such configurations, component sizing and power/energy management are critical in reducing purchasing cost, increasing durability of FC stack and decreasing operational cost. In terms of low-level controls, filter-based methods with conventional PI controllers are widely adopted in real-time applications. However, the cut-off frequency is highly dependent on the vehicle specifications and the driving conditions [35, 36]. A constant frequency cannot be suitable for all driving conditions and the DC-link voltage experiences fluctuations when the vehicle frequently accelerates and decelerates [37–39].

Regarding high-level controls, energy management and component sizing of FC hybrid electric vehicles have been separately or sequentially optimized in automotive applications, including buses, trams and trucks. However, their combined optimization has only been well addressed in FC hybrid electric buses [40–42] and has not been comprehensively studied for trucking applications. Due to imperfect manufacture process, modeling simplification and uncertain parameters during vehicle operation, the optimal results obtained from a deterministic co-design optimization might not be robust to variations of parameters and optimization variables [43].

1.3 Aims & Objectives

This thesis aims to address the above issues by answering the following questions:

- What are the possible configurations to hybridize FCs with different energy storage technologies such as batteries and SCs and how do they differ in performance?

For the passive hybrid topology:

- What is the drivetrain and component energy efficiency for different driving cycles?

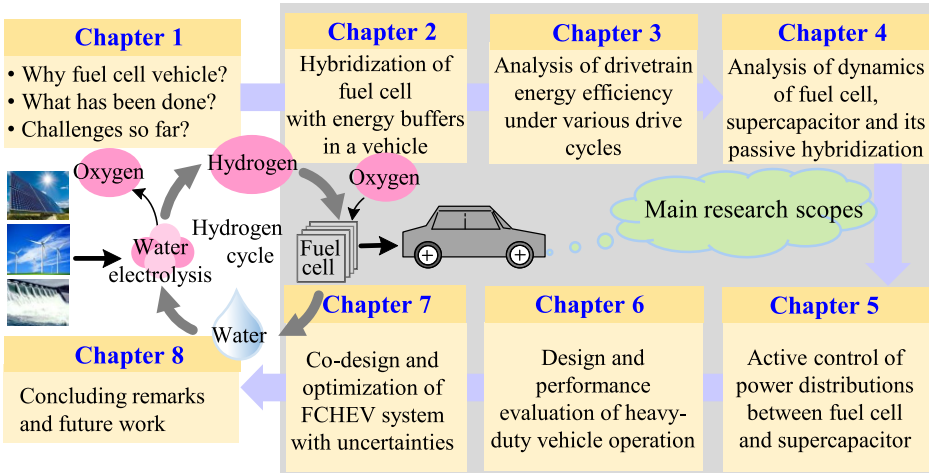

Fig. 1.3: Research framework.

- How can a lab-scale experimental platform be designed for validation of the dynamic characteristics?

For the active hybrid topologies:

- What is the performance of the adaptive power split and the load disturbance compensator in active controlling the power distribution while maintaining a stable DC-link voltage in electric bus applications?
- What is the performance of different energy storage technologies for applications in fuel cell hybrid electric trucks (FCHETs)?
- What is the performance of the robust co-design optimization when considering uncertainties in driving conditions for FCHET applications?

A graphical framework of this thesis is shown in Fig. 1.3. The objective of this thesis is to perform a comprehensive study on FCHEVs: energy storage hybridization configurations, simulation and experimental validation of a passive hybrid configuration, power allocation of an active hybrid configuration, joint component sizing and energy management.

1.4 Main Contributions

The main contributions of this thesis are summarized as follows.

- A FC/SC passive hybrid powertrain for a passenger car is modeled in a high

level of detail. The performance of a pure FC system and the FC/SC passive hybrid system are compared under a pulsed load current. The powertrain efficiency is quantified for various driving cycles.

- A lab-scale FC/SC passive hybrid system is designed and implemented for a light vehicle. The system is experimentally tested using a step load current and a driving cycle current.
- An active FC/SC hybrid system in bus applications is considered and a filter-based method is developed to adaptively control the power distribution between the FC and the SC. To maintain a stable DC-link voltage, a feed-forward compensator is adopted by using a load disturbance observer. The observer can accurately estimate the load current, which makes the feed-forward compensator applicable in cases where the load current is not measurable.
- A chance-constraint optimization algorithm is proposed to evaluate the performance of different energy storage technologies for FCHET applications. The electric machine is sized in a way that the delivered power is satisfied in a probabilistic sense. The sizing of power sources and energy management are optimized considering the FC degradation and cycle life of the energy buffer.
- A robust co-design optimization framework is formulated for FCHETs with consideration of the uncertainties in vehicle movements and design decision variables. The propagation of uncertainties from parameters and design decision variables to other optimization variables is analyzed.

The remaining claimed contributions can be directly found in the research publications.

1.5 Thesis Outline

This thesis consists of two parts. Part I summarizes the author's publications listed in Section 1.6. Part II contains the included papers.

Chapter 2 reviews the theory and characteristics of the FCHEV components. The hybridization topologies of FC with other energy storage technologies (e.g., batteries and SCs) are also covered.

Chapter 3 analyzes the FC/SC passive hybrid system in the time and frequency domains. The powertrain is modeled and simulated with load-dependent component

models. The system energy efficiency is analyzed and evaluated with consideration of the varied DC-link voltage for various driving cycles.

Chapter 4 presents a detailed design procedure for a lab-scale FC/SC passive hybrid system. The system is experimentally validated using a step load current and a driving cycle current.

Chapter 5 considers an active FC/SC hybrid system and develops a filter-based method to adaptively control the power distribution between the FC and the SC. The feed-forward compensator is applied with a load disturbance compensator to maintain a relatively stable DC-link voltage when the load changes frequently.

Chapter 6 develops a chance-constraint optimization algorithm to evaluate the performance of different energy storage technologies for FCHET applications. The formulated problem is decomposed into two sub-problems: (1) limiting demanded power and electric machine sizing; (2) power sources sizing and energy management, which are solved by convex programming.

Chapter 7 presents a robust co-design optimization framework for a FCHET considering uncertainties. The vehicle speed and design decision variables (e.g., scaling factors of FC and battery) are considered to be uncertain and the propagation of uncertainties is illustrated. The performance of deterministic and robust co-design optimization frameworks is compared.

Chapter 8 summarizes the main conclusions and outlines the future work.

1.6 List of Publications

This thesis summarizes the author's work reported in the following publications:

I. **Qian Xun**, Nikolce Murgovski, and Yujing Liu, "Chance-constrained robust co-design optimization for fuel cell hybrid electric trucks", *Applied Energy*, (under revision after first round review), 2022.

II. **Qian Xun**, Nikolce Murgovski, and Yujing Liu, "Joint component sizing and energy management for fuel cell hybrid electric trucks", *IEEE Transactions on Vehicular Technology*, doi: 10.1109/TVT.2022.3154146, 2022.

III. **Qian Xun**, Vicente Roda, Yujing Liu, Xiaoliang Huang, and Ramon Costa-Castelló, "An adaptive power split strategy with a load disturbance compensator for fuel cell/supercapacitor powertrains", *Journal of Energy Storage*, vol. 44, Part A, p. 103341, 2021.

IV. **Qian Xun**, Stefan Lundberg, and Yujing Liu, "Design and experimental verification of a fuel cell/supercapacitor passive configuration for a light vehicle" *Journal of Energy Storage*, vol. 33, p. 102110, 2021.

V. **Qian Xun**, Yujing Liu, Xiaoliang Huang, Emma Arfa Grunditz, Jian Zhao, Nan Zhao, "Drive cycle energy efficiency of fuel cell/supercapacitor passive hybrid vehicle system," *IEEE Transactions on Industry Applications*, vol. 57, no. 1, pp. 894-903, 2021.

VI. **Qian Xun** and Yujing Liu, "Evaluation of fluctuating voltage topology with fuel cells and supercapacitors for automotive applications," *International Journal of Energy Research*, vol. 43, pp. 4807-4819, 2019.

VII. **Qian Xun**, Yujing Liu, and Xiaoliang Huang, "Intelligent power allocation with load disturbance compensator in fuel cell/supercapacitor system for vehicle application," in *Proc. IEEE Transportation Electrification Conference and Expo (ITEC)*, pp. 489-494, 2020.

VIII. **Qian Xun**, Yujing Liu, and Nan Zhao, "Energy efficiency comparison of hybrid powertrain systems for fuel-cell-based electric vehicles," in *Proc. IEEE Transportation Electrification Conference and Expo (ITEC)*, pp. 1234-1239, 2020.

IX. **Qian Xun**, Yujing Liu, Jian Zhao, and Emma Grunditz, "Modelling and simulation of fuel cell/supercapacitor passive hybrid vehicle system," in *Proc. Energy Conversion Congress and Exposition (ECCE)*, pp. 2690-2696, 2019.

X. **Qian Xun**, Yujing Liu, and Elna Holmberg, "A comparative study of fuel cell electric vehicle hybridization with battery or supercapacitor," in *Proc. International Symposium on Power Electronics, Electrical Drives, Automation and Motion*, pp. 389-394, 2018.

The author also contributed to the following publications although they are not covered in this thesis:

I. Xiaorui Guo, **Qian Xun**, Zuxin Li, and Shuxin Du, "Event-triggered consensus algorithm for reactive power sharing considering abnormal communication transmission", *Electric Power Systems Research*, (submitted), 2021.

II. Haotian Xie, Fengxiang Wang, **Qian Xun**, Yingjie He, José Rodríguez, and Ralph Kennel, "A low-complexity gradient descent solution with backtracking iteration approach for finite control set predictive current control," *IEEE Transactions on Industrial Electronics*, vol. 69, no. 5, pp. 4522-4533, 2022.

III. Haotian Xie, Fengxiang Wang, **Qian Xun**, Yingjie He, José Rodríguez, and Ralph Kennel, "Iterative gradient descent based finite control set predictive current control with least squares optimized duty cycles," *IEEE Journal of Emerging and Selected Topics in Power Electronics*, doi: 10.1109/JESTPE.2021.3069804, 2021.

IV. Haihong Qin, Zihe Peng, Ying Zhang, **Qian Xun**, and Dafeng Fu, "A comparative study of freewheeling methods for eGaN HEMTs in a phase-leg configuration", *IEEE Journal of Emerging and Selected Topics in Power Electronics*, vol. 9, no. 3, pp. 3657-3670, 2021.

V. Haihong Qin, Ruoxi Wang, **Qian Xun**, Wenming Chen, and Sixuan Xie, "Switching time delay optimization for "SiC+Si" hybrid device in a phase-leg configuration," *IEEE Access*, vol. 9, pp. 37542-37556, 2021.

VI. Tongguang Yang, Zhenhua Cai, and **Qian Xun**, "Adaptive backstepping-based H∞ robust controller for photovoltaic grid- connected inverter," *IEEE Access*, vol. 8, pp. 17263-17272, 2020.

VII. Tongguang Yang, Bin Li, and **Qian Xun**, "LSTM-attention-embedding model-based day-ahead prediction of photovoltaic power output using Bayesian optimization," *IEEE Access*, vol. 7, pp. 171471-171484, 2019.

VIII. Haihong Qin, Yubin Mo, **Qian Xun**, Ying Zhang, and Yaowen Dong, "A digital-controlled SiC-based solid state circuit breaker with soft switch-off method for DC power system," *Electronics*, vol. 8, no. 8, pp. 837-851, 2019.

IX. Xiaorui Guo, **Qian Xun**, Zuxin, Li, and Shuxin Du, "Silicon carbide converters and MEMS devices for high-temperature power electronics: a critical review," *Micromachines*, vol. 10, no. 6, pp. 406-430, 2019.

X. Haotian Xie, **Qian Xun**, Ying Tang, Fengxiang Wang, José Rodríguez, and Ralph Kennel, "Robust parallel predictive torque control with model reference adaptive estimator for IM drives," in *Proc. International Conference on Electrical Machines (ICEM)*, pp. 2381-4802, 2020.

Chapter 2

Theoretical Framework of Fuel Cell Hybrid Electric Vehicles

This chapter provides the theoretical framework of FCHEVs including the longitudinal vehicle dynamics, key components, and a brief review of the hybridization topologies of FCs with various energy storage technologies.

2.1 Longitudinal Vehicle Dynamics

The vehicle is considered to be a mass point moving on a road surface. Following the Newton's second law of motion, the force balance in time-domain is described as

$$F_{\mathrm{wh}}(t) = (m_{\mathrm{veh}} + m_{\mathrm{r}})\frac{\mathrm{d}v(t)}{\mathrm{d}t} + \frac{c_{\mathrm{d}}}{2}\rho_{\mathrm{a}}A_{\mathrm{f}}v^2(t) + m_{\mathrm{veh}}g\left(\sin\alpha(t) + c_{\mathrm{r}}\cos\alpha(t)\right), \quad (2.1)$$

where $F_{\mathrm{wh}}(t)$ is the wheel force. The term m_{veh} is the vehicle gross (maximum) weight and m_{r} is the equivalent inertial mass of rotational components, including all wheels and the electric machine. The term $v(t)$ is the vehicle moving speed, which is given by a driving cycle speed profile in simulations and experiments. The notations c_{d}, ρ_{a}, A_{f}, g, $\alpha(t)$ and c_{r} are drag coefficient, air density, front area, gravitational constant, road slope, and rolling resistance coefficient. Due to the involvement of mechanical braking, the wheel force can also be written as $F_{\mathrm{wh}}(t) = F_{\mathrm{em}}(t) + F_{\mathrm{brk}}(t)$, where $F_{\mathrm{em}}(t)$ is the traction force of the electric machine and $F_{\mathrm{brk}}(t)$ is the friction braking force. The equivalent inertial mass can

be described as

$$m_{\mathrm{r}} = \frac{1}{r_{\mathrm{wh}}^2}\left(J_{\mathrm{wh}} + k_{\mathrm{gr}}^2 J_{\mathrm{em}}\right), \tag{2.2}$$

where r_{wh} and J_{wh} represent the wheel radius and total inertia of all wheels, respectively. The term k_{gr} is the gear ratio of the entire transmission from the electric machine to wheels, J_{em} is the inertia of the electric machine.

The instantaneous wheel power is calculated as

$$P_{\mathrm{wh}}(t) = v(t)F_{\mathrm{wh}}(t), \tag{2.3}$$

and the energy consumption is the time integral of the wheel power.

2.2 Electric Powertrain

The electric powertrain usually consists of a transmission, a three-phase DC/AC inverter, a permanent magnet synchronous machine (PMSM) and associated control unit. The transmission in an EV is used to adapt the output torque and rotational speed of electric machine to driving wheels. With multiple gear ratios, the transmission system has the capability to adjust a gear ratio according to the different driving conditions. For simplicity and also the most common solution in commercial EVs, it can be considered as a single-step gear with a constant gear ratio.

The electromagnetic torque $T_{\mathrm{em}}(t)$ and rotational speed $n_{\mathrm{em}}(t)$ of the electric machine in motor mode can be computed from the longitudinal force and the vehicle speed, shown as

$$T_{\mathrm{em}}(t) = \frac{r_{\mathrm{wh}}F_{\mathrm{wh}}(t)}{\eta_{\mathrm{gr}}k_{\mathrm{gr}}}, \tag{2.4}$$

$$n_{\mathrm{em}}(t) = k_{\mathrm{gr}}\frac{v(t)}{r_{\mathrm{wh}}}\frac{60}{2\pi} = k_{\mathrm{gr}}\omega(t)\frac{60}{2\pi}, \tag{2.5}$$

where η_{gr} is the transmission efficiency from electric machine to wheels, the term $\omega(t)$ is the wheel angular speed.

As a mechatronic device, the PMSM generates losses in the process of electromechanical energy conversion. The main losses include copper loss, iron loss and mechanical loss. Without considering the mechanical loss, the mean electrical losses [44] are calculated as

$$\begin{aligned} P_{\mathrm{loss,em}} &= \sum P_{\mathrm{loss}} = P_{\mathrm{Cu}} + P_{\mathrm{Fe}}, \\ &= 3i_{\mathrm{s}}^2 R_{\mathrm{s}} + k_{\mathrm{h}} f B^{\beta} + k_{\mathrm{c}} f^2 B^2 + k_{\mathrm{e}} f^{3/2} B^{3/2}, \end{aligned} \tag{2.6}$$

where i_s is the winding RMS phase current, and R_s is the winding resistance, which increases with temperature in reality but is not considered here. The term k_h is the hysteresis core loss coefficient, f is the synchronous frequency, B is the flux density, and β is the weight coefficient of the flux density. The term k_c is the eddy-current core loss coefficient and k_e is the excess core loss coefficient.

The three-phase inverter, equipped with power electronic devices, converts DC voltage to three-phase AC voltage required for PMSM. Due to high-frequency switching and parasitic parameters of power electronic devices, the conduction and switching of both transistors and diodes cause inverter losses. When an ideal sinusoidal pulse width modulation (PWM) three-phase voltage is applied, the average conduction losses and switching losses in IGBTs and free-wheeling diodes during one switching period [45] can be estimated as

$$P_{\text{cond}} = \left(\frac{1}{2\pi} \pm \frac{m_{\text{PWM}}\cos\varphi}{8}\right) V_{\text{th}} i_s + \left(\frac{1}{8} \pm \frac{m_{\text{PWM}}\cos\varphi}{3\pi}\right) R_{\text{on}} i_s^2, \tag{2.7}$$

$$P_{\text{sw}} = f_{\text{sw}} E_{\text{on+off}} \left(\frac{1}{\pi}\frac{i_s}{I_{\text{ref}}}\right)^{k_i} \cdot \left(\frac{V_{\text{DC}}}{V_{\text{ref}}}\right)^{k_v}, \tag{2.8}$$

where m_{PWM} is the PWM modulation index, φ is the phase angle between voltage and current, which is obtained from machine-mapping. The term V_{th} is the on-state threshold voltage, and R_{on} is the on-state resistance. The term f_{sw} is the switching frequency, $E_{\text{on+off}}$ is the energy dissipated during the switch turned on and turned off, I_{ref} is the reference current, to which switching losses in data sheet correlate, V_{DC} is the DC-link voltage, V_{ref} is the reference DC voltage, to which switching losses in data sheet correlate, k_i is the current dependence of switching losses with 1 for IGBTs and 0.6 for diodes, and k_v is the voltage dependence of switching losses with 1.35 for IGBTs and 0.6 for diodes.

2.3 Auxiliary Loads

During the movement of the vehicle, several auxiliary loads also contribute to the power and energy consumption. These loads might include air conditioner, cooling fan, compressor, water pump, lights, control unit, etc. However, the power consumed by the auxiliary loads vary for different types of vehicles. For an electric car, [46] indicates that the power consumption caused by the auxiliary loads varies from 1.5 kW to 6.5 kW. For a 12 m electric bus or trolleybus, the main auxiliary loads may consume the power ranging from 22.5 to 58 kW, while the air condition and heating account for more than 50% of the auxiliary power [47]. The auxiliary

loads consume an average power of around 5.7 kW and a maximum power of around 60 kW in a line haul truck [48].

2.4 Power Sources

Power sources, such as FC, battery, and SC are essential to power an EV. They can cooperate to both provide the propulsion power and store the regenerative braking energy in battery or SC during vehicle operation.

FC, as an energy conversion device, converts the chemical energy from hydrogen into electrical energy with the byproduct of water. A typical polarization curve of a single FC cell is shown in Fig. 2.1. The cell voltage drops when the current increases. Due to electrochemical reactions, the thermodynamic voltage, calculated from Gibbs free energy, is the maximum voltage that can be obtained through the chemical reaction. The losses that are always associated with the thermodynamic voltage, include activation losses, ohmic losses, and concentration losses. When FC works at low current, the activation losses dominates. While ohmic losses become to dominate when the operation current increases. When the operation current increase further, the concentration losses are dominating. Therefore, the output voltage of an individual cell is the thermodynamic voltage subtracted by all losses. A typical cell voltage varies within a range of 0.5-1 V depending on the load current. Several cells are assembled in series to form a FC stack to meet the voltage requirement.

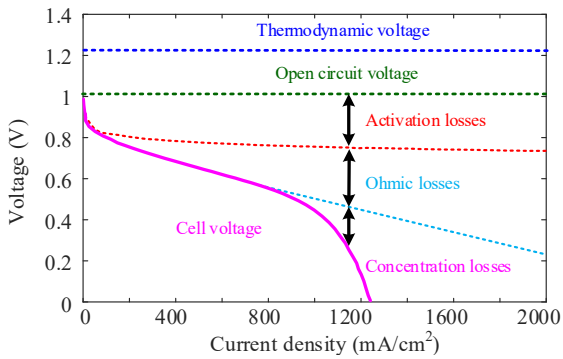

Fig. 2.1: Typical polarization curve of a single cell. Adopted from [49].

The battery and SC, as energy storage devices, are utilized to hybridize with FC to improve the power capability and the dynamic responses of the system. The specific energy and specific power of each power source device are compared in

Fig. 2.2. It is clear to see that the FC shows high energy density and low power density. The SC shows high power density and low energy density. The battery has the moderate power density and energy density. Due to the high power capability of the SC, the cell can be fully charged within a very short time interval, such as few seconds; by contrast, the charging time of the battery is relatively long, which is limited by its power capability. Therefore, the SC might be suitable in applications where the large transient peak power is required for a very short time, while the battery might be suitable for applications where long-time medium power demand is needed. With the development of current technologies, the energy density of the SCs are expected to be comparable with batteries after decades. Lithium-ion capacitor (LiC), as one of hybrid SCs, has the same anode as those used in lithium-ion batteries (LiB) and the same cathode as those used in SCs. The LiC shows advantages of both LiB and SC.

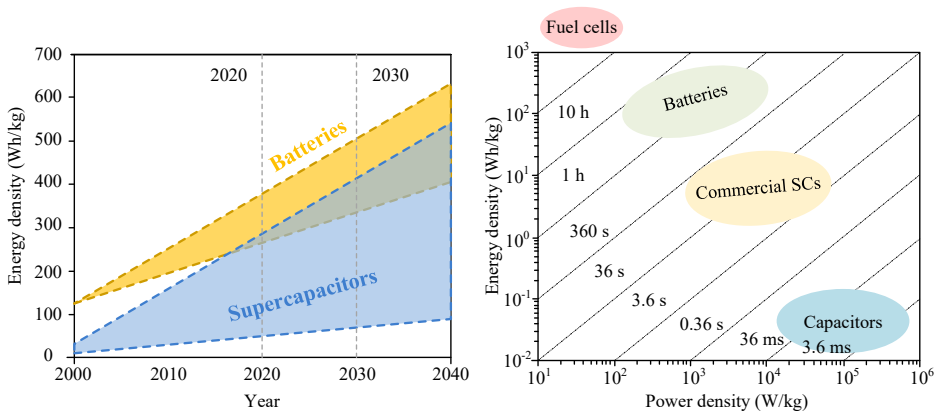

Fig. 2.2: Trends of the development of batteries and supercapacitors in energy density along with the Ragone plot together with fuel cell. Adopted from [50].

Therefore, the hybridization of FC with battery or SC, or both is a great way to make full advantages of each device.

2.5 Fuel Cell Hybrid Powertrains

Due to variable operation voltages of FC, SC and battery, DC/DC converters might be required to hybridize FC with other energy sources. Depending on the number of DC/DC converters and the way each device are connected, the hybridization configurations are illustrated in Fig. 2.3 [4, 21, 51]. The main topologies, including passive, semi-active, and fully-active are developed for different automotive applica-

tions. Some assessment of differences between three configurations is summarized in Table 2.1.

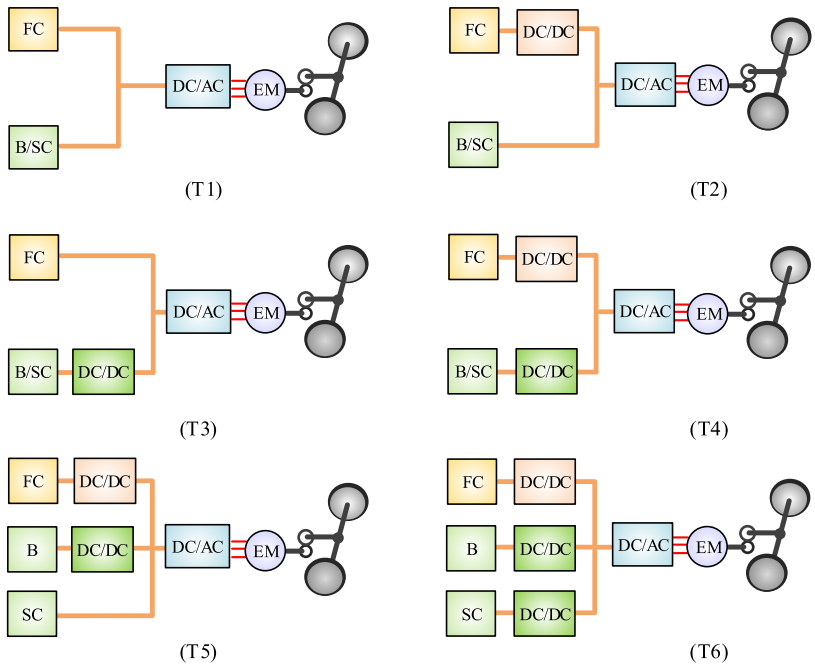

Fig. 2.3: Hybridization topologies of fuel cell with other energy storage technologies in FCHEVs. (T1) Passive hybrid. (T2), (T3), and (T5) are semi-active hybrid. (T4) and (T6) are fully active hybrid.
Note: FC: fuel cell; B: battery; SC: supercapacitor; EM: electric machine.

The fully-active hybrid system has a function of full controllableness since DC/DC converters are associated with each power source [52]. With a reduced number of DC/DC converters, the semi-active hybrid system can only control the DC-link voltage and the power allocation between each device indirectly. Both of them allow an active control of the DC-link voltage and power distribution directly or indirectly. The passive configuration, without any DC/DC converters, cannot control the power distribution actively, which is inherently determined by the internal resistance of each device.

Clearly, active and semi-active hybrid configurations require a well-developed control strategy and additional DC/DC converters to improve the control performance [53–56]. By contrast, without any DC/DC converters and control strategies, the sizing and parameters design of FC and energy buffers in the passive hybrid configuration becomes important. The basic criteria include the operation volt-

Table 2.1: Comparison of different powertrain configurations.

Structure	Fully-active	Semi-active	Passive hybrid
Controllability	G	M	N
Redundancy	A	M	G
Efficiency	A	M	G
Stability	G	M	A
Cost/Complexity	A	M	G

Note: G=Good; M=Marginal; A=Acceptable; N=No acceptable

age matching and the energy storage capacity. Also, the FC operating current dynamics can also be considered as the third design criterion [57].

Chapter 3

Design, Modeling, and Simulation of Passive Hybrid Powertrain

This chapter is based on Papers V, VI, VIII, IX, and X. The objective of this chapter is to present the working principle of the FC/SC passive hybrid system in the time and frequency domains. The design criteria for such a passive hybrid system is described, followed by a case study for passenger car applications. The powertrain and component efficiencies are investigated considering the DC-link voltage variation for several driving cycles.

3.1 Working Principle

3.1.1 Time-domain Analysis

For a general load, the equivalent circuit model of a passive hybrid system of the FC and the SC is shown in Fig. 3.1. The FC is represented by a voltage source connected in series with a resistor. The SC is represented by a nominal capacitance with its equivalent series resistor (ESR). The load is represented by a current source. To prevent the current flowing from the load to the FC, a diode with r_{d} represented as the resistance is placed between the FC and the SC.

The output voltage of the FC can be approximated as a piece-wise linear function,

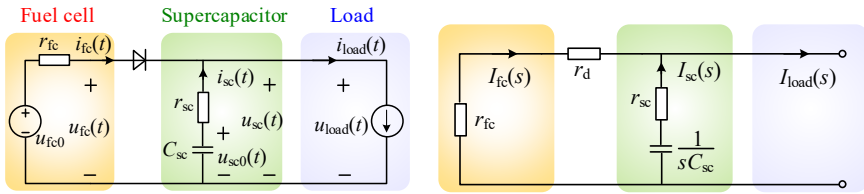

(a) Time-domain. (b) Frequency-domain.

Fig. 3.1: Equivalent circuit model.

which can be described as

$$u_{\mathrm{fc}}(t) = u_{\mathrm{fc0}} - r_{\mathrm{fc}} i_{\mathrm{fc}}(t), \tag{3.1}$$

where $u_{\mathrm{fc}}(t)$ and $i_{\mathrm{fc}}(t)$ denote the FC voltage and current in the continuous time-domain, respectively. u_{fc0} and r_{fc} represent the open-circuit voltage and the equivalent resistance, respectively.

The output voltage of the SC can be obtained by solving the following first-order differential equation, shown as

$$i_{\mathrm{sc}}(t) = C_{\mathrm{sc}} \frac{\mathrm{d}u_{\mathrm{sc0}}(t)}{\mathrm{d}t}, \tag{3.2}$$

where $u_{\mathrm{sc0}}(t)$ is the open circuit voltage (OCV) of the SC and i_{sc} is the SC current, and C_{sc} is nominal capacitance. Following Kirchhoff's law, the current balance can be written as

$$i_{\mathrm{fc}}(t) + i_{\mathrm{sc}}(t) = i_{\mathrm{load}}(t). \tag{3.3}$$

Since the SC ESR is quite small, which can be neglected. By ignoring the diode losses, interconnection losses and the ESR of the SC, one can get

$$u_{\mathrm{sc0}}(t) = u_{\mathrm{sc}}(t) = u_{\mathrm{fc}}(t) = u_{\mathrm{load}}(t). \tag{3.4}$$

By substituting of (3.1), (3.3), and (3.4) into (3.2), we have

$$i_{\mathrm{load}}(t) - i_{\mathrm{fc}}(t) = -C_{\mathrm{sc}} r_{\mathrm{fc}} \frac{\mathrm{d}i_{\mathrm{fc}}}{\mathrm{d}t}. \tag{3.5}$$

Since the FC voltage is approximately equal to the SC voltage, the change rate of the FC voltage is also same as that of the SC voltage. Therefore, the change in FC voltage would result in a proportional change in FC current, as shown in

$$\frac{\mathrm{d}u_{\mathrm{sc}}(t)}{\mathrm{d}t} = \frac{\mathrm{d}u_{\mathrm{fc}}(t)}{\mathrm{d}t} \propto -\frac{\mathrm{d}i_{\mathrm{fc}}(t)}{\mathrm{d}t}. \tag{3.6}$$

3.1.2 Frequency-domain Analysis

The transfer function from the load current to the FC current is derived as

$$G_{\mathrm{fc}}(s) = \frac{1 + sC_{\mathrm{sc}}r_{\mathrm{sc}}}{1 + sC_{\mathrm{sc}}(r_{\mathrm{fc}} + r_{\mathrm{sc}} + r_{\mathrm{d}})}. \tag{3.7}$$

Due to the small ESR of the SC, (3.7) performs as a low-pass filter (LPF) and the cut-off frequency is $1/[2\pi C_{\mathrm{sc}}(r_{\mathrm{fc}} + r_{\mathrm{sc}})]$ by ignoring the diode resistance. At the lower frequency, the DC gain is approximating to 1; while at higher frequency, the DC gain is approximating to 0. Therefore, the FC supplies the DC component while the SC supplies virtually all the high-frequency components. In the mid-frequency region, the impedance of the FC and SC are almost at the same scale and the current distribution is approximately equal. The mid-frequency characteristic is dependent on the pole, which is limited by the selection of the the FC and the SC.

3.2 Design Criteria

To make a functional passive hybrid system, the SC cannot be overcharged by the FC and the load. The output voltage over it should always be within the rated voltage and the following equations should be met

$$u_{\mathrm{sc0}}(t) > u_{\mathrm{fc0}}, \tag{3.8a}$$

$$u_{\mathrm{sc0}}(t) = u_0(t)n_{\mathrm{scs}}, \tag{3.8b}$$

where u_0 is the OCV of the SC cell and n_{scs} is the number of series-connected SC cells. The total capacitance of the SC bank with series connected SC cells can be calculated as

$$C_{\mathrm{sc}} = \frac{1}{\sum_{i=1}^{n_{\mathrm{scs}}} 1/C_i}, \tag{3.9}$$

where C_i is the capacitance of each individual SC cell. The energy capacity of the SC bank is

$$E_{\mathrm{sc}} = \frac{1}{2}C_{\mathrm{sc}}(u_{\mathrm{sc,max}}^2 - u_{\mathrm{sc,min}}^2), \tag{3.10}$$

where $u_{\mathrm{sc,max}}$ and $u_{\mathrm{sc,min}}$ are the maximum and minimum allowed operating voltage of the SC bank, respectively. The energy capacity E_{sc} is designed to store all or partially regenerative braking energy from the propulsion system.

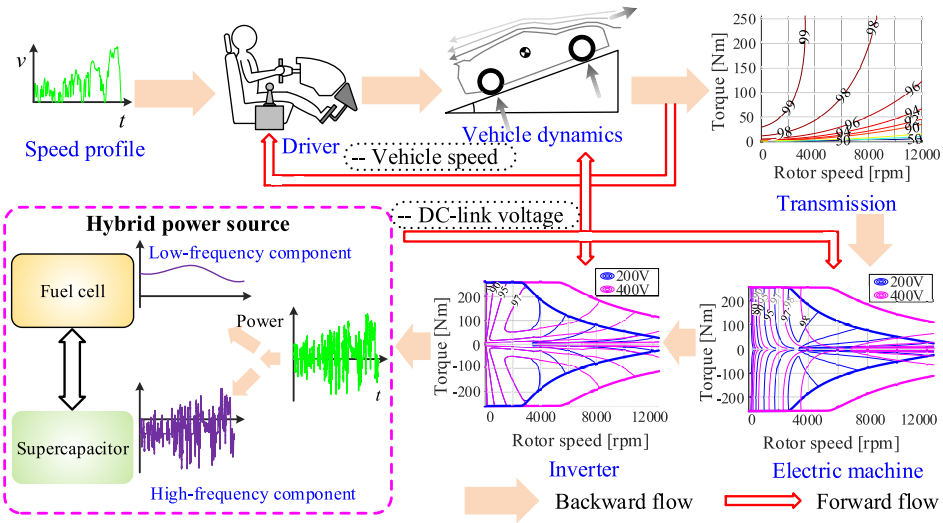

Fig. 3.2: Vehicle simulation configuration.

3.3 Powertrain Configuration

Honda's Clarity FCHEV is studied as a benchmark in this chapter, and each component is modelled and developed from the real world wherever possible to make the simulation applicable. The vehicle system is developed using a quasi-static backward method, shown in Fig. 3.2. The powertrain consists of a FC stack, a SC bank, an IGBT-based inverter, a PMSM, a single-step fixed-speed transmission, vehicle dynamics, and a driver model. The driver is modeled as a PI controller. The transmission efficiency is modelled as a function of electric machine torque and rotational speed. The inverter and the electric machine efficiencies are modeled as functions of the electric machine torque, speed, and the DC-link voltage since the different DC-link voltage might result in the different efficiency at the same operation point. The FC and the SC are modeled by their equivalent circuits.

The input of the simulation is the time-based speed profile from typical driving cycles for passenger cars. The sampling time of the simulation is set to 0.1 s, which is determined by the time resolution of the driving cycle data. To simplify the analysis, auxiliary loads and mechanical losses are not considered. Each component is calculated or modeled in the quasi-steady state, thermal energy losses and other thermal aspects are neglected as such models could not be verified based on previous publications.

3.4 Component Modeling

3.4.1 Electric Machine

The efficiency and losses of electric machine are exported from a model built up in Ansys Maxwell using finite element method (FEM), which is a redesigned version of MCF31 machine in Honda FCX Clarity electric vehicle with parameters published in [58, 59]. The efficiency maps at DC-link voltage levels of 250 V and 400 V are illustrated in Fig. 3.2. It shows that the higher DC-link voltage leads to a wider range of high-efficiency area. The field weakening control can start at a higher speed level as the DC-link voltage increases, and the maximum output power increases with the increased available DC-link voltage.

3.4.2 Three-phase Inverter

The switch used here to calculate inverter losses is Infineon FS400R07A1E3-H5 with a chip temperature of 125 °C and a gate voltage of 15 V, and detailed parameters can be found in [60]. The efficiency map of the inverter varies with electric machine torque and speed at two DC-link voltage levels, as shwon in Fig. 3.2. The efficiency is calculated by the average conduction losses and switching losses of IGBTs and free-wheeling diodes during one switching period described in (2.7) and (2.8). The efficiency has stronger speed dependency than torque, and it increases with the growth of speed. The lower DC-link voltage mostly makes the higher efficiency at operation points with the same torque and speed.

3.4.3 Transmission

The torque losses are modelled as a function of the electric machine torque and speed, and a generic torque loss [59] can be written as

$$T_{\text{loss}}(t) = b_1 + b_2 T_{\text{em}}(t) + b_3 n_{\text{em}}(t) + b_4 T_{\text{em}}^2(t) + b_5 n_{\text{em}}^2(t) + b_6 T_{\text{em}}(t) n_{\text{em}}(t), \quad (3.11)$$

where $b_1 \sim b_6$ are the coefficients. The efficiency in motor mode is calculated as

$$\eta_{\text{gr}} = \frac{T_{\text{em}} - T_{\text{loss}}}{T_{\text{em}}} \times 100\%. \quad (3.12)$$

This gives a gear efficiency as a function of the machine torque and speed. The efficiency decreases with increase of the speed, while it increases slightly with increasing torque, as shown in Fig. 3.2.

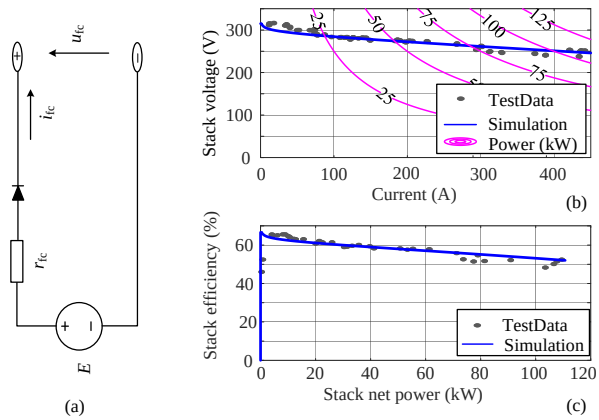

Fig. 3.3: Fuel cell characteristics. (a) Equivalent circuit. (b) Polarization curve. (c) Efficiency curve.

3.4.4 Fuel Cell

A generic equivalent circuit model available in Simscape library in MATLAB/ Simulink is used. The detailed information can be found in [61–67]. The FC is represented by a controlled-voltage source E connected in series with an internal resistance r_{fc}, shown in Fig. 3.3 (a). The model has been validated by the test data of 114 kW Mirai FC stack published in [68] as shown in Fig. 3.3 (b), (c). The FC used in this study is a scaled down version of Mirai stack with 48 kW and the terminal voltage varying from 336 V to 240 V to fit a current range of 0−200 A.

3.4.5 Supercapacitor

The behavior of the SC is represented by a two-branch equivalent circuit model, shown in Fig. 3.4 (a), which has also been used to develop a port crane powertrain [69]. The equivalent parallel resistance, R_{p}, represents the leakage element, C_0 is the main capacitance, a group of series and parallel element (R_{s}, C_{s} and R_{sa}) models the equivalent series resistance and terminal parasitic elements. The SC pack is developed on the 2.7 V-BCAP3000 cell produced by Maxwell [70]. To match the voltage of the FC stack, 125 cells of SCs are connected in series. Note, this parameter is not optimized, but simply taken as a design example to investigate the performance of the FC/SC passive hybrid powertrain. The dynamic characteristics of the SC pack under Worldwide harmonized Light duty driving Test Cycle (WLTC) are shown in Fig. 3.4.

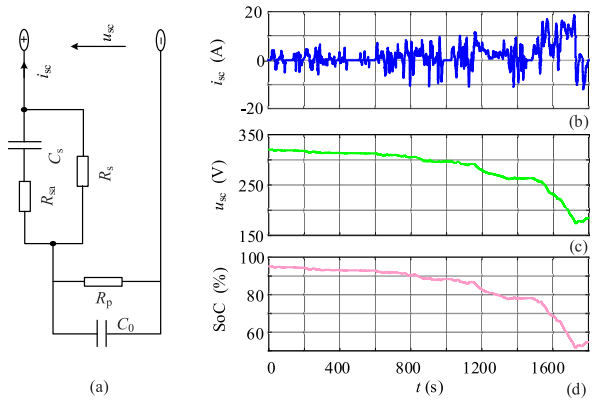

Fig. 3.4: Supercapacitor dynamic characteristics. (a) Simplified equivalent circuit. (b) Load current. (c) Terminal voltage. (d) State of charge (SoC).

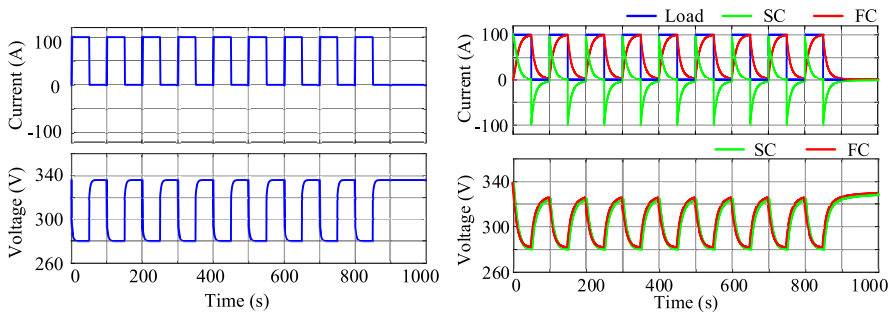

(a) Pure FC.

(b) FC/SC passive hybrid system.

Fig. 3.5: Dynamic behavior between pure FC and FC/SC passive hybrid system under 100 A, 0.02 Hz pulse load.

3.4.6 Passive Hybrid Power Supply

To demonstrate the operation principle of the FC/SC passive hybrid power supply, the dynamic response under 100 A, 0.02 Hz pulse load current is compared with the pure FC dynamic response, shown in Fig. 3.5, where the initial simulation condition is set as no-load. In the pure FC system, the pulse load current causes voltage drop at the transient state when the step load is applied, followed by voltage recovery when the load is removed. In the FC/SC passive system, the SC supplies all the load current and meets the peak load at the beginning due to the smaller impedance of SC, and the SC is operating around an average current of zero since the SC deals with the dynamic load current, while the FC provides the

average load current.

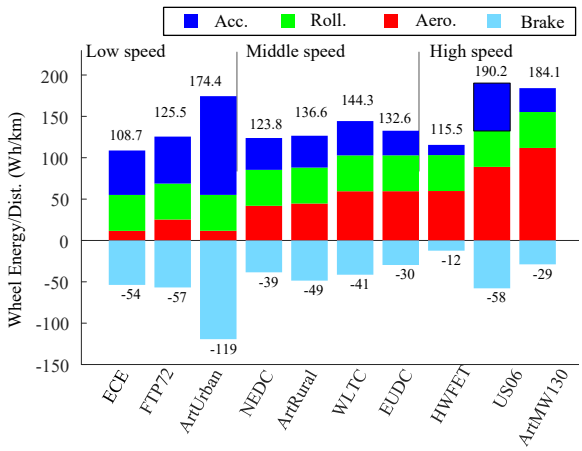

Fig. 3.6: Wheel energy per distance for selected driving cycles.

3.5 Simulation and Evaluation

3.5.1 Driving-cycle Characterization

To evaluate the performance of the powertrain system, 10 official driving cycles are considered. They are categorized into low-, middle-, and high-speed category depending on the driving time spent at speed levels of up to 60 km/h, between 60−90 km/h and above 90 km/h [71]. Therefore, all driving cycles are classified as

- Low-speed driving cycles: ECE, Federal Test Procedure (FTP72), and Artemis Urban (ArtUrban).
- Middle-speed driving cycles: New European Driving Cycle (NEDC), Artemis Rural (ArtRural), WLTC, and Extra Urban Driving Cycle (EUDC).
- High-speed driving cycles: Highway Fuel Economy Test Cycle (HWFET), US06, and Artemis Motorway 130 (ArtMW130).

3.5.2 Energy Consumption for Each Driving Cycle

The wheel energy per driving distance for the selected driving cycles is shown in Fig. 3.6. For each cycle, the propulsion energy consumed by acceleration is as large as the braking energy. In the low-speed driving cycles, ArtUrban has the highest energy consumption due to the largest acceleration energy caused by

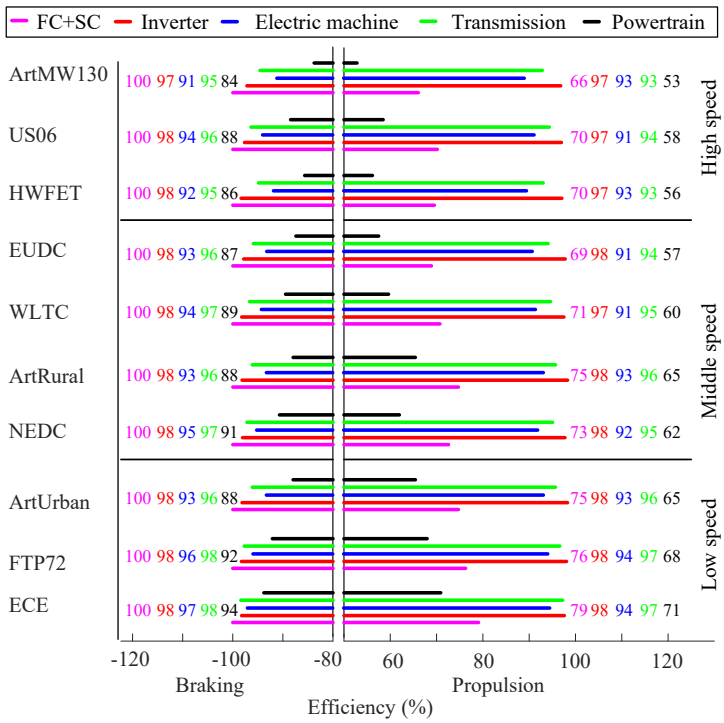

Fig. 3.7: Powertrain average efficiency per cycle in propulsion versus braking mode.

large values in accelerations and power level which is also the highest one among all driving cycles. Among the high-speed level, US06 and ArtMW130 consume as much as 65% more energy than HWFET for propulsion, since the US06 has large speed levels and acceleration, while the ArtMW130 spends more time on the high-speed levels.

3.5.3 Driving Cycle Energy Efficiency

The average energy efficiency, including FC/SC passive hybrid power supply, inverter, electric machine, transmission, and powertrain in both propulsion and braking modes, can be seen in Fig. 3.7 for the selected cycles, and the DC-link voltage range is shown in Table 3.1. Here, the FC/SC system efficiency in propulsion mode is calculated as the hybrid energy efficiency of FC and SC, while the efficiency in braking mode is only related to the SC, since all the braking energy will be absorbed into the SC. The powertrain efficiency during propulsion lies between $53\% - 71\%$, whereas it is higher during braking, i.e., $84\%-94\%$. For all components, the efficiency is the same or higher during braking, but for the

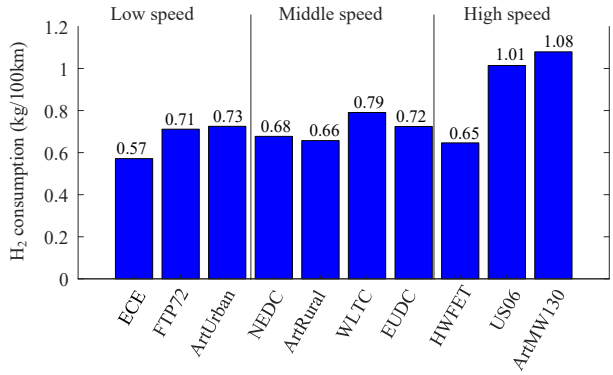

Fig. 3.8: Hydrogen consumption per cycle.

FC/SC system it is much higher since only the highly efficient SC is active. For the selected driving cycles, the lower power demand leads to the relatively higher DC-link voltage. Apparently, the higher DC-link voltage gives higher efficiency on the FC/SC system, electric machine and inverter. In addition, the lower speed and higher torque lead to a higher efficiency of the transmission as noted in Fig. 3.2.

3.5.4 Hydrogen Consumption

The hydrogen consumptions for each driving cycle are shown in Fig. 3.8, with a range of 0.57 kg/100km to 1.08 kg/100km. These values are closely related to vehicle speed, acceleration and power. US06 and ArtMW130 driving cycles consume the highest amount of hydrogen among all driving cycles, and these driving cycles also stand out in terms of average acceleration power and wheel energy per distance. In Fig. 3.6, ArtUrban also stands out regarding the wheel energy per distance, but the hydrogen consumption is much lower because of low-speed levels and low average acceleration power. The third largest hydrogen consumption is WLTC, since WLTC reaches the same speed levels as US06, while US06 and ArtMW130 have the similar range of DC-link voltage. The FC consumes more hydrogen at high speed, high acceleration and low DC-link voltage, which is also reflected in Table 3.1.

3.5.5 Summary

This chapter conducts a comprehensive evaluation of the energy efficiency and hydrogen consumption of the FC/SC passive hybrid powertrain under several driving cycles considering the DC-link voltage variation. The DC-link voltage

Table 3.1: DC-link voltage range for selected driving cycles.

Driving cycles		DC-link voltage (V)
Low-speed cycles	ECE	310−336
	FTP72	293−336
	ArtUrban	305−336
Middel-speed cycles	NEDC	269−336
	ArtRural	267−336
	WLTC	259−336
	EUDC	269−336
High-speed cycles	HWFET	291−336
	US06	260−336
	ArtMW130	260−336

varies with the demanded power, which is determined by the driving conditions. Results show that the energy efficiency is higher under low-speed driving cycles and the hydrogen consumption is higher under high-speed driving cycles due to a larger portion of energy consumption per distance under high-speed driving cycles.

Chapter 4

Experimental Verification of a Lab-scale Passive Hybrid Configuration

This chapter is based on Paper IV. The objective of this chapter is to evaluate the FC/SC passive configuration from both experiments and simulations. Separate measurements are firstly conducted on the FC stack and the SC bank. Then, their passive configuration is experimentally verified through step load current and ArtUrban driving cycle current.

4.1 Design Specifications

Renault Twizy Urban 80 is selected as the benchmark vehicle and its main specifications can be found in [46, 47]. The passive hybrid powertrain consists of an FC stack, a diode, an SC bank, and a propulsion system as shown in Fig. 4.1. The propulsion system, including a DC/AC inverter, an electric machine, a transmission, and wheels, is considered as a dynamic load, which is simulated by a controlled current source for simplicity. The Horizon H-3000 FC stack with a voltage range from 36 to 68.4 V is used in this study and its main specifications can be found in [51]. The Maxwell BCAP3000 SCs are selected to build up the SC bank. According to (3.8), 26 cells are connected in series, giving the SC bank a rated voltage of 70.2 V. The total energy of the SC bank is 195 kJ with the

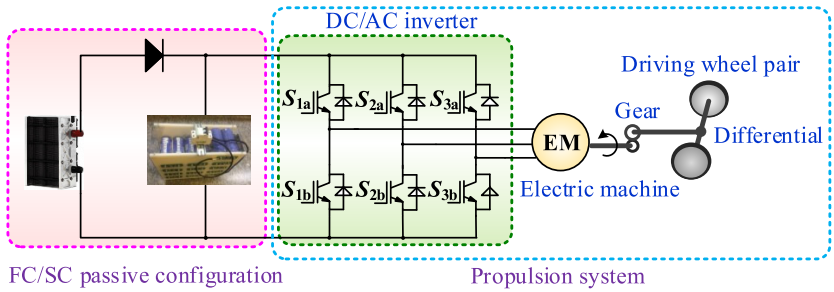

Fig. 4.1: Fuel cell/supercapacitor passive hybrid powertrain.

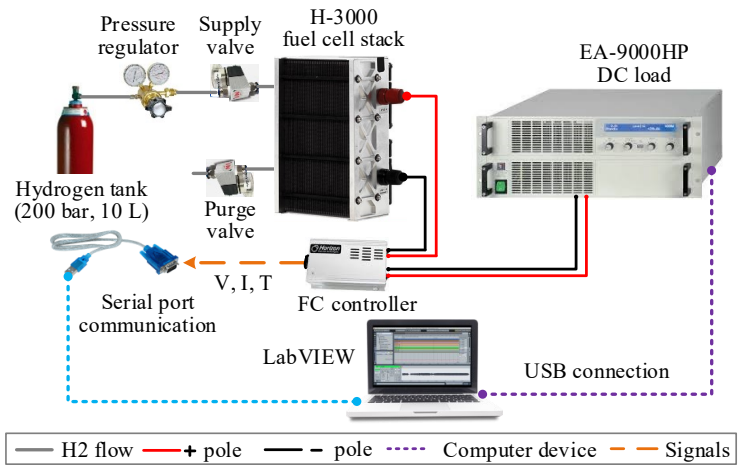

Fig. 4.2: Test platform for fuel cell stack.

total capacitance of around 115 F. The total internal resistance of the SC bank is calculated as 0.00754 Ω.

4.2 Development of Test Platform

4.2.1 Fuel Cell Test Platform

The FC test platform is shown in Fig. 4.2. A 10 L HYDROGEN 6.0 hydrogen tank with an initial pressure of 200 bar from Aga Gas AB is used to provide hydrogen to the FC stack. Due to the low operation pressure of the used FC stack (0.45 to 0.55 bar), a two-stage pressure regulator is connected to adjust the hydrogen pressure from the tank. The first stage is to generate a pressure between 0∼40 bar, and the second stage is to tune the pressure to around 0.5

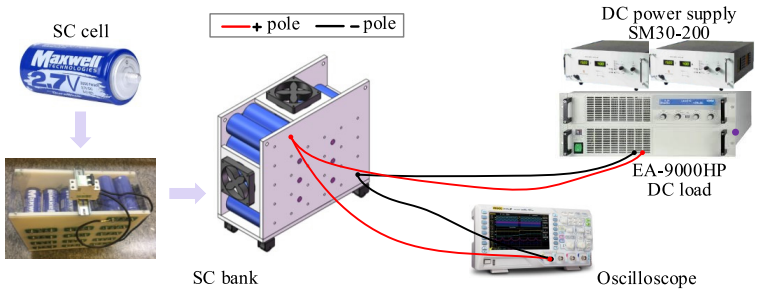

Fig. 4.3: Test platform for supercapacitor bank.

bar. During the FC operation, the unreacted hydrogen needs to be purged out from the purge valve. The output of the purge valve is connected to the outside to avoid the accumulation of hydrogen gas in the lab. The electronic load, EA-9000HP, is connected to provide the dynamic current to the FC stack. The FC controller is used to control the supply valve, purge valve, and air fans as well as to detect the voltage, current, and temperature of the FC stack. The experimental data is collected by LabVIEW interface through serial port communication and oscilloscope.

4.2.2 Supercapacitor Test Platform

The SC bank is tested using the platform shown in Fig. 4.3. Two DC power supplies, SM30-200, are connected in series to generate a maximum voltage of 60 V. The EA-9000HP is connected in parallel to discharge the SC bank. The oscilloscope is used to collect the experimental data. The SC bank is charged and discharged by a constant current of 50 A. The SC bank is charged to the maximum voltage of about 60 V and discharged to 6 V.

4.2.3 Implementation of Passive Hybrid Configuration

The schematic of the FC/SC passive configuration is shown in Fig. 4.4(a) with the experiment platform shown in Fig. 4.4(b). The diode, MUR2X100A02, is used to prevent the energy exchange from the SC bank to the FC stack and the power supply. The DC breakers, C65N-DC, are used to connect or disconnect the separate devices.

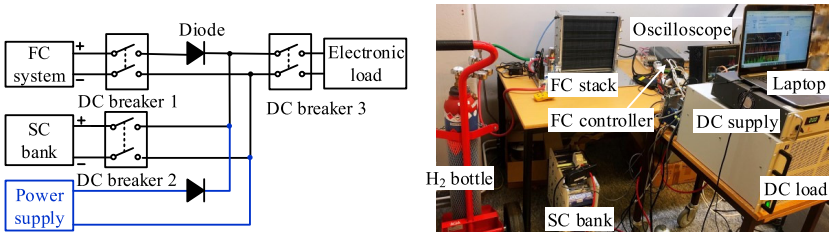

(a) Schematic diagram. (b) Experiment platform.

Fig. 4.4: Experiment configuration for fuel cell/supercapacitor passive hybrid system.

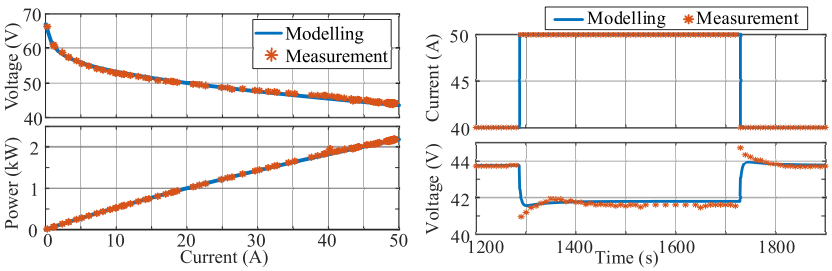

(a) Polarization curve. (b) Dynamic response.

Fig. 4.5: Verification of fuel cell stack model.

4.3 Modelling and Characterization

4.3.1 Fuel Cell Modeling and Characterization

The model parameters are obtained from the tested polarization curve of the FC stack. Fig. 4.5(a) compares the measured and simulated polarization curves using the FC model available in MATLAB/Simulink. The simulation results show a good match with the experimental data with a voltage error within 2%. To investigate the dynamic response of the FC stack to the step load currents, the simulated and measured voltage profiles are shown in Fig. 4.5(b). The voltage has an instantaneous change and there is a time delay for the voltage to reach the steady-state, which suggests that the FC stack performs like a RL branch to the step current. As shown in Fig. 4.5(a), the internal resistance r_{fc} is estimated to be 0.2388 Ω when the FC stack works in the ohmic region.

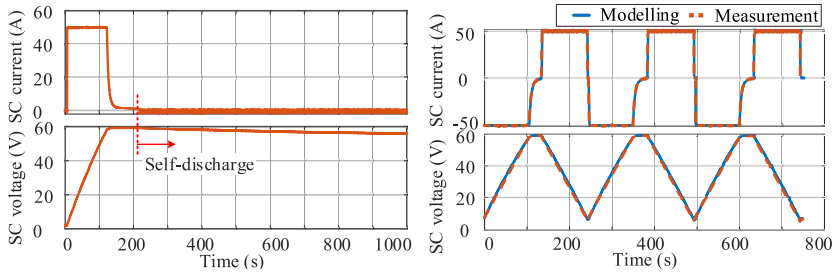

(a) Charge redistribution. (b) Dynamic response.

Fig. 4.6: Verification of the supercapacitor bank model.

4.3.2 Supercapacitor Modeling and Characterization

The charge redistribution is shown in Fig. 4.6(a), where the SC bank is charged to 59.2 V by 50 A and then the charging current reduces to 0 A within several minutes. The SC bank voltage drops to 55.6 V as the charge redistributes. The simulation results using SC model from MATLAB/Simulink is compared with the measured dynamic response, which are shown in Fig. 4.6(b). The smallest error is obtained when $C_{\text{sc}} = 105.85$ F and $r_{\text{sc}} = 0.0225\ \Omega$. Due to the resistors of the connectors and cables, the resistance obtained from the experiments is 10 F lower than the calculated value, and the obtained resistance is a bit higher than the calculated value in Section 4.1.

The obtained voltage error is less than 3% when the voltage is above 16 V and the voltage error is a little bit higher when the voltage is below 16 V. This is because the low voltage is more difficult to model. In the meantime, the measurement error should also be considered.

4.4 Experimental Verification

4.4.1 Short-term Scenario

To evaluate the performance of the FC/SC passive hybrid configuration, the experiment is conducted using step load currents. Note that the FC stack, the SC bank, the power supply, and the electronic load are connected in parallel and they share the same voltage. Therefore, only the load voltage is measured. The test results are shown in Fig. 4.7(a). When the load current with amplitude of 50 A is applied, the FC and SC together provide the current to the electronic

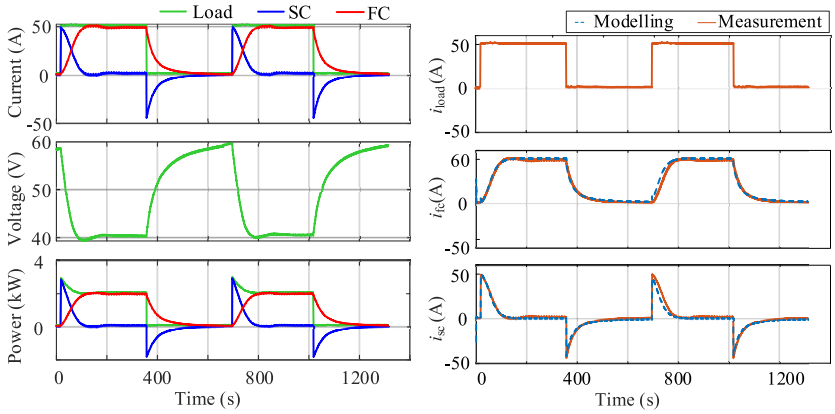

(a) Measurement. (b) Current distribution.

Fig. 4.7: Experimental results of passive hybrid system under step load.

load. The SC bank responds instantly and supplies almost all the current and power due to its smaller internal impedance. With the SC bank providing the power, the SoC of the SC bank decreases, resulting in the decreased voltage. The system voltage is always below 60 V, which means that the FC stack does not operate at the OCV because of the long stabilization time of approximately 120 s, as shown in the figure. This can protect the FC stack against gas starvation and degradation. From the polarization curve of the FC stack, it can be observed that its current increases when its voltage decreases. In this way, the FC current increases gradually to the steady-state due to the reduced system voltage and the FC does not suffer from any current or power transients. When the load current changes from 50 A to 0 A, the FC current decreases gradually from 50 A to 0A, while the SC bank is charged by the FC current and the voltage of the SC bank increases. Since FC stack performs as a RL characteristic under the step load current and the FC current decreases until a new operation equilibrium is reached. In summary, the SC bank responds to the transient current and power instantaneously while the FC stack takes over the steady-state current and power.

The current distributions obtained from the equivalent circuit model and the measurements are compared in Fig. 4.7(b). In the steady state, the FC currents obtained from the equivalent circuit model have error within 4% compared to the measurements, while the errors are slightly higher during transients. This is because the resistance of the FC stack changes with the operating conditions, such as temperature, pressure, and flow rate. The resistance of the SC bank also

changes with the temperature.

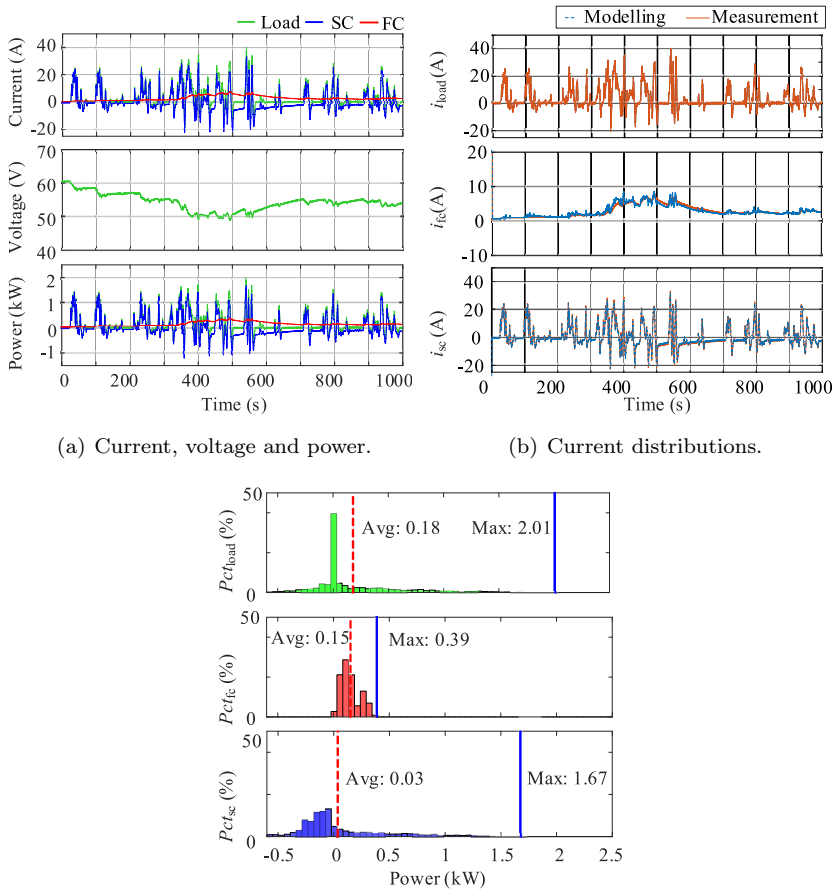

(a) Current, voltage and power.

(b) Current distributions.

(c) Histograms of power.

Fig. 4.8: Experimental results of the passive hybrid system under ArtUrban driving cycle.

4.4.2 Long-term Scenario

The experimental results of the FC/SC passive configuration under a downscaled ArtUrban driving cycle current are shown in Fig. 4.8. As shown in Fig. 4.8(a), when the load current changes frequently, the SC bank reacts to this high-frequency change while the current and power of the FC change gradually due to its relatively higher internal impedance. The maximum FC current/power change rate is 0.62 A/s and 29.64 W/s, which is only 0.9% and 1% of the nominal current/power

per second, respectively. Therefore, the FC degradation is reduced in this passive hybrid configuration. The current distributions between simulation and experiment with the same initial conditions are compared in Fig. 4.8(b) and the simulation shows good consistent with the experiment. The histograms of load power, FC power, and SC power are shown in Fig. 4.8(c) and "Pct" represents the percentage of the specific power in the corresponded total power range. The FC supplies almost the average power of the load while the SC provides nearly zero average power. This results in an energy difference of 0.01 kWh during this driving cycle test. Since the SC handles most of the peak power, the FC can be downsized. In fact, the FC peak power is only about one fifth of the load peak power.

4.4.3 Summary

This chapter shows the design and characterization of a passive FC/SC configuration for a light vehicle. The dynamic characteristics of the FC stack and the SC bank are experimentally illustrated. The feasibility of the FC/SC passive configuration is experimentally verified by a step load current and a driving cycle current. Due to the smaller internal impedance of the SC bank, it provides the transient current and power while the FC stack handles the steady-state current and power. Therefore, it is possible to downsize the FC stack and its peak power demand is only one fifth of the load peak power under the examined driving cycle.

Chapter 5

Adaptive Power Allocation Strategy for Active Hybrid Configuration

This chapter is based on Papers III and VII. The objective of this chapter is to demonstrate the effectiveness of the adaptive power split strategy and the load disturbance compensator for an active hybrid configuration in electric bus applications by performing extensive experiments.

5.1 Control Plant Modeling

The active hybrid powertrain considered in this study is shown in Fig. 5.1 and the variables in time-domain are marked as small letters, while capital letters are used in frequency-domain. Same as Chapter 4, the propulsion system is treated as the dynamic load, where the power is calculated from the speed profile through longitudinal vehicle dynamics. The FC and the SC are represented by a voltage source, $u_{\mathrm{fc}}(t)$, and a capacitor, C_{sc}, respectively. The controller for the SC buck-boost converter is designed to be faster than the controller for the FC boost converter to make sure that the FC does not respond to the sudden load current variation but gradually ramps up to follow the reference. The DC/DC converters of the FC and the SC share the same DC bus capacitor C_{bus}. Therefore, their output voltages are always the same.

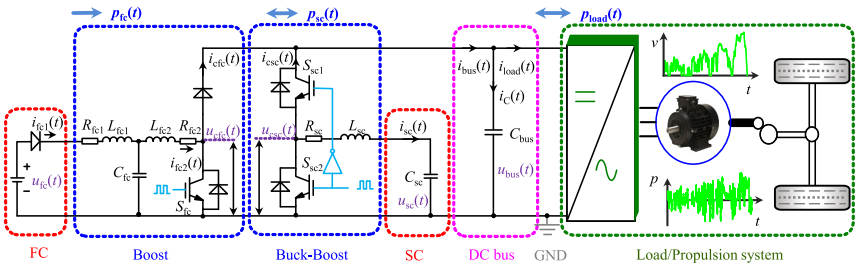

Fig. 5.1: A hybrid FC/SC system for electric vehicle applications.

By ignoring losses of power electronic converters, the power balance equation at the DC-side is expressed as

$$p_{\text{load}}(t) = p_{\text{fc}}(t) + p_{\text{sc}}(t). \tag{5.1}$$

5.1.1 Boost Converter for Fuel Cell

A boost converter is needed to boost the FC voltage as shown in Fig. 5.1. The inductor L_{fc1} and the capacitor C_{fc} act as the input filter for the boost converter. The inductor L_{fc2} is the input inductor of the boost converter. R_{fc1} and R_{fc2} are the parasitic resistors of L_{fc1} and L_{fc2}, respectively. The average voltage across the switch S_{fc} is denoted as $U_{\text{cfc}} = D'_{\text{fc}} U_{\text{bus}}$, where $D'_{\text{fc}} = 1 - D_{\text{fc}}$ and D_{fc} is the duty ratio of the gate signal for the FC side of the boost converter. The input current of the boost converter is derived as

$$I_{\text{fc2}}(s) = \frac{U_{\text{fc}}(s) - \left(L_{\text{fc1}} C_{\text{fc}} s^2 + C_{\text{fc}} R_{\text{fc1}} s + 1\right) U_{\text{cfc}}(s)}{L_{\text{fc1}} L_{\text{fc2}} C_{\text{fc}} s^3 + C_{\text{fc}} \left(L_{\text{fc1}} R_{\text{fc2}} + L_{\text{fc2}} R_{\text{fc1}}\right) s^2 + k_1 s + k_0}, \tag{5.2}$$

where

$$k_1 = \left(C_{\text{fc}} R_{\text{fc1}} R_{\text{fc2}} + L_{\text{fc1}} + L_{\text{fc2}}\right), \tag{5.3a}$$

$$k_0 = \left(R_{\text{fc1}} + R_{\text{fc2}}\right). \tag{5.3b}$$

A variable change is introduced as

$$U_{\text{mfc}}(s) = \frac{U_{\text{fc}}(s)}{L_{\text{fc1}} C_{\text{fc}} s^2 + R_{\text{fc1}} C_{\text{fc}} s + 1} - U_{\text{cfc}}(s), \tag{5.4}$$

which can be used to limit the inrush current when the converter starts since the variable change is set as 0 and FC voltage equals to switch voltage. The inductor current changes slowly from 0 due to the second-order system.

The capacitor C_{fc} of the input filter indeed can be neglected at low frequency since the FC has quite slow dynamics. With the first-order approximated model, the

current of inductor L_{fc1} is the same as that of inductor L_{fc2} with the denotation of $I_{\mathrm{fc1}} = I_{\mathrm{fc2}} = I_{\mathrm{fc}}$. The converter transfer function is approximated as

$$G_{\mathrm{fc}}(s) = \frac{I_{\mathrm{fc}}(s)}{U_{\mathrm{mfc}}(s)} \approx \frac{1}{sL_{\mathrm{fc}} + R_{\mathrm{fc}}}, \tag{5.5}$$

where $L_{\mathrm{fc}} = L_{\mathrm{fc1}} + L_{\mathrm{fc2}}$ and $R_{\mathrm{fc}} = R_{\mathrm{fc1}} + R_{\mathrm{fc2}}$.

5.1.2 Buck-boost Converter for Supercapacitor

A bidirectional DC/DC converter is used to discharge and charge the SC. The gate signals for S_{sc1} and S_{sc2} are always complementary with a small dead-time inserted. L_{sc} is the output inductor and R_{sc} is the parasitic resistor. The average voltage across S_{sc2} is denoted as U_{csc} and the high order switching ripples are neglected. The SC current can be derived as

$$I_{\mathrm{sc}}(s) = \frac{U_{\mathrm{csc}}(s) - U_{\mathrm{sc}}(s)}{sL_{\mathrm{sc}} + R_{\mathrm{sc}}}. \tag{5.6}$$

Similar to the boost converter, the variable change is defined as

$$U_{\mathrm{msc}}(s) = U_{\mathrm{csc}}(s) - U_{\mathrm{sc}}(s)\,. \tag{5.7}$$

Therefore, the transfer function of the converter is written as

$$G_{\mathrm{sc}}(s) = \frac{I_{\mathrm{sc}}(s)}{U_{\mathrm{msc}}(s)} = \frac{1}{sL_{\mathrm{sc}} + R_{\mathrm{sc}}}. \tag{5.8}$$

5.1.3 Current Control Loop

As shown in (5.5) and (5.8), the transfer functions of the DC/DC converters for the FC and the SC show the same first-order linear time-invariant system structure. The conventional PI controller is used to regulate the individual current and the closed-loop transfer function can be described as

$$G_{\mathrm{cl},x}(s) = \frac{G_{\mathrm{PI},x}(s)\,G_x(s)}{1 + G_{\mathrm{PI},x}(s)\,G_x(s)} = \frac{T_{\mathrm{i},x}s + 1}{T_{0,x}^2 s^2 + 2\xi_x T_{0,x} s + 1}, x = \text{fc or sc}, \tag{5.9}$$

with $G_{\mathrm{PI},x}(s) = K_{\mathrm{P},x} + \dfrac{K_{\mathrm{I},x}}{s}$, where $K_{\mathrm{P},x}$ and $K_{\mathrm{I},x}$ respectively denote the coefficients of proportional and integral gains in the PI controller with the time constant calculated as $T_{\mathrm{i},x} = K_{\mathrm{P},x}/K_{\mathrm{I},x}$. $T_{0,x}$ and ξ_x are the time constant and damping coefficient, which are respectively identified as

$$T_{0,x} = \sqrt{\frac{T_{\mathrm{i},x}T_{\mathrm{f},x}}{K_{\mathrm{P},x}K_{\mathrm{f},x}}}, \tag{5.10a}$$

$$\xi_x = \frac{T_{\mathrm{i},x}}{2T_{0,x}}\left(1 + \frac{1}{K_{\mathrm{P},x}K_{\mathrm{f},x}}\right), \tag{5.10b}$$

where $T_{\mathrm{f},x} = L_x/R_x$ and $K_{\mathrm{f},x} = 1/R_x$. Considering the actual parameter values of the current PI controllers, it can be observed that $T_{0x}^2 \approx 0$ and $2\xi_x T_{0x} \approx T_{\mathrm{i}x}$. Therefore, the closed-loop transfer functions of the current loop are approximately equal to 1 in the low-frequency range.

A LPF is used to split the reference current into two parts due to the intrinsic characteristics of the FC and the SC. The transfer function of the LPF is described as

$$H_{\mathrm{LPF}}(s) = \frac{1}{T_{\mathrm{i}} s + 1}, \tag{5.11}$$

where $T_{\mathrm{i}} = 1/(2\pi f_{\mathrm{c}})$ with f_{c} being the cut-off frequency. The low-frequency component is supplied by the FC and the high-frequency part is provided by the SC. In case of negative current and large current change rate, a saturation block and a ramp limiter are designed for the FC reference current, with the transfer function denoted as $G_{\mathrm{lim}}(s)$.

Therefore, the closed-loop transfer function of the DC bus current control, including the LPF saturation block and the ramp limiter, can be derived as

$$G_{\mathrm{cur}}(s) = G_{\mathrm{lim}}(s) H_{\mathrm{LPF}}(s) G_{\mathrm{cl,fc}}(s) + (1 - G_{\mathrm{lim}}(s) H_{\mathrm{LPF}}(s)) G_{\mathrm{cl,sc}}(s). \tag{5.12}$$

Since (5.9) approximates to 1 at the low-frequency range, one can get (5.12) also approximates to 1.

5.1.4 Voltage Control Loop

Using Kirchhoff's current law, the transfer function from the DC bus current and the disturbance (load current) to the DC bus voltage can be respectively derived as

$$G_{\mathrm{bus}}(s) = \frac{U_{\mathrm{bus}}(s)}{I_{\mathrm{bus}}(s)} = \frac{1}{sC_{\mathrm{bus}}}, \tag{5.13a}$$

$$G_{\mathrm{load}}(s) = \frac{U_{\mathrm{bus}}(s)}{I_{\mathrm{load}}(s)} = -\frac{1}{sC_{\mathrm{bus}}}. \tag{5.13b}$$

The voltage PI controller can also be designed and the closed-loop transfer function of the DC bus voltage control can be derived as

$$G_{\mathrm{vol}}(s) = \frac{G_{\mathrm{PI}}(s) G_{\mathrm{cur}}(s) G_{\mathrm{bus}}(s)}{1 + G_{\mathrm{PI}}(s) G_{\mathrm{cur}}(s) G_{\mathrm{bus}}(s)}. \tag{5.14}$$

5.1.5 Dynamic Load

The dynamic load is simulated as a controlled bidirectional current source calculated from the power required during the vehicle operation. Since the power level of

the experimental setup is significantly lower than that of the real vehicle. Hence, current used in the experiment is a scaled down current profile calculated from the real vehicle.

5.2 Control Framework

The control framework for the FC/SC active hybrid system is illustrated in Fig. 5.2, which features an adaptive power split strategy and a load disturbance compensator.

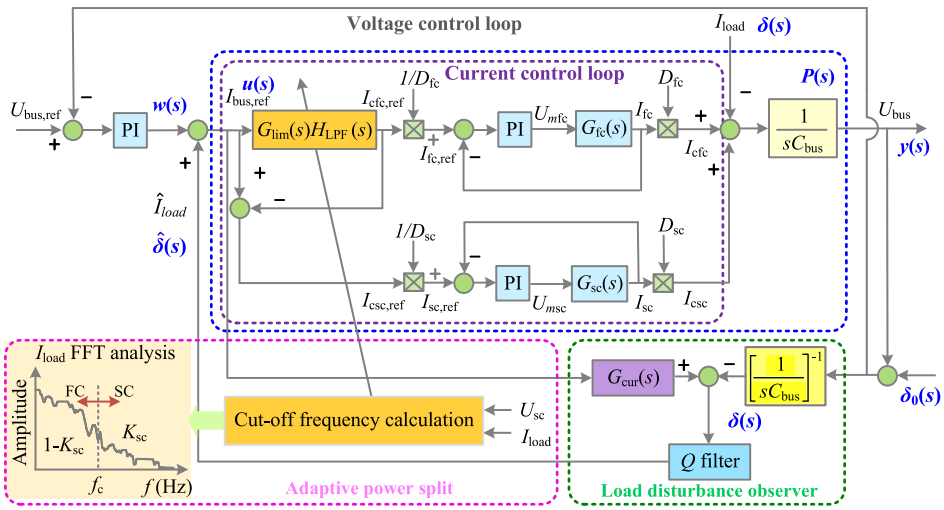

Fig. 5.2: Control framework of FC/SC hybrid system.

5.2.1 Adaptive Power Split Strategy

The implementation of the adaptive power split strategy is described in Fig. 5.3. Due to unidirectional power flow of the FC, a minimum cut-off frequency is directly set when the load current is negative, while the cut-off frequency is adaptively controlled by the area ratio in the frequency spectrum of the load current when the load current is positive. The area ratio, K_{sc}, is defined as the high-frequency spectrum area over the total frequency spectrum area [72], which is a function of SC SoC and the load current. More details can be found in [37]. Once K_{sc} is determined, the cut-off frequency f_c can be calculated.

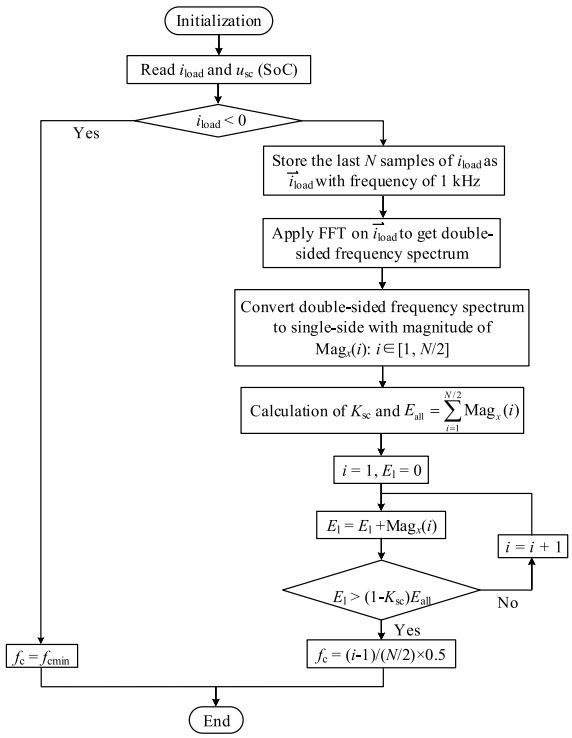

Fig. 5.3: Flow chart of the implementation of the adaptive power split.

5.2.2 Load Distrubance Compensator

The disturbance $\delta(s)$ is the load current, which has effects of $-G_{\text{bus}}(s)$ on the system output $y(s)$. A simplified block diagram of the control framework is shown in Fig. 5.4 to highlight the load disturbance compensator. Therefore, the main task of the load disturbance compensator is to estimate the load current and compensate this current to the input $w(s)$.

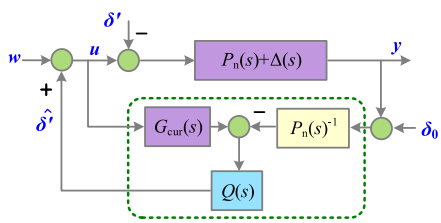

Fig. 5.4: Illustration of the load disturbance compensator.

The control plant of the DC bus voltage can be written as $P(s) := P_{\text{n}}(s) + \Delta(s)$

with the nominal dynamics $P_{\mathrm{n}}(s)$ used for controller design and the uncertain dynamics $\Delta(s)$. In which, $P_{\mathrm{n}}(s) = G_{\mathrm{cur}}(s)G_{\mathrm{bus}}(s)$. $Q(s)$ is the LPF with a relative degree greater or equal to that of $P_{\mathrm{n}}(s)$ [73]. For simplification, a first order LPF, with a same format as (5.11), is used in this work. $\delta_0(s)$ is sensor noise. The load current disturbance can be estimated with a linear function of the system input $u(s)$ and the output $y(s)$, which is shown as

$$\hat{\delta}(s) = Q(s)\left(u(s) - P_{\mathrm{n}}^{-1}(s)y(s) - P_{\mathrm{n}}^{-1}(s)\delta_0(s)\right), \tag{5.15}$$

and the closed-loop transfer function from $w(s)$ to $y(s)$ then becomes

$$H_{\mathrm{LDC}}(s) = \frac{P(s)}{1 + Q(s)\left(P(s)P_{\mathrm{n}}(s)^{-1} - 1\right)}, \tag{5.16}$$

we can see that for low frequencies where $Q(s) \approx 1$ and $H_{\mathrm{LDC}} \approx P_{\mathrm{n}}(s)$, which means that the closed-loop system with the load disturbance compensator can make the system perform the same behavior as the nominal plant model. One can get $y \approx P_{\mathrm{n}}w - \delta_0$ and the system output $y(s)$ can track the reference $w(s)$ without the influence of the disturbance $\delta'(s)$, where $\delta'(s) = \delta(s)/G_{\mathrm{cur}}(s)$.

5.3 Experimental Verification

The experimental work is carried out in the IRI fuel cell laboratory (UPC-CSIC) in Barcelona (Spain) using the test station shown in Fig. 5.5. The test station includes the following components: the FC system from Ballard with nominal parameters of 26 VDC, 46 A, and 1200 W; the SC module from Maxwell with the rated capacitance of 165 F and the rated voltage of 48 V; the DC/DC converters from Semikron$^{\mathrm{TM}}$; the programmable source/sink from Höcherl & Hackl; the DC source LAB/SMS470; the ZS electronic DC load; and the CompactRIO 9049 controller. The DC source is used to simulate the FC before performing experiments on Nexa FC system.

The control strategy is implemented in CompactRIO 9049 controller using LabVIEW. The measurement data is collected by the host computer using a sampling time of 0.1 s. Two bus driving cycles, i.e., Manhattan Bus Cycle (MBC) and City Suburban cycle (CSC) are considered in this work. The dynamic load is simulated by the programmable source/sink, which is controlled by LabVIEW using the host computer. The demanded vehicle power is calculated by using the parameters listed in [40]. The dynamic load current is scaled to have the value within $[-10, 10]$ and the DC bus voltage reference is set as 75 V. Due to the unidirectional current of the FC system, the lower limit of the FC current reference is set 1 A, and the

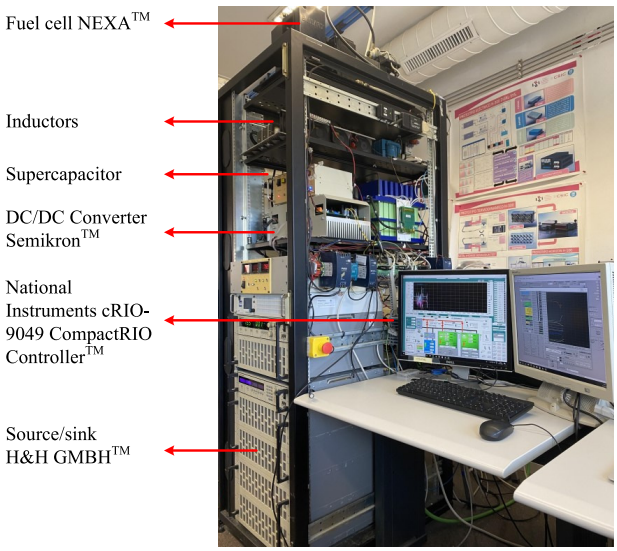

Fig. 5.5: Experimental setup for FC/SC hybrid system.

change rate is limited within ±10% of its rated current per second to avoid the FC system experiencing the large current change rate.

5.3.1 Validation of Load Disturbance Compensator

The performance of the load disturbance compensator is first validated when the DC source is used to simulate the FC. A constant voltage of 32 V is set for the DC source. The time constant in the load disturbance compensator should be selected properly, since a smaller time constant makes the system more sensitive while a bigger time constant makes the system more stable. According to multiple tests, the time constant is selected as 0.025. As can be seen from (5.15), the performance of the load disturbance does not affect by the power distribution between the FC and the SC. Also, to limit FC power variation and maintain a reasonable SC SoC level, the cut-off frequency should be properly selected. Therefore, a constant cut-off frequency of 0.04 Hz is suitable for this particular case for comparison, and a same cut-off frequency is set for the control schemes with and without the load disturbance compensator.

According to (5.13), the effect of the load current disturbance to the output voltage is described by the transfer function $-1/(sC_{\text{bus}})$. This effect is designed to be rejected by the voltage control loop in the conventional cascaded PI control. Since the voltage PI control loop is 10 times slower than the current inner PI loop. There

is always a voltage lag in the DC bus voltage regulation due to the error-based PI controller. Due to the frequent acceleration and deceleration of the electric vehicle, the load power varies accordingly and causes large variations of the load current. As shown in Fig. 5.6, the DC bus voltage fluctuates a lot without the load disturbance compensator, especially at large transient current variations.

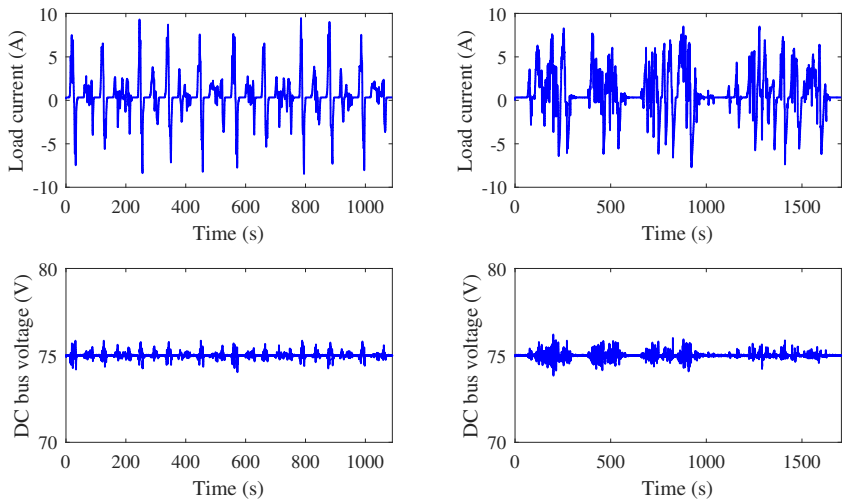

(a) Results under MBC test cycle.

(b) Results under CSC test cycle.

Fig. 5.6: Experimental results of load current and the DC bus voltage without load disturbance compensator. The load current is applied to the source/sink with a sampling time of 0.2 s.

When the load disturbance compensator is applied, the DC bus voltage fluctuation is significantly reduced. These observations are more clearly shown in Fig. 5.7 when the smaller and less varied load current is applied. For example, in the time periods of [160, 220] s in MBC test cycle and [1000, 1400] s in CSC test cycle, the DC bus voltage fluctuations are significantly reduced with the load disturbance compensator applied. However, due to the time delay of the load current estimation and also the estimation errors, the DC bus voltage fluctuations cannot be perfectly canceled in some cases. As illustrated in the time periods of [430, 470] s in MBC test cycle and [400 450] s in CSC test cycle, the DC bus voltage fluctuations are reduced in some extent but still exist.

To further verify the performance of the load disturbance compensator, the DC source is replaced by the Nexa FC system, the test results are shown in Fig 5.8. Due to the larger sampling time of the applied load current, the DC bus

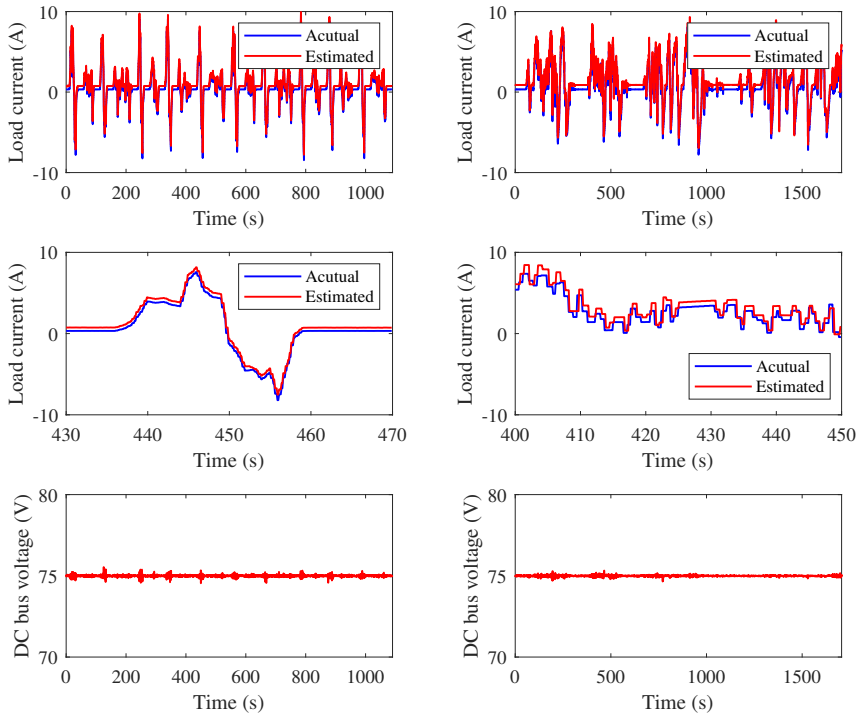

(a) Results under MBC test cycle.

(b) Results under CSC test cycle.

Fig. 5.7: Experimental results of load current and the DC bus voltage with load disturbance compensator. The load current is applied to the source/sink with a sampling time of 0.2 s.

voltage fluctuations are slightly higher than that shown in Fig. 5.6 when the load disturbance compensator is not applied. However, the DC bus voltage fluctuations are significantly reduced with the load disturbance compensator introduced. As aforementioned, due to the time delay and the estimation error of the load current, the DC bus voltage fluctuation cannot be compensated for some cases. In summary, the proposed load disturbance compensator can significantly reduce the DC bus voltage variation caused by the load current change compared to the conventional PI controller without the load disturbance compensator. The performance of the load disturbance compensator is dependent on the load current variation rate and the sampling rate. When the load current changes in a high variation rate, the DC bus voltage still shows some fluctuations with the proposed load disturbance compensator.

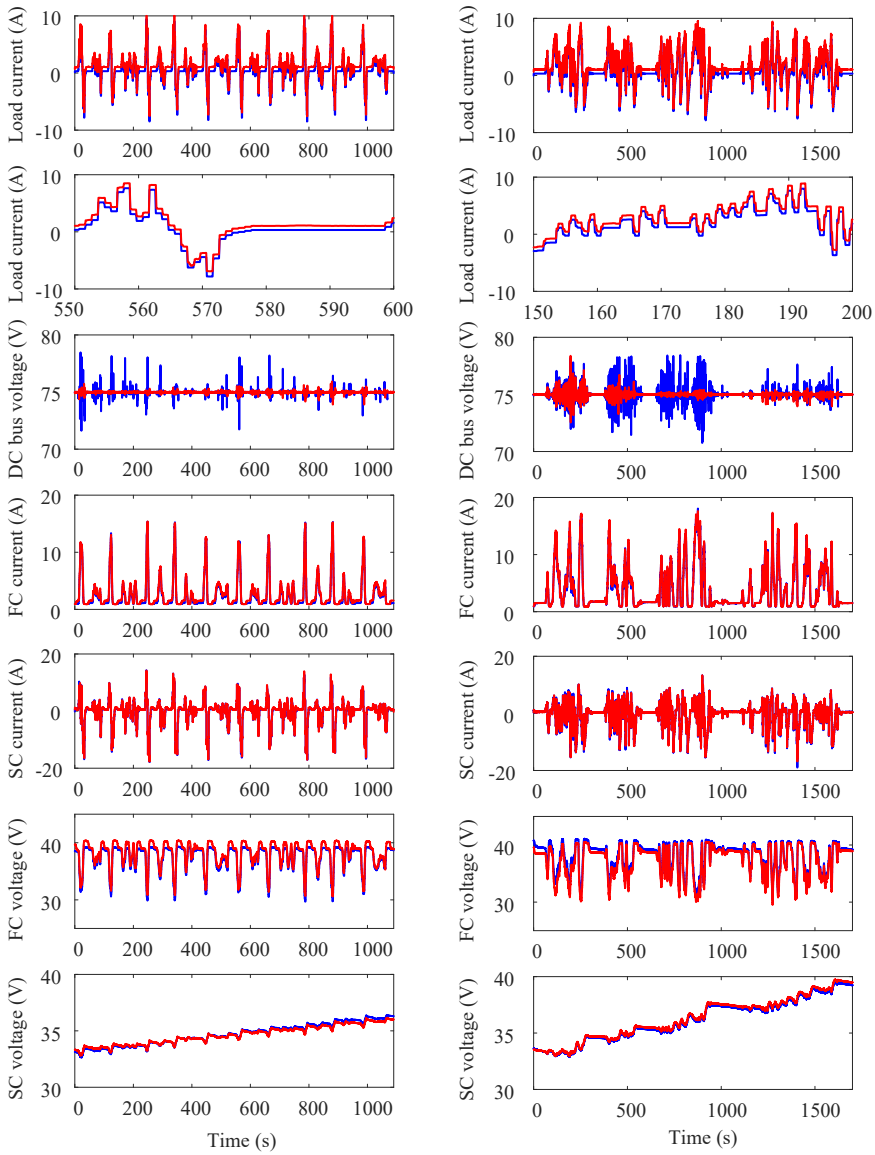

(a) Results under MBC test cycle.

(b) Results under CSC test cycle.

Fig. 5.8: Experimental results with and without load disturbance compensator using Nexa FC system. The load current is applied to the source/sink with a sampling time of 1 s. The blue line and red line in load current plots represent the actual applied load current and the estimated value, while in other plots represent the results without and with load disturbance compensator, respectively.

5.3.2 Validation of Adaptive Power Split Strategy

Similarly, the effectiveness of the adaptive power split strategy is first verified when the DC source is used to simulate the FC. The experimental results of the SC SoC under constant and adaptive cut-off frequencies are compared in Fig. 5.9. A constant cut-off frequency of 0.04 Hz is used as the baseline. Under this constant cut-off frequency, the SC SoCs increase from 68.5% to approximately 74.8% under MBC test cycle and from 69.1% to approximately 83.4% under CSC test cycle. The SC may experience over-charge if this driving cycle continues to repeat more times. When the adaptive cut-off frequency is applied, the SC SoC is controlled in the desired range. In fact, the SC SoC varies from 68.2% to 69.1% under MBC test cycle and from 69.1% to 71.4% under CSC test cycle with the adaptive cut-off frequency. To further verify the performance of the adaptive power split strategy, the DC source is replaced by the Nexa FC system, the test results are shown in Fig. 5.10.

5.3.3 Summary

This chapter develops an adaptive power split strategy with a load disturbance compensator for the fully-active FC/SC hybrid system used in electric bus applications. Experimental results show that the SC SoC is effectively controlled within the desired range by adaptively controlling the current distribution between the FC and the SC. The load disturbance compensator can reduce the DC-link voltage fluctuation caused by the load current variation. Due to the estimation error and the time delay of estimating the load current, the fluctuation is not perfectly cancelled, especially when the load current changes quickly.

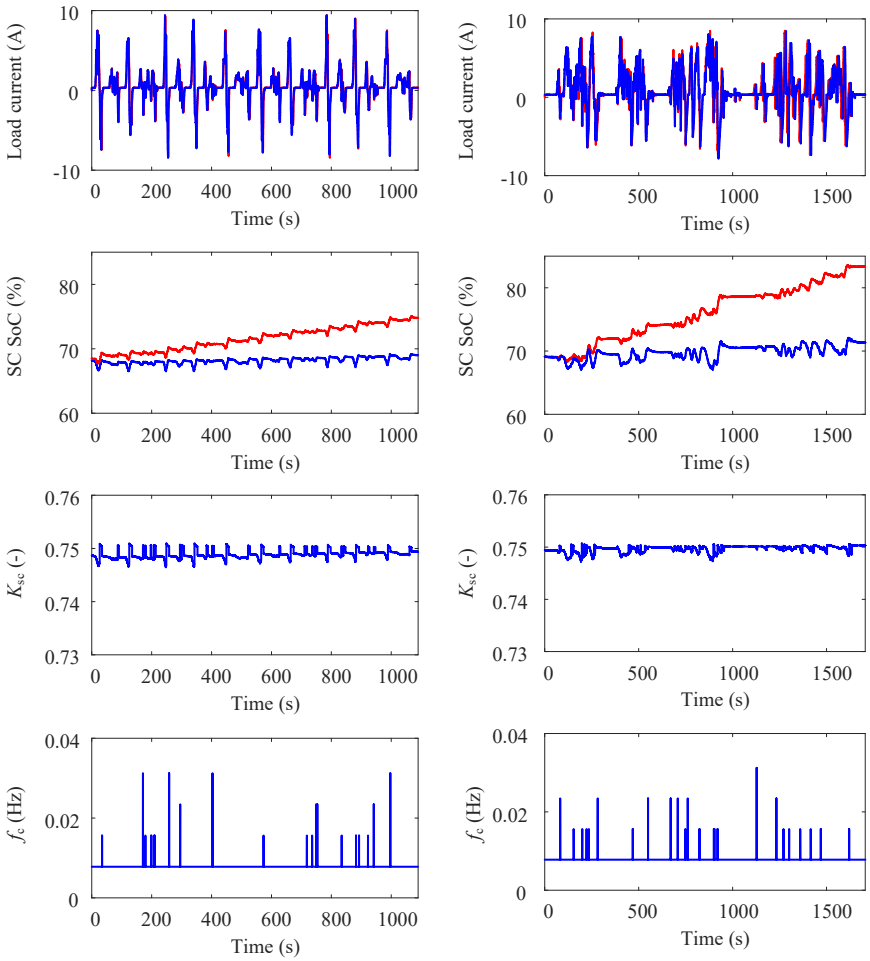

(a) Results under MBC test cycle.

(b) Results under CSC test cycle.

Fig. 5.9: Experimental results for adaptive power slpit strategy validation. The load current is applied to the source/sink with a sampling time of 0.2 s. The red line represents the results under the constant cut-off frequency and the blue line represents the results under the adaptive cut-off frequency.

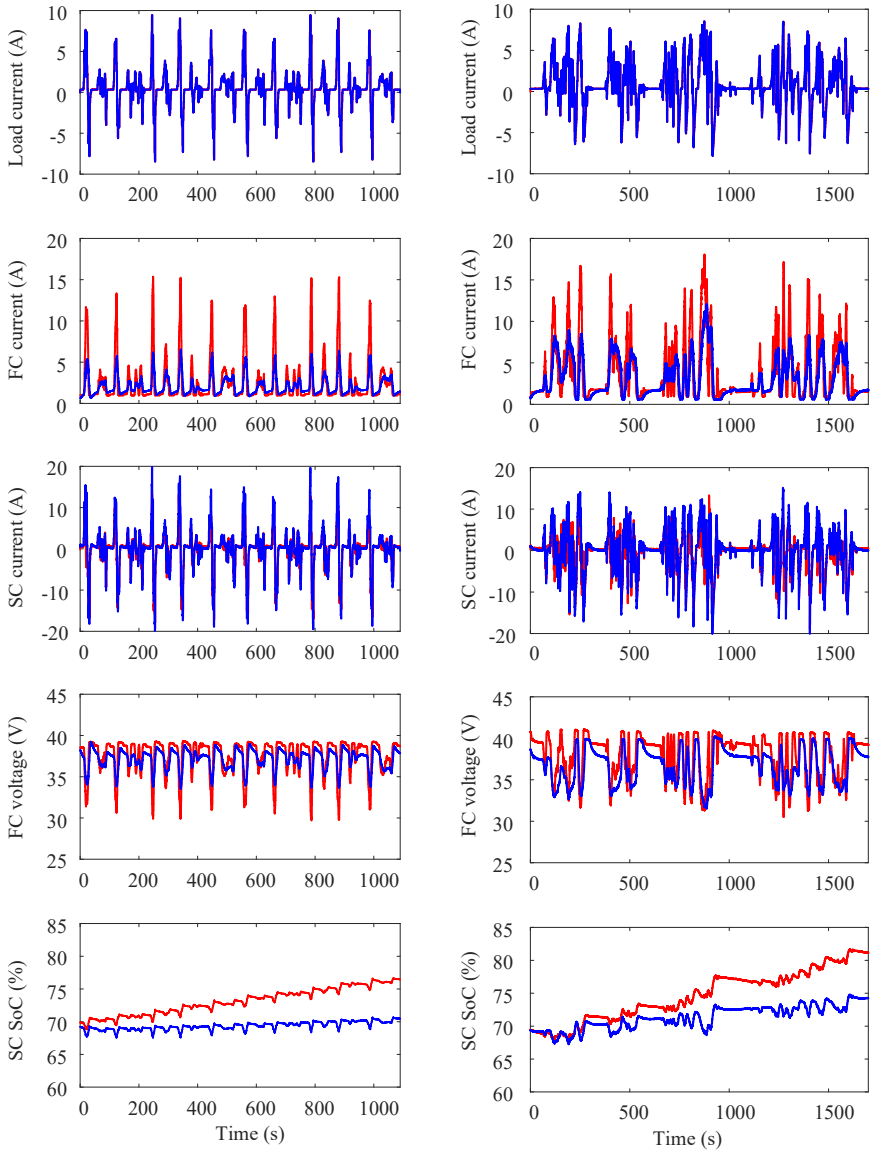

(a) Results under MBC test cycle.

(b) Results under CSC test cycle.

Fig. 5.10: Experimental results for adaptive power slpit strategy validation with Nexa FC system connected. The load current is applied to the source/sink with a sampling time of 1 s. The red line represents the results under the constant cut-off frequency and the blue line represents the results under the adaptive cut-off frequency.

Chapter 6

Joint Component Sizing and Energy Management for Various Trucking Applications

This chapter is based on Paper II. The objective of this chapter is to evaluate the performance of different energy storage technologies in FCHEVs for various trucking applications.

6.1 Mathematical Model

The considered powertrain topology is shown in Fig. 6.1. More details see [74].

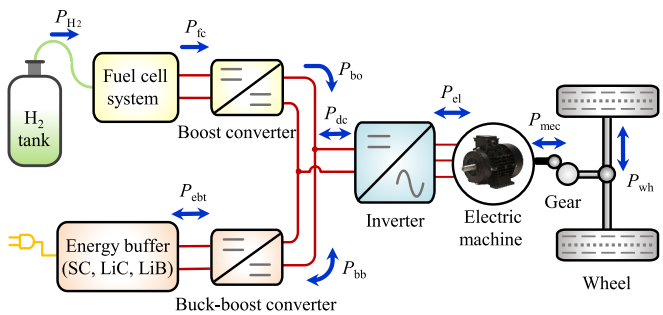

Fig. 6.1: Architecture of the powertrain system.

6.1.1 Driving Cycles

Four typical truck driving cycles developed by the European association of car manufacturers (ACEA), including urban delivery, regional delivery, construction, and long-haul are adopted. The maximum acceleration and deceleration are defined as $2\,\mathrm{m/s^2}$ and $-1\,\mathrm{m/s^2}$, respectively. The total traveling length for all driving cycles is around 100 km.

6.1.2 Power Balance

The FC and energy buffers are supposed to provide all demanded positive power, while energy buffers are designed to store all or partial percentage of braking energy depending on the involvement of the mechanical braking. This can be mathematically expressed as

$$\min\left(P_{\mathrm{ebt}}(t)\eta_{\mathrm{bb}}, \frac{P_{\mathrm{ebt}}(t)}{\eta_{\mathrm{bb}}}\right) + P_{\mathrm{fc}}(t)\eta_{\mathrm{bo}} \geqslant P_{\mathrm{wh}}(t) + P_{\mathrm{loss,em}}(t) + P_{\mathrm{aux}}(t), \quad (6.1)$$

where $P_{\mathrm{ebt}}(t)$ is the terminal power of the energy buffer, $P_{\mathrm{fc}}(t)$ is the output electrical power of the FC, and η_{bo} and η_{bb} are the efficiencies of the boost converter and buck-boost converter, respectively. The term $P_{\mathrm{loss,em}}(t)$ is the power losses of the drivetrain system, including the final gear, the electric machine, and the inverter, $P_{\mathrm{aux}}(t)$ is the power consumption of the auxiliary loads.

6.1.3 Electric Drive System

A 200 kW PMSM with the associated three-phase inverter is adopted as a baseline. The peak torque and peak speed reach to 2850 Nm and 2500 rpm, respectively. The electric power at the DC side varying with the torque and speed is shown in Fig. 6.2(a). The electric power can be approximated by a quadratic function in torque with dependence on angular speed [75]. From the approximated model, the relation of the efficiency varying with the torque and speed can be computed, which is graphically illustrated in Fig. 6.2(b).

The baseline electric machine can be scaled by a scaling factor s_{em} to meet the wheel power demand. Therefore, the electrical power in a scaled electric machine can be derived as

$$P_{\mathrm{em}}(T_{\mathrm{em}}(t), t) = \sum_{i=0}^{2} s_{\mathrm{em}}^{1-i} a_i(\omega(t)) T_{\mathrm{em}}^{i}(t), \quad (6.2)$$

where a_i with $i \in \{0, 1, 2\}$ are the speed-dependent coefficients in the baseline approximation and T_{em} represent the electromagnetic torque in the scaled model.

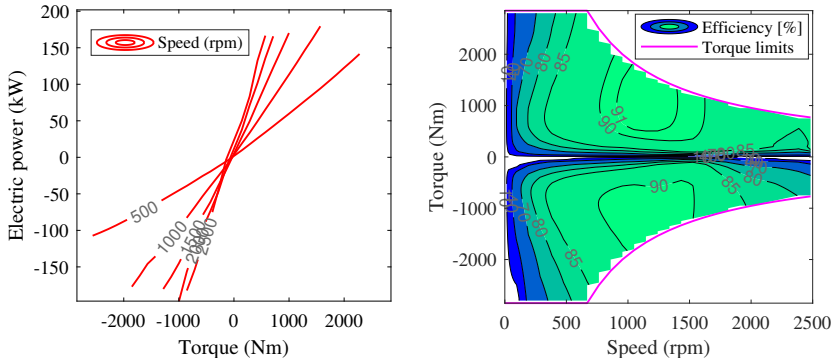

(a) Electric power. (b) Efficiency map.

Fig. 6.2: Electric power and efficiency map of the electric machine with the associated inverter. The electric machine torque is limited by speed dependent bounds.

The scaling factor s_{em} should be bounded within

$$s_{\text{em}} \in [s_{\text{em,min}}, s_{\text{em,max}}]. \tag{6.3}$$

Due to the involvement of the mechanical braking, the torque balance can be relaxed as

$$T_{\text{em}}(t) \geqslant T_{\text{dem}}(t), \tag{6.4}$$

which can also avoid the calculation of braking torque [76]. The longitudinal wheel force that electric machine can provide is limited by the available electromagnetic torque, gear ratio and the vehicle speed. The electromagnetic torque limit is fitted by two parts, where one is determined by the power bound of the baseline electric machine $P_{\text{emb,min}}$ and $P_{\text{emb,max}}$, which limits the wheel force by

$$F_{\text{wh}}(t) \in [s_{\text{em}} P_{\text{emb,min}}/v(t), s_{\text{em}} P_{\text{emb,max}}/v(t)]\,. \tag{6.5}$$

Another one is constrained by torque limits $T_{\text{emb,min}}$, $T_{\text{emb,max}}$, shown as

$$T_{\text{em}}(t) \in [T_{\text{emb,min}}(\omega(t)) s_{\text{em}}, T_{\text{emb,max}}(\omega(t)) s_{\text{em}}]\,, \tag{6.6}$$

where $T_{\text{emb,min}}$ and $T_{\text{emb,max}}$ are the minimal and maximal torque limits of the baseline electric machine, which are functions of rotation speed.

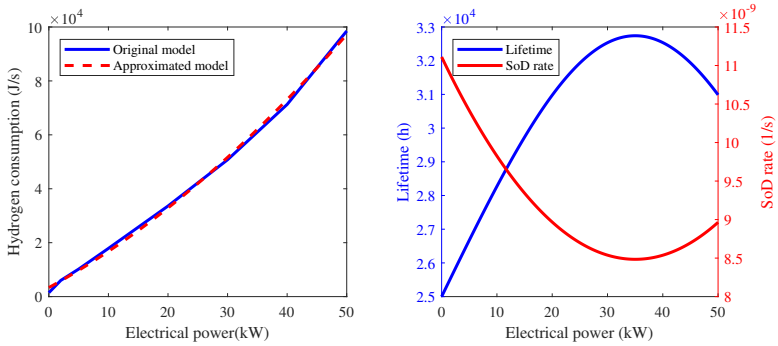

(a) Hydrogen consumption.

(b) Lifetime and degradation rate with respect to power.

Fig. 6.3: Quasi-static fuel cell system model.

6.1.4 Fuel Cell System

Hydrogen Consumption

A 50 kW PEMFC is used as the baseline model in this chapter, which is adopted from the Advanced Vehicle Simulator (ADVISOR) software. The consumed hydrogen varying with the electrical power is illustrated in Fig. 6.3(a), which can be modelled as a quadratic function of the generated electrical power.

The baseline FC model can be scaled by a scaling factor s_{fc}, which is bounded with

$$s_{\mathrm{fc}} \in [s_{\mathrm{fc,min}}, s_{\mathrm{fc,max}}]. \tag{6.7}$$

The relation between the consumed hydrogen and the generated electrical power in the scaled model is derived as

$$P_{\mathrm{H_2}}(t) = \sum_{i=0}^{2} s_{\mathrm{fc}}^{1-i} c_i P_{\mathrm{fc}}^{i}(t), \tag{6.8}$$

where c_i with $i \in \{0, 1, 2\}$ are fitting coefficients in the baseline model. The term P_{fc} is the electrical power in the scaled model, which is constrained by

$$P_{\mathrm{fc}}(t) \in [s_{\mathrm{fc}} P_{\mathrm{fcb,min}}, s_{\mathrm{fc}} P_{\mathrm{fcb,max}}], \tag{6.9}$$

with $P_{\mathrm{fcb,min}}$ and $P_{\mathrm{fcb,max}}$ being the minimum and maximum output power of the baseline FC system.

Performance Degradation

Due to cyclic load variations, the output voltage of the FC fades with time going on. The state of degradation (SoD) is defined as a combination of the number of start/stop cycles and the integration of the degradation rate over time [77, 78]. In this study, the FC is considered as always in "ON" state and thus the start/stop-cycle-based degradation is ignored. The degradation rate is described as a quadratic function determined by the FC operation power in a baseline model, which can be described as

$$\dot{\mathrm{sod}}_{\mathrm{b}}(t) = \sum_{i=0}^{2} d_i s_{\mathrm{fc}}^{-i} P_{\mathrm{fc}}^{i}(t), \tag{6.10}$$

where $d_i \geqslant 0$ is the fitting coefficient. The FC SoD rate varying with its operation power in a baseline model is shown in Fig. 6.3(b). This gives the FC lifetime of at least 25000 hours according to the 2030 target for long-haul trucks. It can be seen that the fading rate of the SoD is greater when the FC operates at high or low power.

It is assumed that the FC lifetime does not change with its power rating. Therefore, the degradation rate in a scaled FC system, $\dot{\mathrm{sod}}(t)$, is the same as that in the baseline model. The SoD over one driving cycle in a scaled model is constrained by

$$\mathrm{sod}(t) \in [0, \Delta\mathrm{sod}], \tag{6.11}$$

with $\Delta\mathrm{sod} = \dfrac{s_{\mathrm{f}}}{L_{\mathrm{avg}} y_{\mathrm{veh}}} \mathrm{sod}_{\max}$, where s_{f} is the length of the driving cycle, L_{avg} is the average travel distance per year, y_{veh} is the truck service years, and $\mathrm{sod}_{\max}$ is the maximum allowed degradation during its lifetime, which is usually set as 1.

To reduce the degradation caused by large power variation, the power variation rate $\dot{P}_{\mathrm{fcs}}(t)$ should be bounded within a certain range, which can be expressed as

$$\dot{P}_{\mathrm{fc}}(t) \in [R_{\mathrm{fcb,min}} s_{\mathrm{fc}}, R_{\mathrm{fcb,max}} s_{\mathrm{fc}}], \tag{6.12}$$

where $R_{\mathrm{fcb,min}}$ and $R_{\mathrm{fcb,max}}$ denote the lower and upper bounds of the power variation rate in a baseline model.

6.1.5 Energy Buffer

Different energy buffer technologies, including SCs, LiCs and LiBs, are investigated. The individual cell can be uniformly modelled as a series connected resistor, R_{eb} with a controlled voltage source represented as OCV, u_{eb}. For SCs and LiCs, the

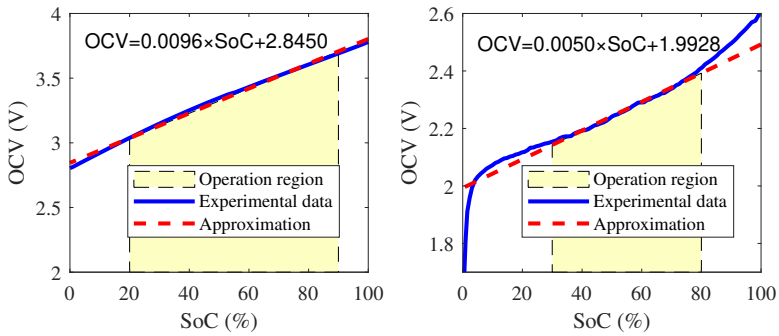

(a) UCK42V28000 cell. (b) Toshba 20 Ah battery [80].

Fig. 6.4: OCV model of LiC and LiB with respect to the SoC levle.

OCVs almost linearly increase with the SoC levels if ignoring the capacitance change. However, the voltage of LiBs varies a lot at lower and higher SoC levels, but the relationship between the OCV and the recommended SoC level can still be approximated to a linear function. The OCVs of representative technologies, Aowei UCK42V28000, and Toshba SCiB20Ah, are illustrated in Fig. 6.4. Following the model by [42, 79], a linear approximation for the OCV of the energy buffer is expressed as

$$u_{\mathrm{eb}}(t) = \frac{Q_{\mathrm{eb}}}{C_{\mathrm{eb}}} \mathrm{soc}_{\mathrm{eb}}(t) + u_{0\mathrm{eb}}, \tag{6.13}$$

where Q_{eb}, C_{eb}, $\mathrm{soc}_{\mathrm{eb}}$ and $u_{0\mathrm{eb}}$ represent the rated capacity, rated capacitance, SoC and the initial voltage of the single cell.

The pack energy and power are only dependent on the total number of cells and are not affected by the connection pattern. The targeted energy buffer is a scaled version of the pack with n_{eb} known a priory. The scaling factor s_{eb} satisfies

$$s_{\mathrm{eb}} \in [s_{\mathrm{eb,min}}, s_{\mathrm{eb,max}}], \tag{6.14}$$

where $s_{\mathrm{eb,min}}$ and $s_{\mathrm{eb,max}}$ are lower and upper bounds. The dynamics of the scaled pack is given as

$$\dot{E_{\mathrm{eb}}}(t) = -P_{\mathrm{eb}}(t), \tag{6.15}$$

where a positive power indicates that discharging current is applied to the energy buffer. The terminal power of the scaled buffer pack is calculated as

$$P_{\mathrm{ebt}}(t) = P_{\mathrm{eb}}(t) - \frac{R_{\mathrm{eb}} C_{\mathrm{eb}} P_{\mathrm{eb}}^2(t)}{2E_{\mathrm{eb}}(t) + u_{0\mathrm{eb}}^2 C_{\mathrm{eb}} s_{\mathrm{eb}} n_{\mathrm{eb}}}. \tag{6.16}$$

Due to the physical limitation of the SoC level and the operation current for a single cell, the internal energy and power of the target pack during the operation need to be restricted to a safe range, which can be described as

$$E_{\mathrm{eb}}(t) \in [E_{\mathrm{eb,min}}, E_{\mathrm{eb,max}}], \tag{6.17a}$$

$$P_{\mathrm{eb}}(t) \in [P_{\mathrm{eb,min}}, P_{\mathrm{eb,max}}], \tag{6.17b}$$

with lower bounds and upper bounds expressed as

$$E_{\mathrm{eb,min}} = s_{\mathrm{eb}} n_{\mathrm{eb}} C_{\mathrm{eb}} \left(u_{\mathrm{eb}}^2(\mathrm{soc}_{\mathrm{eb,min}}) - u_{\mathrm{eb0}}^2\right)/2, \tag{6.18a}$$

$$P_{\mathrm{eb,min}} = i_{\mathrm{eb,min}} \sqrt{s_{\mathrm{eb}} n_{\mathrm{eb}} \left(2E_{\mathrm{eb}}(t)/C_{\mathrm{eb}} + s_{\mathrm{eb}} n_{\mathrm{eb}} u_{\mathrm{eb0}}^2\right)}, \tag{6.18b}$$

$$E_{\mathrm{eb,max}} = s_{\mathrm{eb}} n_{\mathrm{eb}} C_{\mathrm{eb}} \left(u_{\mathrm{eb}}^2(\mathrm{soc}_{\mathrm{eb,max}}) - u_{\mathrm{eb0}}^2\right)/2, \tag{6.18c}$$

$$P_{\mathrm{eb,max}} = i_{\mathrm{eb,max}} \sqrt{s_{\mathrm{eb}} n_{\mathrm{eb}} \left(2E_{\mathrm{eb}}(t)/C_{\mathrm{eb}} + s_{\mathrm{eb}} n_{\mathrm{eb}} u_{\mathrm{eb0}}^2\right)}, \tag{6.18d}$$

where $\mathrm{soc}_{\mathrm{eb,min}}$ and $\mathrm{soc}_{\mathrm{eb,max}}$ are the minimal and maximal SoC of the cell while $i_{\mathrm{eb,min}}$ and $i_{\mathrm{eb,max}}$ denote the maximal charge and discharge current, respectively. Additionally, considering the cycle life of the energy buffer, the energy throughput in a given driving cycle should satisfy

$$E_{\mathrm{ebcl}}(t) \in [E_{\mathrm{ebcl,min}}, E_{\mathrm{ebcl,max}}], \tag{6.19}$$

the lower bound and upper bound are described as

$$E_{\mathrm{ebcl,min}} = 0, \tag{6.20a}$$

$$E_{\mathrm{ebcl,max}} = \frac{2N_{\mathrm{cl}} s_{\mathrm{eb}} n_{\mathrm{eb}} E_{\mathrm{cl}} s_{\mathrm{f}}}{y_{\mathrm{veh}} L_{\mathrm{avg}}}, \tag{6.20b}$$

where N_{cl} is the number of cycles in a whole lifetime and E_{cl} is the maximum allowable energy change per cell in a charging or discharging cycle. The energy throughput is computed as

$$\dot{E}_{\mathrm{ebcl}}(t) = \left|P_{\mathrm{eb}}(t)\right|. \tag{6.21}$$

6.2 Problem Formulation

6.2.1 Objective Function

The objective function is formulated to minimize a total cost consisting of the operation cost (hydrogen and electricity consumption) and the capital cost (FC system, the energy buffer and the electric machine). All costs are evaluated as

euros per unit traveling length to make them comparable. The hydrogen cost is computed as

$$C_{\mathrm{H_2}} = \frac{\beta_{\mathrm{H_2}}}{L_{\mathrm{dc}}\mathrm{LHV}} \int_0^{t_\mathrm{f}} P_{\mathrm{H_2}} \mathrm{d}t, \tag{6.22}$$

where $\beta_{\mathrm{H_2}}$ is the hydrogen unit price in €/kg, L_{dc} is the driving cycle length in meters, and LHV is the lower heating value of hydrogen in J/kg. The electricity cost is written as

$$C_{\mathrm{ele}} = \frac{\beta_{\mathrm{ele}}}{L_{\mathrm{dc}}}(E_{\mathrm{eb}}(0) - E_{\mathrm{eb}}(t_\mathrm{f})), \tag{6.23}$$

with β_{ele} being the unit price of electricity, $E_{\mathrm{eb}}(0)$ and $E_{\mathrm{eb}}(t_\mathrm{f})$ being the stored energy of energy buffer at the beginning and the end of a driving cycle, respectively. The energy change during a travel range L_{range}, typically in the order of 600-800 km, should be limited to the maximum stored energy. As a driving cycle has shorter length than L_{range}, it is assumed that this energy change is evenly distributed into each driving cycle. Therefore, the energy change over one driving cycle should satisfy

$$-\frac{s_\mathrm{f}}{L_{\mathrm{range}}}\Delta E_{\mathrm{eb,max}} \leqslant E_{\mathrm{eb}}(0) - E_{\mathrm{eb}}(t_\mathrm{f}) \leqslant \frac{s_\mathrm{f}}{L_{\mathrm{range}}}\Delta E_{\mathrm{eb,max}}, \tag{6.24}$$

where $\Delta E_{\mathrm{s,max}}$ is the maximum allowable energy change during the travel range, which can be calculated as

$$\Delta E_{\mathrm{eb,max}} = \frac{s_{\mathrm{eb}} n_{\mathrm{eb}} C_{\mathrm{eb}}}{2} \left(u_{\mathrm{eb}}^2(\mathrm{soc}_{\mathrm{eb,max}}) - u_{\mathrm{eb}}^2(\mathrm{soc}_{\mathrm{eb,min}})\right). \tag{6.25}$$

The capital cost of the FC system and the battery pack are dependent on their power rating and energy capacity, respectively. They can be calculated as

$$C_{\mathrm{fc}} = \frac{\beta_{\mathrm{fc}} P_{\mathrm{fcb,max}} s_{\mathrm{fc}}}{L_{\mathrm{avg}} y_{\mathrm{veh}}} \mathrm{CF}, \tag{6.26a}$$

$$C_{\mathrm{eb}} = \frac{\beta_{\mathrm{eb}} s_{\mathrm{eb}} n_0 C_{\mathrm{eb}}}{2 L_{\mathrm{avg}} y_{\mathrm{veh}}} (u_{\mathrm{eb,max}}^2 - u_{\mathrm{eb,min}}^2)\mathrm{CF}, \tag{6.26b}$$

where β_{fc} and β_{eb} are the price of FC and battery in unit power and unit energy, respectively. The terms $u_{\mathrm{eb,min}}$ and $u_{\mathrm{eb,max}}$ denote the minimal and maximal OCV of the cell. The vehicle has an annual traveling length of L_{avg} with total service years in a whole lifetime denoted as y_{veh}. The notation CF is a cost factor dependent on the yearly interest rate and the service years.

Similarly, the capital cost of the electric machine is denoted as

$$C_{\mathrm{em}} = \frac{\beta_{\mathrm{em}} s_{\mathrm{em}} P_{\mathrm{emb,max}}}{L_{\mathrm{avg}} y_{\mathrm{veh}}} \mathrm{CF}, \tag{6.27}$$

where β_{em} is the electric machine price in unit power and $P_{\text{emb,max}}$ is the maximum electrical power of the baseline electric machine. By adding all costs together, one can get the total cost over a unit traveling length, which is described as

$$C_{\text{tot}} = C_{\text{H}_2} + C_{\text{ele}} + C_{\text{fc}} + C_{\text{eb}} + C_{\text{em}}. \tag{6.28}$$

6.2.2 Chance-constrained Programming

Since the driving cycle data might represent different power ratings of trucks, the peak wheel power demand calculated from the driving cycle speed will be scarce in some cases, which also infers small probability of peak wheel power demand. It is of interest to investigate possible cost-benefit if the demanded power is satisfied in a probabilistic sense [81]. This method can also remove outliers of the noisy measurement and give a sensitivity analysis on how component sizes change with the demanded power.

When the demanded wheel power satisfies in a probabilistic sense, the power rating of the electric machine can be reduced, which also minimizes cumulative power provided by the FC and the energy buffer. Therefore, the power balance in (6.1) is rewritten as a chance-constraint

$$\mathbb{P}\left(\begin{array}{c}\min\left(P_{\text{ebt}}(t)\eta_{\text{bb}}, P_{\text{ebt}}(t)/\eta_{\text{bb}}\right) + P_{\text{fc}}(t)\eta_{\text{bo}} \\ \geqslant P_{\text{wh}}(t) + P_{\text{loss,em}}(t) + P_{\text{aux}}(t)\end{array}\right) \geqslant \gamma, \tag{6.29}$$

where $\gamma \in (0, 1]$ is a pre-assigned probability for constraint satisfaction. For any γ satisfying $\gamma < 1$, it is allowed to downsize the FC, energy buffer, electric machine and associated power electronics by delivering less power than demanded for some time intervals. The power balance satisfaction with a known probability $\gamma \in (0, 1]$ gives a wheel power trajectory $P_{\text{wh},\gamma}(t)$ and a reduced electric machine power rating. This consequently will cause the vehicle operation speed to deviate from the requested driving cycle speed. Since the power trajectory $P_{\text{wh},\gamma}(t)$ and the power rating of the electric machine are only determined by the cumulative distribution function (CDF) of the wheel power demand for a given driving cycle. This can be separated before performing the remaining component sizing and energy management. Further details can be found in Section 6.3.

Therefore, the chance-constrained power balance in (6.29) can translate into a deterministic equation, shown as

$$\min\left(P_{\text{ebt}}(t)\eta_{\text{bb}}, \frac{P_{\text{ebt}}(t)}{\eta_{\text{bb}}}\right) + P_{\text{fc}}(t)\eta_{\text{bo}} \geqslant P_{\text{wh},\gamma}(t) + P_{\text{loss,em}}(t) + P_{\text{aux}}(t). \tag{6.30}$$

As aforementioned, the problem consists of several optimization variables, including design decision variables s_{em}, s_{fc}, and s_{eb}, time dependent control variables $P_{\mathrm{fc}}(t)$, $P_{\mathrm{eb}}(t)$, and $T_{\mathrm{brk}}(t)$, and time dependent state variable $E_{\mathrm{eb}}(t)$, $\mathrm{sod}(t)$, and $E_{\mathrm{ebcl}}(t)$. Let $\mathbf{d}$, $\mathbf{x}$, $\mathbf{u}$, and $\mathbf{p}$ represent the vectors of design decision variables, state variables, control variables and parameters. Therefore, one can get $\mathbf{d} = [s_{\mathrm{em}}, s_{\mathrm{fc}}, s_{\mathrm{eb}}]$, $\mathbf{u}(t) = [P_{\mathrm{fc}}(t), P_{\mathrm{eb}}(t)]$, and $\mathbf{x}(t) = [E_{\mathrm{eb}}(t), \mathrm{sod}(t), E_{\mathrm{ebcl}}(t)]$. Due to numerous fixed parameters in $\mathbf{p}$, the elements of the parameter vector are not explicitly listed here but are assumed to appear in the objective function and the constraints. Hence, the total cost expressed in (6.28) can be written as a function $\phi(\mathbf{d}, \mathbf{x}(t), \mathbf{u}(t), \mathbf{p}(t), t)$, which is determined by vectors $\mathbf{d}$, $\mathbf{x}$, $\mathbf{u}$, and $\mathbf{p}$. The problem is formulated to minimize the objective function $\phi(\mathbf{d}, \mathbf{x}(t), \mathbf{u}(t), \mathbf{p}(t), t)$ with respect to inequality constraints $\mathbf{h}$, equality constraints $\mathbf{g}$, and system dynamics $\dot{\mathbf{x}}(t) - \mathbf{f}(\mathbf{d}, \mathbf{x}(t), \mathbf{u}(t), \mathbf{p}(t), t) = 0$. This can be mathematically described as

$$\min_{\mathbf{d}, \mathbf{x}(t), \mathbf{u}(t)} \phi(\mathbf{d}, \mathbf{x}(t), \mathbf{u}(t), \mathbf{p}(t), t), \tag{6.31a}$$

$$\text{s.t. } \mathbf{g}(\mathbf{d}, \mathbf{x}(t), \mathbf{u}(t), \mathbf{p}(t), t) = 0, \tag{6.31b}$$

$$\mathbf{h}(\mathbf{d}, \mathbf{x}(t), \mathbf{u}(t), \mathbf{p}(t), t) \leqslant 0, \tag{6.31c}$$

$$\dot{\mathbf{x}}(t) - \mathbf{f}(\mathbf{d}, \mathbf{x}(t), \mathbf{u}(t), \mathbf{p}(t), t) = 0. \tag{6.31d}$$

By summarizing all constraints, inequality constraint (6.31c) comprises (6.3), (6.4), (6.5), (6.6), (6.7), (6.9), (6.11), (6.12), (6.14), (6.17), (6.19), and (6.30). System dynamics (6.31d) include (6.10), (6.15), and (6.21).

To transcribe the infinite dimensional problem into a finite dimensional problem, the problem (6.31) can be discretized as

$$\min_{\mathbf{d}, \mathbf{x}(k), \mathbf{u}(k)} \phi(\mathbf{d}, \mathbf{x}(k), \mathbf{u}(k), \mathbf{p}(k)), \tag{6.32a}$$

$$\text{s.t. } \mathbf{g}(\mathbf{d}, \mathbf{x}(k), \mathbf{u}(k), \mathbf{p}(k)) = 0, \tag{6.32b}$$

$$\mathbf{h}(\mathbf{d}, \mathbf{x}(k), \mathbf{u}(k), \mathbf{p}(k)) \leqslant 0, \tag{6.32c}$$

$$\mathbf{x}(k+1) - \tilde{\mathbf{f}}(\mathbf{d}, \mathbf{x}(k), \mathbf{u}(k), \mathbf{p}(k)) = 0, \tag{6.32d}$$

where $\mathbf{x}(k)$ is the vector of the discretized form of state variables, $\mathbf{u}(k)$ is the vector of discretized form of control variables, $\mathbf{p}(k)$ is the vector of discretized form of parameters, and $\tilde{\mathbf{f}}(\cdot)$ is the vector of discretized form of dynamic equality constraints. It is clear to see the formulated problem in the present form is nonlinear and non-convex dynamic program.

6.3 Convex Modelling Steps

The convex modelling steps are introduced to show the process of obtaining power trajectory $P_{\mathrm{wh}}, \gamma(t)$ can be formulated as a convex problem after sizing electric machine. Then, the electric machine sizing can be excluded from the problem (6.32), and the remaining sub-problem can also be solved by convex programming.

6.3.1 Sub-problem I for Limiting Demanded Power and Electric Machine Sizing

The target of the sub-problem is to maintain the vehicle to drive as close as possible to demanded speed and travel time but with limited power rating of the electric machine. In practice, this means that the acceleration is limited for some instances due to the limited power rating of the electric machine while higher speed is allowed for some other instances to make sure that the truck still arrives on time. It is noted that the probability γ should be selected properly since it may not be possible to maintain the desired travel when γ is too low. Hence, the constraint on final arriving time is modeled as a soft constraint.

The problem of closely following the original speed, while keeping the delivered power limited and trying to finish the route in about the same time, can be formulated in spatial domain as

$$\min_{\sigma, E_{\mathrm{k},\gamma}, F_{\mathrm{wh},\gamma}, t_\gamma} c_{\mathrm{time}}\sigma + \int_0^{s_\mathrm{f}} \left(E_{\mathrm{k},\gamma}(s) - E_{\mathrm{k}}(s)\right)^2 \mathrm{d}s, \tag{6.33a}$$

$$\frac{\mathrm{d}E_{\mathrm{k},\gamma}(s)}{\mathrm{d}s} = -\frac{\rho_\mathrm{a} c_\mathrm{d} A_\mathrm{f}}{m_\mathrm{veh}+m_\mathrm{r}} E_{\mathrm{k},\gamma}(s) + F_{\mathrm{wh},\gamma}(s) - F_\alpha(s), \tag{6.33b}$$

$$\frac{\mathrm{d}t_\gamma(s)}{\mathrm{d}s} = \begin{cases} \frac{1}{\sqrt{2E_{\mathrm{k},\gamma}(s)/(m_\mathrm{veh}+m_\mathrm{r})}}, & \forall s \in \mathcal{S}_\mathrm{drv} \\ \Delta t_\mathrm{ss}(s)\delta(s), & \forall s \in \mathcal{S}_\mathrm{ss} \end{cases}, \tag{6.33c}$$

$$0 < E_{\mathrm{k},\gamma}(s) \leqslant \max_\mathrm{s}(E_\mathrm{k}(s)), \quad \forall s \in \mathcal{S}_\mathrm{drv}, \tag{6.33d}$$

$$E_{\mathrm{k},\gamma}(s) = 0, \quad \forall s \in \mathcal{S}_\mathrm{ss}, \tag{6.33e}$$

$$t_\gamma(0) = 0, \quad t_\gamma(s_\mathrm{f}) \leqslant t(s_\mathrm{f}) + \sigma, \tag{6.33f}$$

$$F_{\mathrm{wh},\gamma}(s) \geqslant -\frac{P_\mathrm{wh}^\mathrm{max}(\gamma)}{\sqrt{2E_{\mathrm{k},\gamma}(s)/(m_\mathrm{veh}+m_\mathrm{r})}}, \forall s \in \mathcal{S}_\mathrm{drv}, \tag{6.33g}$$

$$F_{\mathrm{wh},\gamma}(s) \leqslant \frac{P_\mathrm{wh}^\mathrm{max}(\gamma)}{\sqrt{2E_{\mathrm{k},\gamma}(s)/(m_\mathrm{veh}+m_\mathrm{r})}}, \forall s \in \mathcal{S}_\mathrm{drv}, \tag{6.33h}$$

$$\frac{T_{\mathrm{emb,min}}(\omega(s))s_\mathrm{em}k_\mathrm{gr}}{r_\mathrm{wh}} \leqslant F_{\mathrm{wh},\gamma}(s) \leqslant \frac{T_{\mathrm{emb,max}}(\omega(s))s_\mathrm{em}k_\mathrm{gr}}{r_\mathrm{wh}}, \forall s, \tag{6.33i}$$

where σ is a slack variable and c_{time} is a weighting coefficient penalizing longer time. The variable $E_{\text{k},\gamma}(s)$ denotes the vehicle kinetic energy when the delivered power has a cumulative probability not greater than γ. More detailed information and convexity of each constraint see [74]. After solving the problem (6.33), the power trajectory $P_{\text{wh},\gamma}$ can be calculated from the optimization variables $E_{\text{k},\gamma}$ and $F_{\text{wh},\gamma}$.

6.3.2 Sub-problem II for Power Sources Sizing and Energy Management

After performing the electric machine sizing in Sub-problem I, the Sub-problem II can be reorganized as minimizing $\phi(\cdot)$ excluding the electric machine cost with respect to (6.3)-(6.6), (6.7), (6.9), (6.10), (6.11), (6.12), (6.14), (6.15), (6.17), (6.19), (6.21), and (6.30).

The objective function $\phi(\cdot)$ is convex. The constraints (6.3)-(6.6), (6.7), (6.9), (6.11), (6.12), (6.14), (6.15), (6.17a), (6.19) are affine relations, and therefore convex. The constraint (6.17b) is nonlinear, but it defines a convex set. To convexity the constraint (6.10), a variable change sodx is introduced, which is also used to scale up the SoD variation over one driving cycle to improve the solver convergence. The term sodx can then be written as

$$\text{sodx}(t) = \frac{\text{sod}(t)}{\Delta\text{sod}} s_{\text{fc}}, \tag{6.34}$$

where $\text{sod}(t) \in [0, \Delta\text{sod}]$ with $t \in [0, t_{\text{f}}]$. At the beginning of the driving cycle, $\text{sodx}(0) = 0$ and at the end of the driving cycle, $\text{sodx}(t_{\text{f}}) \leqslant s_{\text{fc}}$. Take the derivative of (6.34) to obtain

$$\dot{\text{sodx}}(t) = \dot{\text{sod}}(t) \frac{s_{\text{fc}}}{\Delta\text{sod}}. \tag{6.35}$$

Therefore, constraint (6.10), in a relaxed form, can be rewritten as

$$\dot{\text{sodx}}(t) \geqslant \frac{1}{\Delta\text{sod}} \sum_{i=0}^{2} d_i s_{\text{fc}}^{1-i} P_{\text{fc}}^{i}(t), \tag{6.36}$$

which becomes a convex constraint [82].

To avoid the absolute value in constraint (6.21), one more variable P_{ebx} is introduced and (6.21) can be relaxed as

$$\dot{E}_{\text{ebcl}}(t) = P_{\text{ebx}}(t), \tag{6.37a}$$

$$P_{\text{ebx}} \geqslant P_{\text{eb}}, \tag{6.37b}$$

$$P_{\text{ebx}} \geqslant -P_{\text{eb}}. \tag{6.37c}$$

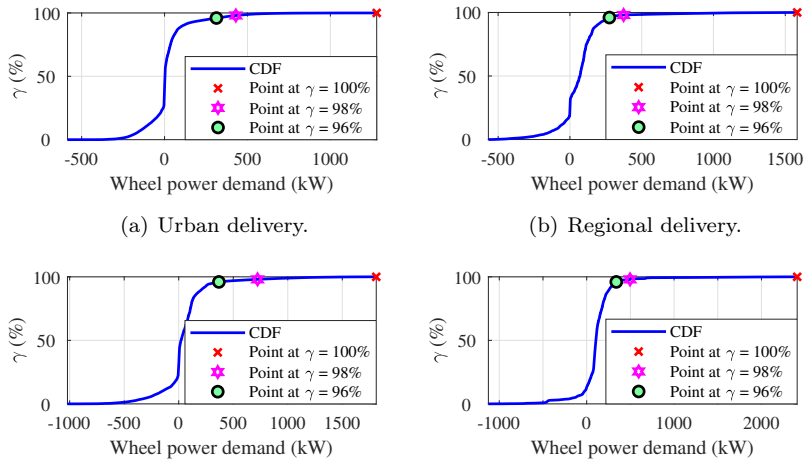

(a) Urban delivery.

(b) Regional delivery.

(c) Construction.

(d) Long-haul.

Fig. 6.5: Cumulative distribution function of the wheel power demand for different trucking applications.

Since constraint (6.30) contains a min function, it can be reformulated as

$$\begin{aligned} &P_{\mathrm{ebt}}(t)\eta_{\mathrm{bb}} + P_{\mathrm{fc}}(t)\eta_{\mathrm{bo}} - P_{\mathrm{loss,em}}(t) - P_{\mathrm{aux}}(t) \geqslant P_{\mathrm{wh},\gamma}(t), \\ &\frac{P_{\mathrm{ebt}}(t)}{\eta_{\mathrm{bb}}} + P_{\mathrm{fc}}(t)\eta_{\mathrm{bo}} - P_{\mathrm{loss,em}}(t) - P_{\mathrm{aux}}(t) \geqslant P_{\mathrm{wh},\gamma}(t). \end{aligned} \tag{6.38}$$

As can be seen that Sub-problem II is convex and can be effectively solved by convex programming.

6.4 Case Study and Simulation Results

All simulations are conducted with CVX toolbox using solver MOSEK in MATLAB R2020b on a PC with the configuration of Intel Core i7-7700K CPU 4.2 GHz and 64 GB RAM.

6.4.1 Electric Machine Sizing and Modification of Velocity Trajectory

Electric Machine Sizing

The CDF of the estimated power demand for four trucking applications is shown in Fig. 6.5 and the main parameters are adopted from [74]. The maximum power

of the electric machine is designed to satisfy a CDF of the upper bound of the wheel power demand. The upper bound of the wheel power demand monotonically decreases with the decrease of CDF. This means that a lower CDF value gives a lower upper bound of the wheel power demand, leading to a lower power rating of the electric machine and a lower cost accordingly. However, the power rating of the electric machine significantly influences the acceleration characteristic. The minimum upper bound of wheel power required for typical trucks with acceleration from 0 to 50 km/h within 25 s is computed to be 170 kW, 247 kW, 330 kW, and 360 kW for applications of urban delivery, regional delivery, construction, and long-haul, respectively. To satisfy this acceleration characteristic, the electric machine should have the corresponded rated power, which covers 92.8 %, 94.3 %, 95.3 %, and 96.5 % of each driving cycle power demand. In the case study, electric machines are selected to meet the above acceleration characteristics and also to be able to cover at least 94 % of the wheel power demand in each driving cycle application. Therefore, the rated power of the electric machine is set as 218 kW, 247 kW, 330 kW, and 360 kW for applications of urban delivery, regional delivery, construction, and long-haul, respectively. The scaling factors are computed to be 1.09, 1.235, 1.65, and 1.8, accordingly.

Modification of Velocity Trajectory

With the determined maximum power of the electric machine, the delivered power is thereby limited during the truck movement. This could cause the velocity trajectory of the truck to deviate from the velocity of the original driving cycle. The velocity trajectory and the travel time for trucks in applications of urban delivery, regional delivery, construction, and long-haul can be obtained by solving problem (6.33). The optimal results at the selected γ for each driving cycle are compared with the original driving cycle for $\gamma = 1$ in Fig. 6.6-Fig. 6.9. In the application of urban delivery, the velocity trajectory at $\gamma = 94\%$ almost exactly follows the original velocity of the driving cycle, see Fig. 6.6(a). The same trends can also be found in applications of regional delivery, construction, and long-haul. This is due to the penalty of the summation of the kinetic energy in the objective function. From the enlarged view of the velocity trajectory as shown in sub-figure (b) in Fig. 6.6-Fig. 6.9, the velocity derivatives are reduced at the selected γ. This is owing to the maximum allowable peak power of electric machine for each journey, which is limited by the cumulative distribution function of the wheel power demand with the probability of the saturated power illustrated in sub-figure (c). It can also be seen that the velocity at the selected γ on some distance instances is higher

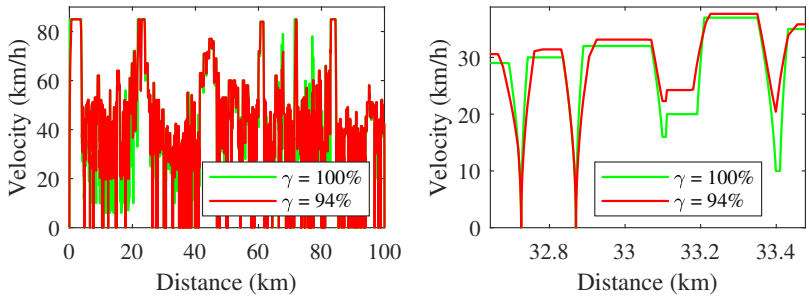

(a) Velocity trajectory.

(b) Enlarged view of velocity.

Fig. 6.6: Optimal results in the application of urban delivery.

than that at $\gamma = 100\%$. This is due to the time penalty in the objective function that ensures that the truck finishes the journey without much delay, even though the delivered peak wheel power is limited. Fig. 6.6-Fig. 6.9(d) show that travel times along each journey at the selected γ and $\gamma = 100\%$ have a good coherence. The trucks can finish all journeys at about the same time compared to $\gamma = 100\%$ as shown in Table 6.1.

Table 6.1: Time Elapsed at the End of Each Driving Cycle with Different γ.

Driving cycles	Elapsed time (s)	
Urban delivery	13127 at $\gamma = 100\%$	13156.2 at $\gamma = 94\%$
Regional delivery	5806.9 at $\gamma = 100\%$	5821.3 at $\gamma = 94.3\%$
Construction	8178.1 at $\gamma = 100\%$	8168.3 at $\gamma = 95.3\%$
Long-haul	4466.9 at $\gamma = 100\%$	4518.2 at $\gamma = 96.5\%$

6.4.2 Fuel Cell and Energy Buffer Sizing

In this section, the determined electric machine and the modified velocity trajectories from Sub-problem I are used to solve Sub-problem II. The optimal sizing of FC and energy buffer for several trucking applications are obtained. Three different energy buffer technologies are also compared for each driving cycle. The optimal sizing of power sources and their optimal power split can be simultaneously obtained by solving Sub-problem II. The optimal values of the FC system and the energy buffer for four driving cycles are shown in Table 6.2. Since the total truck

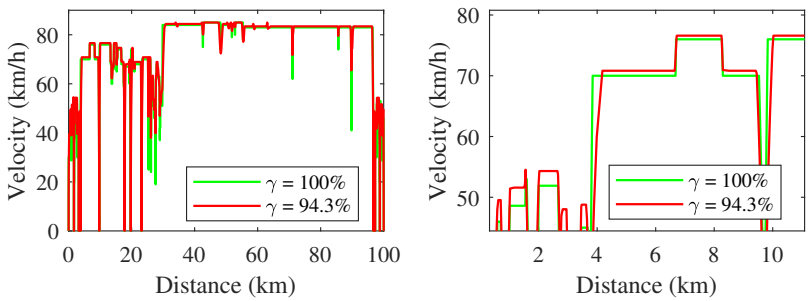

(a) Velocity trajectory. (b) Enlarged view of velocity.

Fig. 6.7: Optimal results in the application of regional delivery.

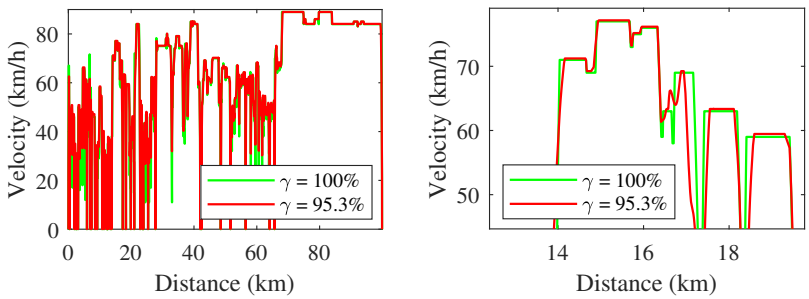

(a) Velocity trajectory. (b) Enlarged view of velocity.

Fig. 6.8: Optimal results in the application of construction.

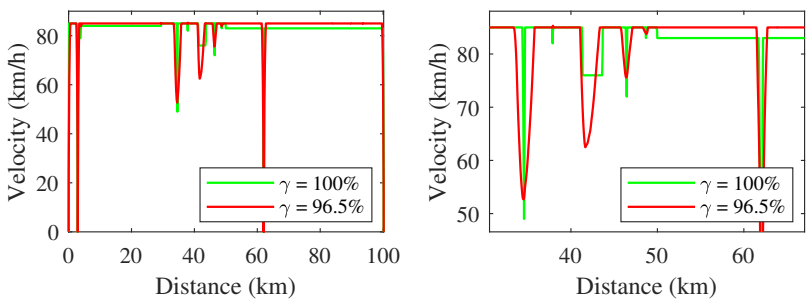

(a) Velocity trajectory. (b) Enlarged view of velocity.

Fig. 6.9: Optimal results in the application of long-haul.

mass is assumed to be constant, the payload significantly differs with the change of the scaling parameters of FC and energy buffer. Therefore, a heavier FC and energy buffer will result in a less payload. This is reflected in the difference in m_0, which is also listed in Table 6.2 for comparison.

Table 6.2: Optimal parameters of the fuel cell, different energy buffers, chassis mass, and total cost.

Driving cycles	Buffers	$P_{\text{fcs,max}}$	$P_{\text{s,max}}$	$E_{\text{s,max}}$	m_0	C_{total}
		kW	kW	kWh	kg	€/100km
Urban delivery	SC	111	652	3.43	16812	25.07
	LiC	76	223	9.93	17246	25.35
	LiB	73	478	59.51	16870	24.56
Regional delivery	SC	210	665	3.48	25375	29.30
	LiC	176	221	9.78	25822	29.37
	LiB	165	376	46.82	25642	27.52
Construction	SC	190	1496	7.82	30576	35.85
	LiC	158	336	14.92	31652	35.06
	LiB	147	512	64.71	31437	32.47
Long-haul	SC	340	791	4.14	37685	37.64
	LiC	266	226	10.15	38421	37.10
	LiB	248	517	64.98	38047	34.92

The FC maximum power in the case with SC is much higher than that of LiC and LiB as the energy buffer in all driving cycles. This is because SC has the lowest energy density and it cannot provide high power for a long time duration, which makes the FC provide the major power demand in most time periods. By contrast, LiC and LiB have a certain amount of energy capacity and they can provide relatively higher power resulting in lower power ratings of FC. However, the energy capacity of LiB in all driving cycles is much higher than that of other energy buffers. For instance, the energy capacity of the LiB in urban delivery application is almost 6 times and 17 times than that of the LiC and the SC, respectively.

Among all driving cycle applications, the truck using LiB as the energy buffer shows the cheapest cost, which is around 2%, 6%, 9%, and 7% lower than that

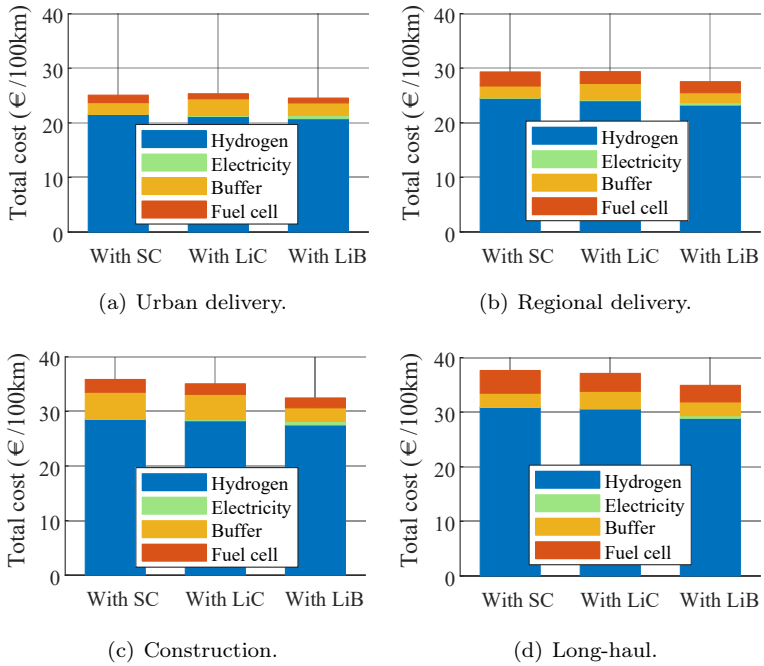

(a) Urban delivery.

(b) Regional delivery.

(c) Construction.

(d) Long-haul.

Fig. 6.10: Comparative total costs in the hybridization of different energy buffers among driving cycles.

of SC as the energy buffer in urban delivery, regional delivery, construction, and long-haul application, respectively. However, the cost in the case of SC and LiC as the energy buffer does not seem to have big difference. In the driving cycles of urban delivery and regional delivery, the cost of the truck with the SC as the energy buffer is slightly lower than that of LiC but it shows the opposite trend in construction and long-haul driving cycles. It is of interest to see that trucks with the LiC as the energy buffer can accommodate more payload than others even though they show higher cost than trucks with LiB as the energy buffer. The major reason of the difference in payloads is due to the different energy density of three energy buffer technologies. The energy density of the investigated LiB is 13.3 times and 3.3 times than that of the SC and the LiC. The difference of energy capacity also contributes to the difference in payloads. As a result, take the long-haul driving cycle as an example, the truck with LiC can carry 374 kg and 736 kg more payload than that of LiB and SC as the energy buffer.

To further understand the difference of the total cost caused by energy buffers,

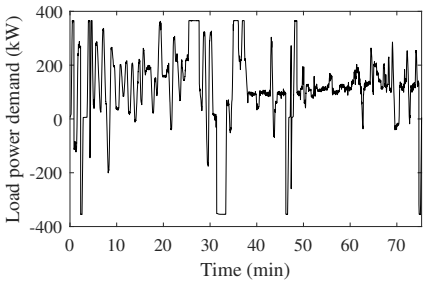

(a) Load power demand.

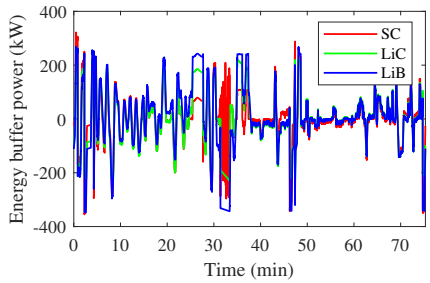

(b) Energy buffer power.

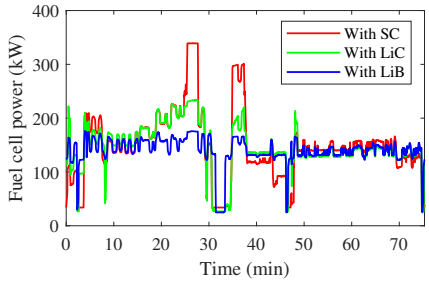

(c) Fuel cell power.

Fig. 6.11: Optimal power allocations in long-haul driving cycle.

the cost distribution is presented in Fig. 6.10. The hydrogen cost accounts for the highest percentage while the electricity cost is the lowest in each hybridization among all driving cycles. Also, the hydrogen cost in the hybridization with LiB shows the lowest expense compared to the hybridization with SC and LiC among all driving cycles due to a cheaper electricity unit price and high energy capacity of LiB. The FC cost in the case of LiB as the energy buffer is the lowest compared to other energy buffers among all driving cycles owing to the smallest FC power rating. The energy buffer cost differs for all driving cycles due to the big difference of the unit price and the energy capacity. For example, in construction driving cycle, the energy capacity of the LiB and the LiC is around 8.27 times and twice than that of the SC. However, the unit price of the SC is around 16 times and twice than those of the LiB and the SC, respectively. For these reasons, the LiC cost is almost the same as the SC cost, whereas the LiB cost is around half of the SC cost. Due to the extremely cheap unit price of the LiB, its cost is still the lowest among all energy buffers for all driving cycles even though much higher energy capacity of LiB is used.

6.4.3 Illustration of Power Allocation

Based on the optimal power rating of the FC and the energy capacity of the buffers, the optimal power allocations in long-haul driving cycle are illustrated as an example in Fig. 6.11. It is evident that the energy buffer mainly charges when the truck decelerates and discharges when the truck accelerates. Also, the power variation tendency of the energy buffer is severe and in general similar to the changes of the demanded load power. By contrast, the FC power is relatively stable due to the FC power variation rate being set within ±10% of the power rating per second in the case study.

It can also be seen that in propulsion mode, the FC and energy buffer together provide the load demanded power. In the hybridization with the SC, the FC is forced to provide more power compared those with the LiC and the LiB when the demanded power is continuously high. This is because the SC has limited energy and cannot provide high power constantly, which can be seen in 25-28 min. Moreover, the FC power maintains a minimum output power, which is set as 10% of its power rating in the case study. This enforces the energy buffer to be also charged by the FC power when working in regenerative braking mode. Among the investigated energy buffers, the LiB attempts to recuperate as much power as possible since it has relatively big energy capacity. The SC can only receive very small part of the negative power as shown in 30-34 min.

6.4.4 Summary

This chapter formulates a chance-constrained program to evaluate the performance of different energy storage technologies hybridized with FC for various trucking applications. The program is decomposed into two sub-problems and convex modeling steps are proposed to effectively solve them. Results show that the power rating of the electric machine is drastically reduced when the delivered power is satisfied in a probabilistic sense. Moreover, the cost effectiveness of the configuration with LiB is the best while the truck with LiC can carry more payload.

Chapter 7

Robust Co-design Optimization with Consideration of Uncertainties

This chapter is based on Paper I. The objective of this chapter is to formulate a robust co-design optimization framework for a FCHET in long-haul application considering the uncertainties in the driving conditions.

7.1 Model Development

The FCHET powertrain structure studied in this chapter is shown in Fig. 7.1. All component models are same as the ones in Chapter 6, but more simplified versions are considered in this chapter. Some other differences are addressed below.

7.1.1 Power Balance

The FC and the LiB are designed to provide all demanded electric power, while the LiB is assumed to capture all regenerative braking energy from the electric machine. The power balance can be rewritten as

$$\frac{R_{\mathrm{eb}}C_{\mathrm{eb}}}{2E_{\mathrm{eb}}(t)+u_{0\mathrm{eb}}^2C_{\mathrm{eb}}s_{\mathrm{eb}}n_{\mathrm{eb}}}P_{\mathrm{eb}}^2(t)-P_{\mathrm{eb}}(t)+P_{\mathrm{em}}(t)+P_{\mathrm{aux}}(t)-P_{\mathrm{fc}}(t)\eta_{\mathrm{dc}}=0, \quad (7.1)$$

where the inverter and the electric machine are considered as a whole. The electric power at the DC-side is denoted as $P_{\mathrm{em}}(t)$.

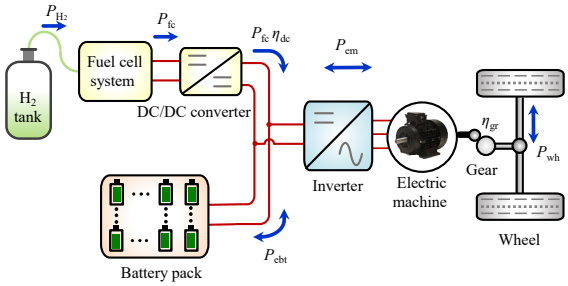

Fig. 7.1: FCHET powertrain structure.

7.1.2 Electric Drive System

For simplicity, the sizing of the electric machine is same as that in the long-haul application shown in Chapter 6, which is set as 360 kW with a scaling factor of 1.8. The electrical power in a scaled electric machine can be written as

$$P_{\mathrm{em}}(t) = s_{\mathrm{em}} f_{\mathrm{em}}(\omega(t), T_{\mathrm{em}}(t)/s_{\mathrm{em}}), \tag{7.2}$$

where $P_{\mathrm{em}}(t) = s_{\mathrm{em}} P_{\mathrm{emb}}(t)$ and $T_{\mathrm{em}}(t) = s_{\mathrm{em}} T_{\mathrm{emb}}(t)$. The function $f_{\mathrm{em}}(\cdot)$ represents the electric power varying with the rotational speed and the electromagnetic torque in the baseline model.

7.1.3 Fuel Cell

Without losing any generality, the consumed hydrogen power in the scaled FC model is written as

$$P_{\mathrm{H_2}}(t) = s_{\mathrm{fc}} f_{\mathrm{H_2}}(P_{\mathrm{fc}}(t)/s_{\mathrm{fc}}), \tag{7.3}$$

where the function $f_{\mathrm{H_2}}(\cdot)$ represents the consumed hydrogen power varying with the electric power in the baseline model. The FC degradation is not considered in this chapter.

7.1.4 Energy Buffer

It is assumed that the LiB can only be charged from the FC, the following constraint is used to maintain energy balance

$$E_{\mathrm{eb}}(t_{\mathrm{f}}) \geqslant E_{\mathrm{eb}}(t_0), \quad \forall t \in [t_0, t_{\mathrm{f}}], \tag{7.4}$$

where t_0 and t_{f} represent the starting and ending time samples of a driving cycle. For simplicity, the cycle life constraint of the LiB is not considered here.

7.2 Problem Formulation

7.2.1 Objective Function

Similar to Chapter 6, the target of the objective function is to minimize a total cost of operation cost and all components cost. Due to the energy balance of the LiB, the operation cost only includes the hydrogen consumption. Also, the cost of the electric machine is not needed since it is a constant. The objective function is denoted as $\phi_1(\mu_{\mathrm{D}}, \boldsymbol{\mu}_{\mathbf{X}}(k), \mathbf{u}(k), \boldsymbol{\mu}_{\mathbf{P}}(k))$ in the discrete form.

7.2.2 Deterministic Problem

As can be seen in (7.1), the summation of the FC power and LiB power is supposed to meet the power requirement of the electric machine, either $P_{\mathrm{fc}}(t)$ or $P_{\mathrm{eb}}(t)$ can be used as the control variable, which will not affect the optimal solutions since one can be computed by another.

By solving the quadratic polynomial equation (7.1), the internal power of the LiB pack at each time sample can be derived as

$$P_{\mathrm{eb}}(t) = \frac{u_{\mathrm{be}}(t) - \sqrt{u_{\mathrm{be}}(t)^2 - 4R_{\mathrm{eb}}u_{\mathrm{be}}(t)\left(P_{\mathrm{em}}(t) + P_{\mathrm{aux}}(t) - P_{\mathrm{fc}}(t)\eta_{\mathrm{dc}}\right)}}{2R_{\mathrm{eb}}}, \quad (7.5)$$

where $u_{\mathrm{be}}(t) = 2E_{\mathrm{eb}}(t)/C_{\mathrm{eb}} + u_{0\mathrm{eb}}^2 s_{\mathrm{eb}} n_{\mathrm{eb}}$. Apparently, the power $P_{\mathrm{eb}}(t)$ is a function of variables $E_{\mathrm{eb}}(t)$, s_{eb}, $P_{\mathrm{fc}}(t)$, and $P_{\mathrm{em}}(t)$.

Let s_{fc} and s_{eb} be the design decision variables, $P_{\mathrm{fc}}(t)$ or $P_{\mathrm{eb}}(t)$ be time dependent control variable, and $E_{\mathrm{eb}}(t)$ be the time dependent state variable. Therefore, one can get $\mathbf{d} = [s_{\mathrm{fc}}, s_{\mathrm{eb}}]$, $\mathbf{u}(t) = [P_{\mathrm{fc}}(t)]$ or $\mathbf{u}(t) = [P_{\mathrm{eb}}(t)]$, and $\mathbf{x}(t) = [E_{\mathrm{eb}}(t)]$. Due to numerous fixed parameters in $\mathbf{p}$, the elements of the parameter vector are not explicitly listed here but are assumed to appear in the objective function and the constraints. By summarizing all constraints, inequality constraint (6.32c) comprises (6.4),(6.5), (6.6), (6.7), (6.9), (6.14), (6.17), and (7.4). System dynamics (6.31d) include (6.15) only.

7.2.3 Robust Problem

For illustration of uncertainties propagation in robust problem, $P_{\mathrm{fc}}(t)$ is used as the control variable. The control variable still remains deterministic [83] since a backward simulation method is used, which is considered to be an open loop control system without feedback. The robust problem can be formulated based on the deterministic problem described in Section 7.2.2. There is no equality

constraint $\mathbf{g}$, which can be removed from the compact form (6.32). Following the work in [43, 84], the discrete form of the robust co-design optimization is formulated as

$$\min_{\boldsymbol{\mu}_\mathbf{D}, \boldsymbol{\mu}_\mathbf{X}(k), \mathbf{u}(k)} \mu_{\phi 1}(\mu_\mathrm{D}, \boldsymbol{\mu}_\mathbf{X}(k), \mathbf{u}(k), \boldsymbol{\mu}_\mathbf{P}(k)), \tag{7.6a}$$

$$\text{s.t. } \mathbf{h}(\boldsymbol{\mu}_\mathbf{D}, \boldsymbol{\mu}_\mathbf{X}(k), \mathbf{u}(k), \boldsymbol{\mu}_\mathbf{P}(k))) + m\boldsymbol{\sigma}_\mathbf{h} \leqslant 0, \tag{7.6b}$$

$$\boldsymbol{\mu}_\mathbf{X}(k+1) - \tilde{\mathbf{f}}(\boldsymbol{\mu}_\mathbf{D}, \boldsymbol{\mu}_\mathbf{X}(k), \mathbf{u}(k), \boldsymbol{\mu}_\mathbf{P}(k))) = 0, \tag{7.6c}$$

$$\mathrm{Var}[\boldsymbol{\mu}_\mathbf{X}(k+1)] - \mathrm{Var}[\tilde{\mathbf{f}}(\boldsymbol{\mu}_\mathbf{D}, \boldsymbol{\mu}_\mathbf{X}(k), \mathbf{U}(k), \boldsymbol{\mu}_\mathbf{P}(k)))] = 0, \tag{7.6d}$$

where $\mu_{\phi 1}$ is the expected value of the function ϕ_1, $\boldsymbol{\mu}_\mathbf{D}$, $\boldsymbol{\mu}_\mathbf{X}$, and $\boldsymbol{\mu}_\mathbf{P}$ are vectors of discretized expected values of decision variables, state variables, and parameters, respectively. Different from the work in [43, 84], more states might be required to compute the uncertainties in state variables. Since the LiB energy is the only state variable in this work, the variance of the LiB energy appears as another state variable. The dynamics are described as shown in (7.6d) and further details are given in Section 7.3. The notation m is the shift index of the inequality constraints and $\boldsymbol{\sigma}_\mathbf{h}$ is the vector of standard deviation of all inequality constraints. The shift index m is selected by designer, representing m times of standard deviation satisfaction of the inequality constraints $\mathbf{h}$ with respect to expected values. This ensures that the robust optimal design is at least $m\boldsymbol{\sigma}_\mathbf{h}$ away from the infeasible region of each inequality constraint. A common value of 3 is selected for shift index m in robust optimization, which shows that the satisfaction of inequality constraints is 99.7% when Gaussian distributions are assumed.

7.3 Uncertainty Analysis

Due to roadway shapes, traffic signs, driver behaviors, and weather condition, the vehicle operation speed at each location is differed even running on a same road. The vehicle speed and road slope at each time sample are uncertain, which can be assumed as Gaussian distributions. These uncertainties result in uncertainties in wheel power demand and also in electric power demand, which can also be propagated to uncertainties in state variables. The discrete system dynamics (7.6c) in robust co-design optimization problem can be rewritten as

$$\boldsymbol{\mu}_\mathbf{X}(k+1) = \tilde{\mathbf{f}}(\boldsymbol{\mu}_\mathbf{D}, \boldsymbol{\mu}_\mathbf{X}(k), \mathbf{u}(k), \boldsymbol{\mu}_\mathbf{P}(k))). \tag{7.7}$$

By applying the first moment to (7.7), the expected value of state variables at time instance $k+1$ can be obtained as

$$\mathbb{E}[\boldsymbol{\mu}_\mathbf{X}(k+1)] = \tilde{\mathbf{f}}(\boldsymbol{\mu}_\mathbf{D}, \boldsymbol{\mu}_\mathbf{X}(k), \mathbf{u}(k), \boldsymbol{\mu}_\mathbf{P}(k))). \tag{7.8}$$

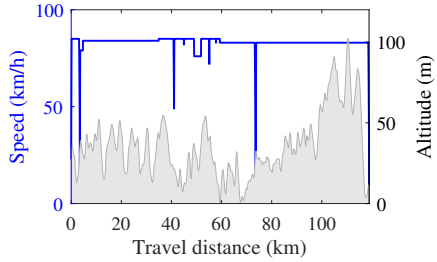

Fig. 7.2: Speed references and road altitude varying along traveled distance.

By applying the second central moment to (7.7) and ignoring covariance terms, one can get the variance of state variables

$$\mathrm{Var}[\boldsymbol{\mu}_{\mathbf{X}}(k+1)] = \mathrm{Var}[\tilde{\mathbf{f}}(\boldsymbol{\mu}_{\mathbf{D}}, \boldsymbol{\mu}_{\mathbf{X}}(k), \mathbf{u}(k), \boldsymbol{\mu}_{\mathbf{P}}(k)))]. \tag{7.9}$$

The proposed method may work with any smooth nonlinear function, or even with multiple states.

7.4 Case Study and Simulation Results

The co-design problem is implemented in MATLAB by using an open source software tool CasADi on a PC described in Chapter 6. The standard deviation values for the random scaling factors are given as 0.05.

7.4.1 Vehicle Movement Uncertainties

To analyze uncertainties of the vehicle movement, numerical speed trajectories are generated by using the Truck Benchmark Model published in [85]. More detailed information can be found in [86, 87]. A 118 km highway road from Södertälje to Norrköping in Sweden is adopted with the speed reference and the road slope shown in Fig. 7.2. To obtain different power capability of the truck, a scaling factor varying from 0.75 to 1.5 is used to scale the engine torque and power. To mimic the traffic condition, 10 multiplication coefficients within 0.9 and 1 are randomly generated, which is used to scale the speed reference shown in Fig. 7.2. Since the truck movement is also affected by the payload and the driver behavior, a PI controller with multiple groups of parameters is used and the truck gross weight is initialized by a value changing between 24 tons and 40 tons. By looping over several times of the simulation, 2040 speed trajectories associated with road slopes are obtained. The variations at time instance k are considered to follow

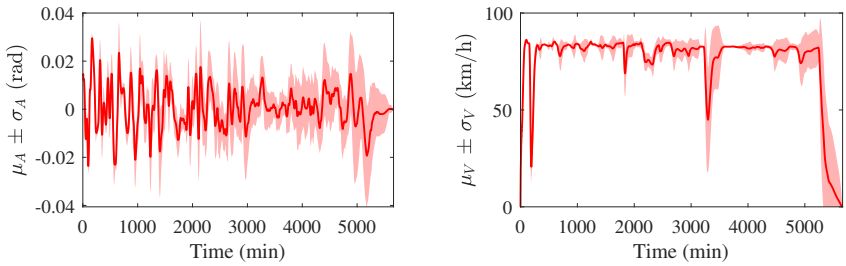

(a) Slope trajectory with its standard deviations.

(b) Speed trajectory with its standard deviations.

Fig. 7.3: Mean slope and mean speed with ±std. variations.

distributions, with expected values denoted as $\mu_V(k)$ and $\mu_A(k)$ for vehicle speed and road slope, respectively, and standard deviations denoted as $\sigma_V(k)$ and $\sigma_A(k)$. They are graphically shown in Fig. 7.3.

7.4.2 Power Sources Sizing

When a constant efficiency of the electric drive system with 90% is assumed, the maximum electric power at the DC-side, P_{em}, is computed as 400 kW. This saturates the mean trajectory with its 3 times of the standard deviation of the electric power demand, which gives the power reference for the sizing of the FC and the LiB as well as the energy management. For comparison, the same mean power trajectory of the electric power is used for the deterministic co-design optimization and the robust co-design optimization. The saturated standard deviation of the electric power is used in robust co-design optimization. The optimal designs of FC and LiB in deterministic co-design optimization and robust co-design optimization are compared in Tab. 7.1. As can be seen that the fuel cell maximum power does not show big difference while the maximum power and energy capacity of the LiB pack are forced to be bigger in the robust co-design optimization. Since the fuel cell power is selected as the control variable, which remains deterministic in the robust co-design optimization and the power capacity of the fuel cell does not show big difference. Due to uncertainties in the vehicle movement, the LiB energy is significantly affected, which results in a larger energy capacity of the LiB pack. It is noticed that the optimal results in robust co-design problem may differ slightly if the LiB power is selected as the control variable. The different results affected by the selection of the control variables is out scope of the study.

Table 7.1: Optimal designs of power sources.

Parameter (unit)	Deterministic	Robust
$P_{\mathrm{fc,max}}$ (kW)	233.65	233.59
$P_{\mathrm{eb,max}}$ (kW)	179.91	420.85
$E_{\mathrm{eb,max}}$ (kWh)	11.65	27.24

7.4.3 Energy Management

The optimal power distributions in deterministic co-design optimization and robust co-design optimization are shown in Fig. 7.4. The fuel cell peak power does not show any big difference, although its power variation is reduced in robust co-design optimization. Since the electric power follows a distribution at each time instance, the LiB power is also robustly constraint, leading to a larger power capacity in robust co-design optimization. Meanwhile, as shown in Fig. 7.5, the uncertainties of electric power results in a certain uncertainties in the LiB energy, which forces a larger LiB energy capacity. The total costs, including FC, LiB, and hydrogen, between deterministic co-design optimization and robust co-design are compared in Tab. 7.2. The hydrogen cost accounts for the highest percentage while the LiB cost is the lowest expense in both deterministic and robust co-design optimization. The hydrogen cost and fuel cell cost are almost the same in robust co-design optimization compared with the ones in deterministic co-design optimization. However, the LiB cost is doubled in robust co-design optimization due to the larger LiB capacity considering the uncertainties in truck movement.

Table 7.2: Total costs.

Costs (unit)	Deterministic	Robust
Fuel cell (€/100 km)	2.86	2.86
Battery (€/100 km)	0.45	1.06
Hydrogen (€/100 km)	25.80	25.73
Total (€/100 km)	29.11	29.65

7.4.4 Summary

This chapter formulates a robust co-design optimization framework for a FCHET. The truck movement is expressed as uncertain parameters in vehicle speed and the road slope. The propagation of uncertainties to state variables is illustrated

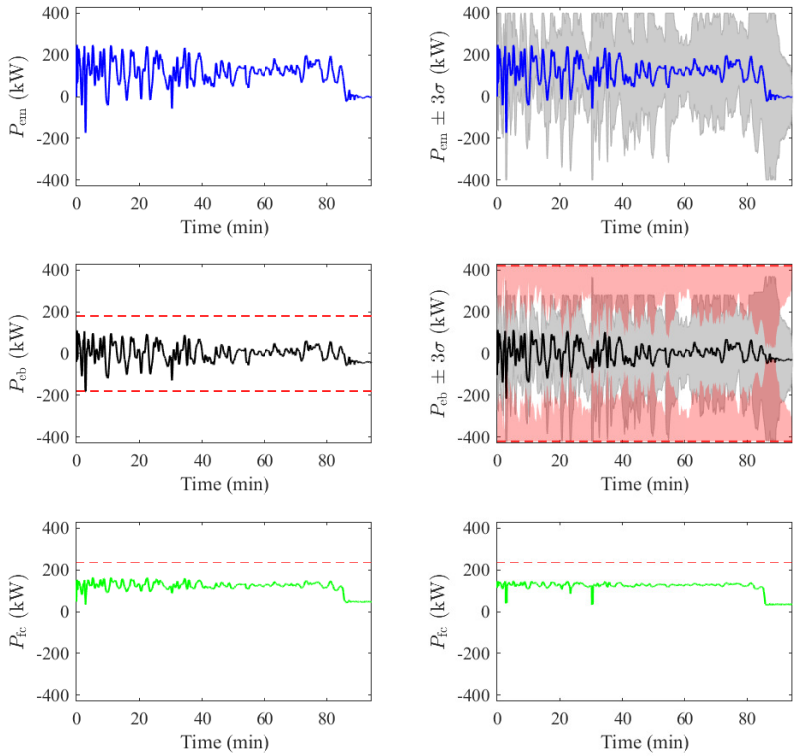

(a) Deterministic co-design optimization. (b) Robust co-design optimization.

Fig. 7.4: Optimal power distributions.

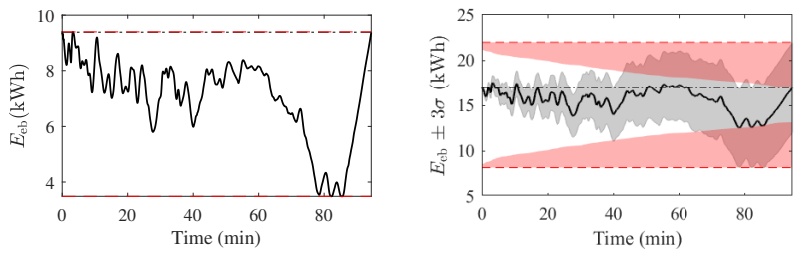

(a) Deterministic co-design optimization. (b) Robust co-design optimization.

Fig. 7.5: Battery energy trajectories.

by considering the uncertainties in the design decision variables. The case study indicates the importance of the robust approach in the joint component sizing and energy management framework. The uncertainties of the truck movement result in uncertainties of the battery energy and power requirements and finally to a bigger battery capacity. The energy capacity is around 2.4 times higher than that without considering the uncertainties.

Chapter 8

Conclusions and Future Work

This chapter summarizes the work presented in this thesis and outlines the future work.

8.1 Conclusions

This thesis performs a comprehensive study on FCHEVs, including the modeling, control, and optimization of various hybrid powertrain configurations. Main conclusions are summarized as follows.

- The FCHEV powertrain configuration needs to be determined based on its specific applications. While the passive hybrid topology is the simplest structure, it loses the active controllability. The semi-active hybrid topology has a certain degree of controllability and requires a proper control strategy. The fully-active hybrid topology shows the best controllability with a trade-off of a more complex structure.
- For the passive FC/SC topology, its inherent characteristics make the powertrain DC-link voltage passively determined by the load conditions. To examine the effects of the DC-link voltage variation, the energy efficiency and hydrogen consumption of a FC/SC powertrain for a passenger car are evaluated using 10 driving cycles. Results show that the energy efficiency is 53%–71% during propulsion and 84%–94% during braking, respectively. Moreover, the energy efficiency is higher during low-speed driving cycles, which results in a lower hydrogen consumption.

- A 3 kW lab-scale passive FC/SC configuration for a light vehicle is validated with each component experimentally modelled. Experiments show that the internal resistance of the FC stack is around 10 times larger than that of the SC bank and the SC bank performs as a LPF for the hybrid system. Therefore, when a step load is applied, the SC bank provides most of the transient current and power while the FC stack handles the steady current and power. Under the ArtUrban driving cycle current, the LPF effect of the SC makes it possible to downsize the FC stack, which only needs a peak power of one fifth of the load peak power. The SC evens out the current and power from the FC to prevent the FC from experiencing large currents and power variations.
- For the fully-active FC/SC system in bus applications, an adaptive power split method is used to smooth the FC current and prevent the SC from exceeding its lower and upper charge limits. The cut-off frequency of the LPF is adaptively controlled by the spectrum area ratio, which is determined by the SC SoC level and the load condition. Experimental results show that the SC SoC is effectively controlled within the desired range by adaptively controlling the current distribution between the FC and the SC. The load disturbance compensator improves the control performance in that the DC-link voltage fluctuation caused by the load current variation is significantly reduced. The proposed method can be easily tailored to other types of hybrid systems.
- A chance-constraint joint component sizing and energy management optimization framework is developed to evaluate the performance of various energy buffers for several trucking applications. The power rating of the electric machine is only around 18% of the wheel peak power demand when the delivered power meets the wheel power demand in a probabilistic sense. Moreover, the vehicle can finish the journey at a similar speed and in about the same time compared to those from the original driving cycle. When LiB is used as the energy buffer, the total cost of the vehicle is the lowest. If LiC is used as the energy buffer, the truck carries the heaviest payload.
- A robust co-design optimization framework is formulated for FCHETs with consideration of the uncertainties in its movements and design decision variables. Due to such uncertainties, the robust optimal solutions differ significantly from the deterministic optimal solutions. These uncertainties can also propagate to state variables and other optimal variables. For example, the battery energy and power become uncertain, which forces a

larger battery capacity and therefore a higher total cost in robust optimal solutions.

8.2 Future Work

Based on the work presented in this thesis, the following research can be conducted in the future.

- Hybridization of FCs with other energy storage devices for various vehicle applications.
  As two mainstream energy sources for EVs, FCs and batteries can complement each other as propulsion sources. However, vehicle design specifications such as driving range and pattern, lifetime, and power capability differ significantly. For example, batteries may be more suitable for urban applications (e.g., light-duty passenger cars) while FCs could be preferred for heavy-duty applications (e.g., forklifts, long-haul trucks, long-distance ferries, and more electric aircraft). To better utilize FCs and other energy storage technologies, a comprehensive investigation can be performed for various vehicle applications.
- Real-time energy management and power control for FCHEVs.
  While many aspects of FCHEVs have been extensively investigated, this technology is still under development. In fact, the FC lifetime has not met the U.S. DoE target and the hydrogen cost is still relatively high. One possibility is to develop a moving horizon real-time energy management and power control strategy to prolong the FC lifetime and minimize the hydrogen consumption.
- A mixed-integer nonlinear optimization framework for FCHEVs with simultaneous component sizing and energy management.
  Joint component sizing and energy management optimization for FCHEVs have been investigated. Usually, the optimization variables that determine the sizing of power sources and electric machines are treated as continuous quantities. However, these variables are discrete in nature. Therefore, mixed-integer nonlinear programming can be utilized to solve such problems. Also, accurate component models are required with the effects of degradation taken into account.
- Thermal effects of components on vehicle modeling, simulation, and optimization.
  The modeling, simulation, and optimization work conducted in this thesis

has not taken into account the thermal effects of the components, which need to be considered for more accurate component models. Moreover, the sensitivity of the FCHEV energy efficiency and hydrogen consumption needs to be swept at different temperatures.

- Modeling and simulation of a FC power plant considering off-board hydrogen utilization.
  Hydrogen can be used as a long-term energy storage solution for renewable energy sources. In a FC power plant, the heat generated during the hydrogen-to-electricity process is a critical asset. Therefore, the FC power plant needs to be properly modeled and analyzed to maximize the overall energy efficiency of the off-board hydrogen.

References

[1] H. Ritchie and M. Roser, "CO2 and greenhouse gas emissions," *Our World in Data*, 2020, https://ourworldindata.org/co2-and-other-greenhouse-gas-emissions.

[2] B. K. Ahn and T. W. Lim, "Fuel cell vehicle development at hyundai-kia motors," in *2006 International Forum on Strategic Technology*, 2006, pp. 199–201.

[3] Climate change: EU to cut CO2 emissions by 55% by 2030, url = https://www.bbc.com/news/world-europe-56828383.

[4] Q. Xun, Y. Liu, and E. Holmberg, "A comparative study of fuel cell electric vehicles hybridization with battery or supercapacitor," in *2018 International Symposium on Power Electronics, Electrical Drives, Automation and Motion (SPEEDAM)*, 2018, pp. 389–394.

[5] A. Haxhiu, A. Abdelhakim, S. Kanerva, and J. Bogen, "Electric power integration schemes of the hybrid fuel cells and batteries-fed marine vessels – an overview," *IEEE Transactions on Transportation Electrification*, pp. 1–1, 2021.

[6] A. K. M. Mohiuddin, A. Rahman, M. F. Chemani, and M. B. Zakaria, "Investigation of PEM fuel cell for automotive use," *IIUM Engineering Journal*, vol. 16, no. 2, p. 69–78, Nov. 2015.

[7] S. Mekhilef, R. Saidur, and A. Safari, "Comparative study of different fuel cell technologies," *Renewable and Sustainable Energy Reviews*, vol. 16, no. 1, pp. 981–989, 2012.

[8] L. Fan, Z. Tu, and S. H. Chan, "Recent development of hydrogen and fuel cell technologies: A review," *Energy Reports*, vol. 7, pp. 8421–8446, 2021.

[9] W. Colella, M. Jacobson, and D. Golden, "Switching to a U.S. hydrogen fuel cell vehicle fleet: The resultant change in emissions, energy use, and greenhouse gases," *Journal of Power Sources*, vol. 150, pp. 150–181, 2005.

[10] F. Dawood, M. Anda, and G. Shafiullah, "Hydrogen production for energy: An overview," *International Journal of Hydrogen Energy*, vol. 45, no. 7, pp. 3847–3869, 2020.

[11] H. Takenaka, "Research on electric power system for Honda FCX fuel cell vehicle," *Honda R&D Technical Review*, vol. 15, no. 2, pp. 1–6, 2003.

[12] A. Ohkawa, "Electric power control system for a fuel cell vehicle employing electric double-layer capacitor," *SAE World Congress*, pp. SAE 2004–01–1006, 2004.

[13] Clarity fuel cell powertrain. [Online]. Available: https://global.honda/innovation/FuelCell/Clarity-Fuel-Cell-engineer-talk.html

[14] H. Yumiya, M. Kizaki, and H. Asai, "Toyota fuel cell system (TFCS)," *World Electric Vehicle Journal*, vol. 7, pp. 1–8, 2015.

[15] Y. Nonobe, "Development of the fuel cell vehicle Mirai," *IEEJ Transactions on Electrical and Electronic Engineering*, vol. 12, pp. 5–9, 2017.

[16] NEXO emergency response guide. [Online]. Available: https://h2tools.org/sites/default/files/NEXO%20Emergency%20Response%20Guide.pdf

[17] "Toyota unveils project portal 2.0 heavy truck," *Fuel Cells Bulletin*, vol. 2018, no. 7, p. 1, 2018.

[18] "Hyundai upgrades XCIENT fuel cell truck," *Fuel Cells Bulletin*, vol. 2021, no. 6, p. 4, 2021.

[19] Record number of newly opened hydrogen refuelling stations in 2020, url = https://www.h2stations.org.

[20] Q. Xun and Y. Liu, "Evaluation of fluctuating voltage topology with fuel cells and supercapacitors for automotive applications," *International Journal of Energy Research*, vol. 43, pp. 1–13, 2019.

[21] H. S. Das, C. W. Tan, and A. Yatim, "Fuel cell hybrid electric vehicles: A review on power conditioning units and topologies," *Renewable and Sustainable Energy Reviews*, vol. 76, pp. 268–291, 2017.

[22] A. Emadi, K. Rajashekara, S. Williamson, and S. Lukic, "Topological overview of hybrid electric and fuel cell vehicular power system architectures and configurations," *IEEE Transactions on Vehicular Technology*, vol. 54, no. 3, pp. 763–770, 2005.

[23] D. Arora, M. Hinaje, C. Bonnet, and et al, "Sizing supercapacitor for direct hybridization with polymer electrolyte membrane fuel cell," in *IEEE Vehicle Power and Propulsion Conference (VPPC)*, August 2018, pp. 1–7.

[24] B. Morin, D. V. Laethem, C. Turpin, and et al, "Direct hybridization fuel cell-supercapacitor," *Fuel Cells*, vol. 14, no. 3, pp. 500–507, 2014.

[25] K. Gerardin, S. Rael, C. Bonnet, D. Arora, and F. Lapicque, "Direct coupling of PEM fuel cell to supercapacitors for higher durability and better energy management," *Fuel Cells*, vol. 18, no. 3, pp. 315–325, 2018.

[26] C. Dépature, A. Macías, A. Jácome, and et al, "Fuel cell/supercapacitor passive configuration sizing approach for vehicular applications," *International Journal of Hydrogen Energy*, vol. 45, pp. 1–12, 2020.

[27] B. Wu, M. A. Parkes, V. Yufit, and et al, "Design and testing of a 9.5 kWe proton exchange membrane fuel cell-supercapacitor passive hybrid system," *International Journal of Hydrogen Energy*, vol. 39, pp. 7885–7896, 2014.

[28] M. Ouyang, L. Xu, J. Li, L. Lu, D. Gao, and Q. Xie, "Performance comparison of two fuel cell hybrid buses with different powertrain and energy management strategies," *Journal of Power Sources*, vol. 163, pp. 467–479, 2006.

[29] T. Azib, O. Bethoux, G. Remy, C. Marchand, and E. Berthelot, "An innovative control strategy of a single converter for hybrid fuel cell/supercapacitor power source," *IEEE Transactions on Industrial Electronics*, vol. 57, no. 12, pp. 4024–4031, 2010.

[30] X. Wu, X. Hu, X. Yin, Y. Peng, and V. Pickert, "Convex programming improved online power management in a range extended fuel cell electric truck," *Journal of Power Sources*, vol. 476, p. 228642, 2020.

[31] D. Zhou, A. Al-Durra, I. Matraji, A. Ravey, and F. Gao, "Online energy management strategy of fuel cell hybrid electric vehicles: A fractional-order extremum seeking method," *IEEE Transactions on Industrial Electronics*, vol. 65, no. 8, pp. 6787–6799, 2018.

[32] Y. Yan, Q. Li, W. Chen, B. Su, J. Liu, and L. Ma, "Optimal energy management and control in multimode equivalent energy consumption of fuel

cell/supercapacitor of hybrid electric tram," *IEEE Transactions on Industrial Electronics*, vol. 66, no. 8, pp. 6065–6076, 2019.

[33] A. Ferrara, S. Jakubek, and C. Hametner, "Energy management of heavy-duty fuel cell vehicles in real-world driving scenarios: robust design of strategies to maximize the hydrogen economy and system lifetime," *Energy Conversion and Management*, vol. 232, p. 113795, 2021.

[34] D. Feroldi, M. Serra, and J. Riera, "Energy management strategies based on efficiency map for fuel cell hybrid vehicles," *Journal of Power Sources*, vol. 190, no. 2, pp. 387–401, 2009.

[35] X. Huang, J. M. A. Curti, and Y. Hori, "Energy management strategy with optimized power interface for the battery supercapacitor hybrid system of electric vehicles," in *Proceedings of IECON 2013-39th Annual Conference of the IEEE Industrial Electronics Society*, 2013, pp. 4635–4640.

[36] D. Pavković, M. Lobrović, M. Hrgetić, and A. Komljenović, "A design of cascade control system and adaptive load compensator for battery/ultracapacitor hybrid energy storage-based direct current microgrid," *Energy Conversion and Management*, vol. 114, pp. 154–167, 2016.

[37] Q. Xun, V. Roda, Y. Liu, X. Huang, and R. Costa-Castelló, "An adaptive power split strategy with a load disturbance compensator for fuel cell/supercapacitor powertrains," *Journal of Energy Storage*, vol. 44, p. 103341, 2021.

[38] S. Ziaeinejad, Y. Sangsefidi, and A. Mehrizi-Aani, "Fuel cell-based auxiliary power unit: EMS, sizing, and current estimator-based controller," *IEEE Transactions on Vehicular Technology*, vol. 65, no. 5, pp. 4286–4835, Nov. 2016.

[39] Y. Wu, Z. Huang, H. Liao, and et al, "Adaptive power allocation using artificial potential field with compensator for hybrid energy storage systems in electric vehicles," *Applied Energy*, vol. 257, pp. 1–14, 2020.

[40] N. Murgovski, X. Hu, L. Johannesson, and B. Egardt, *Combined design and control optimization of hybrid vehicles*. John Wiley & Sons, Ltd, 2015.

[41] X. Hu, N. Murgovski, L. M. Johannesson, and B. Egardt, "Optimal dimensioning and power managementof a fuel cell/battery hybrid bus via convex programming," *IEEE/ASME Transactions on Mechatronics*, vol. 20, no. 1, pp. 457–468, Feb. 2015.

[42] X. Hu, L. Johannesson, N. Murgovski, and B. Egardt, "Longevity-conscious dimensioning and power management of the hybrid energy storage system in a fuel cell hybrid electric bus," *Applied Energy*, vol. 137, pp. 913–924, 2015.

[43] S. Azad and M. J. Alexander-Ramos, "Robust combined design and control optimization of hybrid-electric vehicles using MDSDO," *IEEE Transactions on Vehicular Technology*, vol. 70, no. 5, pp. 4139–4152, 2021.

[44] S. B. Shah, B. Silwal, and A. Lehikoinen, "Efficiency of an electrical machine in electric vehicle application," *Journal of the Institue of Engineering*, vol. 11, no. 1, pp. 20–29, 2015.

[45] A. Wintrich, U. Nicolai, W. Tursky, and T. Reimann, "Application manual power semiconductors," Semikron Int. GmbH, Nurnberg, Germany, 2011.

[46] J. M. Miller, *Propulsion Systems for Hybrid Vehicles*, 2nd ed., ser. 10. United Kingdom: Institution of Engineering and Technology, 2010.

[47] M. Bartłomiejczyk and R. Kołacz, "The reduction of auxiliaries power demand: The challenge for electromobility in public transportation," *Journal of Cleaner Production*, vol. 252, p. 119776, 2020.

[48] T. J. Hendricks and M. O'Keefe, "Heavy vehicle auxiliary load electrification for the essential power system program: Benefits, tradeoffs, and remaining challenges," *SAE Transactions Journal of Commercial Vehicles*, vol. 111, no. 2, pp. 841–851, 2002.

[49] T. Agaesse, "Simulations of one and two-phase flows in porous microstructures, from tomographic images of gas diffusion layers of proton exchange membrane fuel cells," Ph.D. dissertation, National Polytechnic Institute of Toulouse, Toulouse, May 2017.

[50] R. Azega, A. D. Smith, A. Vyas, Q. Li, M. Haque, Z. Geng, Q. Xun, X. Zhang, S. Thurakkal, N. R. Chowdhury, S. Z. Hajibagher, T. Thiringer, Y. Liu, P. Lundgren, and P. Enoksson, "Supercapacitors and batteries, a tale of two technologies: past, present and beyond," *Journal of Energy Storage*, vol. submitted, 2021.

[51] Q. Xun, S. Lundberg, and Y. Liu, "Design and experimental verification of a fuel cell/supercapacitor passive configuration for a light vehicle," *Journal of Energy Storage*, vol. 33, p. 102110, 2021.

[52] D. Zhou, A. Al-Durra, F. Gao, A. Ravey, I. Matraji, and M. Godoy Simões, "Online energy management strategy of fuel cell hybrid electric vehicles based

on data fusion approach," *Journal of Power Sources*, vol. 366, pp. 278–291, 2017.

[53] D. Zhou, A. Ravey, A. Al-Durra, and F. Gao, "A comparative study of extremum seeking methods applied to online energy management strategy of fuel cell hybrid electric vehicles," *Energy Conversion and Management*, vol. 151, pp. 778–790, 2017.

[54] H. Zhao and A. F. Burke, "Fuel cell powered vehicle using supercapacitors-device characteristics, control strategies, and simulation results," *Fuel Cells*, vol. 10, no. 5, pp. 879–896, 2010.

[55] Q. Xun, Y. Liu, and N. Zhao, "Energy efficiency comparison of hybrid power-train systems for fuel-cell-based electric vehicles," in *2020 IEEE Transportation Electrification Conference Expo (ITEC)*, 2020, pp. 1234–1239.

[56] A. Macías, M. Kandidayeni, L.Boulon, and J. Trovão, "Passive and active coupling comparison of fuel cell and supercapacitor for a three-wheel electric vehicle," *Fuel Cells*, vol. 20, no. 3, pp. 351–361, 2020.

[57] C. Dépature, A. Macías, A. Jácome, L. Boulon, J. Solano, and J. P. Trovão, "Fuel cell/supercapacitor passive configuration sizing approach for vehicular applications," *International Journal of Hydrogen Energy*, vol. 45, no. 50, pp. 26 501–26 512, 2020, the recent studies towards hydrogen production and fuel cells.

[58] T. Fukushima, A. Iwai, N. Yamaguchi, and H. Shinoki, "Electric drive motor for fuel cell vehicle FCX Clarity," *Honda R&D Technical Review*, vol. 21, no. 1, pp. 63–70, 2009.

[59] Q. Xun, Y. Liu, J. Zhao, and E. A. Grunditz, "Modelling and simulation of fuel cell/supercapacitor passive hybrid vehicle system," in *Proceedings of the 11th Annual IEEE Energy Conversion Congress and Exposition (ECCE)*, 2018, pp. 389–394.

[60] (Accessed on 2014-03-20) IGBT modules up to 600 V, 650 V. Infineon. [Online]. Available: https://www.infineon.com/cms/en/product/power/igbt/igbt-modules/igbt-modules-up-to-600v-650v/

[61] S. N. Motapon, O. Tremblay, and L.-A. Dessaint, "Development of a generic fuel cell model: application to a fuel cell vehicle simulation," *International Journal of Power Electronics*, vol. 4, no. 6, pp. 505–522, 2012.

[62] S. N. Motapon, L. A. Dessaint, and K. Al-Haddad, "A comparative study of

energy management schemes for a fuel-cell hybrid emergency power system of more-electric aircraft," *IEEE Transactions on Industrial Electronics*, vol. 61, no. 3, pp. 1320–1334, 2014.

[63] F. Khan, A. Nawaz, M. A. Muhammad, and M. A. Khadim, "Review and analysis of MATLAB@ Simulink model of PEM fuel cell stack," *International Journal of Engineering & Computer Science*, vol. 13, pp. 31–34, 2013.

[64] A. Kirubakaran, S. Jain, and R. Nema, "The PEM fuel cell system with DC/DC boost converter: design, modeling and simulation," *International Journal on Electrical and Power Engineering*, vol. 1, no. 1, pp. 26–30, 2010.

[65] O. Leena and P. K. Jyoti, "Modelling and simulation of hydrogen fuel cells," *International Journal of Engineering Science Invention*, vol. 3, no. 6, pp. 1320–1334, 2014.

[66] F. Barbir, "PEM fuel cells: theory and practice," 2005.

[67] Q. Xun, Y. Liu, X. Huang, E. A. Grunditz, J. Zhao, and N. Zhao, "Drive cycle energy efficiency of fuel cell/supercapacitor passive hybrid vehicle system," *IEEE Transactions on Industry Applications*, vol. 57, no. 1, pp. 894–903, 2021.

[68] Technology assessment of a fuel cell vehicle: 2017 Toyota Mirai, Argonne National Laboratory Report. [Online]. Available: https://publications.anl.gov/anlpubs/2018/06/144774.pdf

[69] N. Zhao, N. Schofield, and W. Niu, "Energy storage system for a port crane hybrid power-train," *IEEE Transactions on Transportation Electrification*, vol. 2, no. 4, pp. 480–492, 2016.

[70] Maxwell Technologies Ultracapacitors: BCAP3000 datasheet. [Online]. Available: https://www.maxwell.com/images/documents/K2Series_DS_1015370_5_20141104.pdf

[71] E. A. Grunditz and T. Thiringer, "Characterizing BEV powertrain energy consumption, efficiency and range during official and drive cycles from Gothenburg/Sweden," *IEEE Transactions on Vehicular Technology*, vol. 65, no. 6, pp. 3964–3980, 2016.

[72] L. Sun, K. Feng, C. Chapman, and et al, "An adaptive power-split strategy for battery–supercapacitor powertrain–design, simulation, and experiment," *IEEE Transactions on Power Electronics*, vol. 32, no. 12, pp. 9364–9375, 2017.

[73] E. Sariyildiz and K. Ohnishi, "A guide to design disturbance observer," *Journal*

of Dynamic System, Measurements, and Control, vol. 136, no. 2, pp. 0 210 111–02 101 110, 2014.

[74] Q. Xun, N. Murgovski, and Y. Liu, "Joint component sizing and energy management for fuel cell hybrid electric trucks," *IEEE Transactions on Vehicular Technology*, 2022.

[75] X. Hu, N. Murgovski, L. Johannesson, and B. Egardt, "Energy efficiency analysis of a series plug-in hybrid electric bus with different energy management strategies and battery sizes," *Applied Energy*, vol. 111, pp. 1001–1009, 2013.

[76] N. Murgovski, L. Johannesson, J. Hellgren, B. Egardt, and J. Sjöberg, "Convex optimization of charging infrastructure design and component sizing of a plug-in series HEV powertrain," *IFAC Proceedings Volumes*, vol. 44, no. 1, pp. 13 052–13 057, 2011.

[77] C. Dépature, S. Jemeï, L. Boulon, A. Bouscayrol, N. Marx, S. Morando, and A. Castaings, "IEEE VTS motor vehicles challenge 2017 - energy management of a fuel cell/battery vehicle," in *2016 IEEE Vehicle Power and Propulsion Conference (VPPC)*, 2016, pp. 4635–4640.

[78] K. Davis and J. G. Hayes, "Fuel cell vehicle energy management strategy based on the cost of ownership," *IET Electrical Systems in Transportation*, vol. 9, no. 4, pp. 226–236, 2019.

[79] S. Wei, J. Jiang, N. Murgovski, J. Sjöberg, W. Zhang, C. Zhang, and X. Hu, "Optimisation of a catenary-free tramline equipped with stationary energy storage systems," *IEEE Transactions on Vehicular Technology*, vol. 69, no. 3, pp. 2449–2462, 2020.

[80] N. Takami, H. Inagaki, Y. Tatebayashi, H. Saruwatari, K. Honda, and S. Egusa, "High-power and long-life lithium-ion batteries using lithium titanium oxide anode for automotive and stationary power applications," *Journal of Power Sources*, vol. 244, pp. 469–475, 2013.

[81] S. Wei, N. Murgovski, J. Jiang, X. Hu, W. Zhang, and C. Zhang, "Stochastic optimization of a stationary energy storage system for a catenary-free tramline," *Applied Energy*, vol. 280, p. 115711, 2020.

[82] S. Boyd and L. Vandenberghe, *Convex Optimization*. Cambridge, UK: Cambridge University Press, 2004.

[83] X. Li, Z. Zhang, L. Gao, and C. Gao, "Aircraft robust trajectory optimization using nonintrusive polynomial chaos," *Journal of Aircraft*, vol. 51, no. 5, pp.

1592–1603, 2014.

[84] S. Azad and M. J. Alexander-Ramos, "Robust MDSDO for co-design of stochastic dynamic systems," *Journal of Mechanical Design*, vol. 142, no. 1, 2019, 011403.

[85] (Accessed: Nov. 2018) Truck benchmark model. [Online]. Available: https://www.vehicular.isy.liu.se/en/Software/TruckBenchmark_AAC2016/

[86] L. Eriksson, A. Larsson, and A. Thomasson, "The AAC2016 benchmark - look-ahead control of heavy duty trucks on open roads," *IFAC-PapersOnLine*, vol. 49, no. 11, pp. 121–127, 2016, 8th IFAC Symposium on Advances in Automotive Control AAC 2016.

[87] L. Eriksson, A. Thomasson, K. Ekberg, A. Reig, M. Eifert, F. Donatantonio, A. D'Amato, I. Arsie, C. Pianese, P. Otta, M. Held, U. Vögele, and C. Endisch, "Look-ahead controls of heavy duty trucks on open roads - six benchmark solutions," *Control Engineering Practice*, vol. 83, pp. 45–66, 2019.

Part II

Included papers